UNIVERSITY OF Southampton

University of Southampton Research Repository
ePrints Soton

Copyright © and Moral Rights for this thesis are retained by the author and/or other copyright owners. A copy can be downloaded for personal non-commercial research or study, without prior permission or charge. This thesis cannot be reproduced or quoted extensively from without first obtaining permission in writing from the copyright holder/s. The content must not be changed in any way or sold commercially in any format or medium without the formal permission of the copyright holders.

When referring to this work, full bibliographic details including the author, title, awarding institution and date of the thesis must be given e.g.

AUTHOR (year of submission) "Full thesis title", University of Southampton, name of the University School or Department, PhD Thesis, pagination

http://eprints.soton.ac.uk

UNIVERSITY OF SOUTHAMPTON

FACULTY OF ENGINEERING, SCIENCE & MATHEMATICS

School of Ocean & Earth Science

TRACE ELEMENT DISTRIBUTIONS IN RIDGE FLANK SEDIMENTS FROM THE EAST PACIFIC RISE, AND THEIR USE AS PROXIES OF PAST OCEAN CONDITIONS

by

Sarah Louise Taylor

Thesis for the degree of Doctor of Philosophy

November 2008

This thesis for the degree of Doctor of Philosophy has been produced under the supervision of the following persons:

Thesis supervisors:	Dr R. A. Mills
	Professor J. Thomson
	Dr D. A. Teagle
	Dr R. Taylor

Chair of Advisory Panel: Professor Martin Palmer

UNIVERSITY OF SOUTHAMPTON

ABSTRACT

FACULTY OF ENGINEERING, SCIENCE & MATHEMATICS
SCHOOL OF OCEAN AND EARTH SCIENCE

Doctor of Philosophy

TRACE ELEMENT DISTRIBUTIONS IN RIDGE FLANK SEDIMENTS FROM THE EAST PACIFIC RISE, AND THEIR USE AS PROXIES OF PAST OCEAN CONDITIONS

By Sarah Louise Taylor

Abstract

The eastern equatorial and tropical Pacific regions are areas of significant carbon fluxes from the atmosphere to the ocean interior. Changes in the function of marine biogeochemical cycles in this region potentially exert an important control on global climate. Understanding controls on and changes to ocean chemistry and circulation in this region is therefore of great importance.

Redox sensitive metal distributions in hydrothermal sediments have yet to be exploited effectively as proxies of past ocean conditions. This work presents a 740 ka sediment record from an archived core collected at 14°47'S overlying 1.1 Ma crust on the western flank of the EPR. The metalliferous sedimentation is overprinted by diagenetic mobilisation arising from variations in the sediment redox status of the sediments. Amorphous ferrihydrite phases delivered to the sediment have undergone significant alteration to more stable crystalline forms. Under glacial conditions, the transformation of ferrihydrite appears to be impeded, which is inferred to be a function of a distinct change in the redox status of the sediments under glacial conditions.

Oxyanions coprecipitated with Fe and Mn (hydr)oxides from the hydrothermal plume (P, V, U) are partitioned during Fe-oxide alteration. V is preferentially incorporated into goethite and residual phases, locking the plume derived V within the sediment. Sediment P/Fe ratios are lower than overlying plume values, and vary systematically with variations in ferrihydrite transformation to goethite on glacial-interglacial timescales. This transformation is inferred to lead to P loss from the particulate/sediment phase. Uranium is highly enriched in sulphide rich EPR plume particles and the sediments at 14°S. U/Fe ratios indicate there has been enhanced release of U under interglacial conditions, and preservation of plume U/Fe ratios under glacial conditions. Mo/Mn ratios are used to confirm the changes in redox status on glacial-interglacial timescales at this site. There is a general trend over Marine Isotope Stages 1-14 of a deepening of the sediment redox front through interglacial stages with a shallowing at the onset of glaciation. Enhanced sub-oxic conditions associated with glacial conditions (in particular MIS 12) are attributed to enhanced productivity (and carbon export to the seafloor) and decreased bottom water O_2 (and therefore reduced ventilation of the deep water). This is consistent with paleoproductivity data from other parts of the Eastern Pacific and adds new information of past conditions in a region which has not been studied.

Contents

Table of Figures

Table of Tables

List of Abbreviations

EEP	Eastern Equatorial Pacific
EPR	East Pacific Rise
EXCO	EXchange between Crust and Ocean
FF	Focussing Factor
HNLC	High Nutrient, Low Chlorophyll
ICP-AES	Inductively Coupled Atomic Emission Spectroscopy
ICP-MS	Inductively Couple Mass Spectrometry
JGOFS	Joint Global Ocean Flux Study
LGM	Last Glacial Maximum
MIS	Marine Isotope Stage
MOR	Mid Ocean Ridge
MORT	Mean Oceanic Residence Time
NADW	North Atlantic Deep Water
NPDW	North Pacific Deep Water
ODP	Ocean Drilling Program
SEC	Southern Equatorial Current
SEM	Scanning Electron Microscopy
TAG	Trans Atlantic Geotraverse
TWT	Two-way Transit
USGS	United States Geological Survey
WOCE	World Ocean Circulation Experiment
XRD	X-Ray Diffraction
XRF	X-ray Fluorescence

DECLARATION OF AUTHORSHIP

I, Sarah Taylor

declare that the thesis entitled

TRACE ELEMENT DISTRIBUTIONS IN RIDGE FLANK SEDIMENTS FROM THE EAST PACIFIC RISE, AND THEIR USE AS PROXIES OF PAST OCEAN CONDITIONS

and the work presented in the thesis are both my own, and have been generated by me as the result of my own original research. I confirm that:

- this work was done wholly or mainly while in candidature for a research degree at this University;
- where any part of this thesis has previously been submitted for a degree or any other qualification at this University or any other institution, this has been clearly stated;
- where I have consulted the published work of others, this is always clearly attributed;
- where I have quoted from the work of others, the source is always given. With the exception of such quotations, this thesis is entirely my own work;
- I have acknowledged all main sources of help;
- where the thesis is based on work done by myself jointly with others, I have made clear exactly what was done by others and what I have contributed myself;
- none of this work has been published before submission

Signed: ……..

Date:……

Acknowledgements

I would like to thank my primary supervisor Rachel Mills, for guidance, support and innumerable discussions throughout the construction of this thesis.

I would also like to thank the other members of my supervisory panel, John Thomson, Damon Teagle Rex Taylor, and Martin Palmer, for their guidance and support during the course of this research.

Analytical data was acquired with the assistance of numerous people at the NOC, whom I would like to thank for both their time and patience:

Darryl Green, for training me in digestion techniques, coulometry and giving me lab space, for all the ICP-AES data presented in this thesis and for many technical discussions and assistance.

Heiko Palike for invaluable help producing the age model that forms the basis for the bulk of this work

Ian Croudace for training in the preparation and running of samples for analysis by XRF, and for aid in resolving various XRF data issues

Phil Warwick and Pawel Gaca for assistance planning and carrying out the α-spectrometry, and helping fix the problems that subsequently arose

Andy Milton for all the ICP-MS data presented in this thesis

Ross Williams, for XRD analyses

Richard Pearce, for help with SEM analyses

Mike Bolshaw, for oxygen isotope analyses

The sequential leaches presented in this thesis were performed by Paula Sanchez, and data are reproduced by her kind permission.

I also wish to acknowledge use of the Ferret program for production of a number of graphics contained in this thesis. Ferret is a product of NOAA's Pacific Marine Environmental Laboratory. (Information is available at **http://ferret.pmel.noaa.gov/Ferret/**)

And finally David Berry for help with the use of ferret and everything else!

Chapter 1: Introduction

1.1 General Introduction

The Southeast and equatorial Pacific has been the focus of great interest for a number of years because of the regions importance in the global carbon cycle. The eastern equatorial Pacific (EEP), at the upwelling of the equatorial undercurrent, is the location of the biggest flux of CO_2 to the atmosphere from the modern oceans, and thus the role this region plays in determining climate is obviously important (Tans et al., 1990).

Productivity across the region is highest at the equator and decreases moving southwards through the tropical southeast Pacific. The area is bounded on the east by the Peru margin upwelling, and the highest productivity is observed in the east (e.g. Antoine et al., 1996; Behrenfield & Falkowski, 1997). This productivity has been found to be significant on a global scale (Chavez & Barber, 1987). However, biological productivity does not compensate completely for the elevated CO_2. There is inefficient use of the available nutrients and the EEP and subtropical southeast Pacific form a high nutrient low chlorophyll (HNLC) zone (Loubere et al., 2003).

The productivity is driven by the upwelling of the Equatorial Undercurrent, which draws on several different water sources; a combination of water subducted in the subtropical gyres (Huang & Liu, 1999) and water sourced from the subantarctic regions of the southwest Pacific (Tsuchiya et al., 1990, Togweiller et al., 1991). Water upwelled at the Peru margin flows back to the equator as part of the South Equatorial Current (SEC).

The main topographic high in the Southeast Pacific is the East Pacific Rise (EPR). The EPR between 13^{o}-19^{o}S is a super-fast spreading centre, moving at 143-150mm/yr (Cormier et al., 1996; DeMets et al., 1994; Grevemeyer et al., 2002), and is the locus of intense hydrothermal activity. A significant percentage (~40%) of known high temperature venting occurs on fast spreading ridges and venting from this ridge section has been found to be almost continuous (Baker et al., 1995; Feely et al., 1996; Fouquet, 1997). This venting has implications for the sedimentation in the area. The

Southeast Pacific contains the largest spatial area of recent metalliferous sediments in the oceans.

The main sources and gross composition of sediments in the southern East Pacific Rise has been studied in detail (Dymond, 1981). Within 100km of the ridge axis hydrothermal plume fall out dominates the sediments. This plume coincides with the distribution of metalliferous sediments along the ridge flanks (Bostrom & Peterson, 1969). The distribution is consistent with the local hydrography as mapped by Reid (1981), with bottom currents transporting the hydrothermal components westward north of 30^{o}S (Dymond, 1981).

These metalliferous sediments are potentially the source of much information about the oceans in which they were formed.

1.2 Hydrothermal activity and metalliferous sediment formation

Hydrothermal activity is centred around the global Mid Ocean Ridge (MOR) system. Fluid circulates through the ocean crust, and high temperature fluid is ejected at hydrothermal venting sites. There is also a significant degree of low temperature fluid circulation through the ridge flanks, which have been shown to play an important role in heat and chemical fluxes (e.g. Kadko et al., 1994; Elderfield & Schultz, 1996)

Figure 1.2.1 shows a schematic of a hydrothermal vent. High temperature fluids expelled at the vent site are considerably less dense than the ambient seawater and rapidly rise in a buoyant plume. The temperature of these fluids is usually greater than 200^{o}C, up to a maximum of ~405^{o}C (German & Von Damm, 2004). These plumes can typically rise to a height of 150 – 400m (Lupton, 1995)

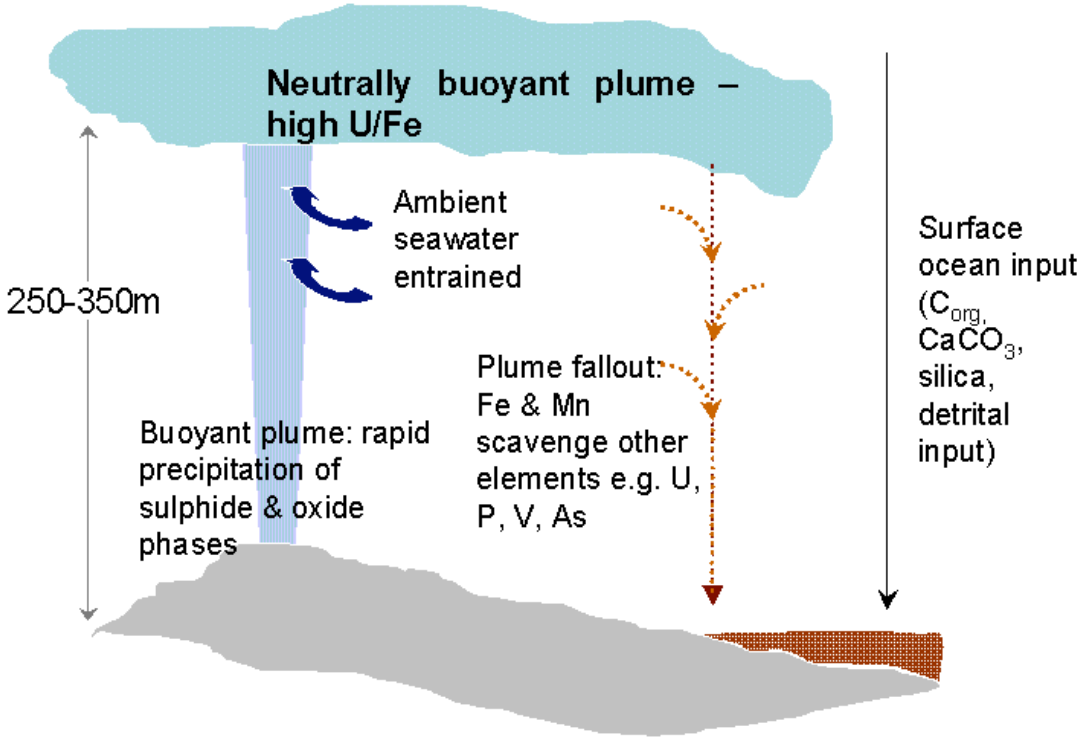

Figure 1.2.1: Schematic of a hydrothermal plume. As the buoyant plume rises, seawater becomes entrained, cooling the plume until it becomes neutrally buoyant and begins to spread laterally. Fe-oxyhydroxides and sulphides are precipitated rapidly from the buoyant plume. Uranium co-precipitates with the Fe-oxyhydroxide fallout.

Circulating hydrothermal fluids are chemically altered in their passage through the ocean crust and are chemically distinct from seawater. Hydrothermal circulation has an important role in the regulation of chemical budgets through the whole ocean (e.g. Elderfield et al., 1993; Elderfield & Schultz; 1996).

As the buoyant plume rises it entrains ambient seawater and as the buoyant plume cools, particulate matter rapidly precipitates. The plume eventually reaches neutral buoyancy with the surrounding seawater and then spreads laterally. The thickness of the plume can be several hundred metres. The neutrally buoyant plume will travel in the prevailing direction of the bottom currents, moderated by the topography. For fast spreading ridges with no axial valley like the EPR, hydrothermal plumes can travel over vast distances, up to several thousand km. Extensive ^{3}He and Mn anomalies have been observed as far as 2000km from the ridge crest (Lupton et al., 2004; Lupton, 1995; Klinkhammer & Hudson, 1986; Lupton & Craig, 1981; Reid, 1981).

Hydrothermal vent discharges are dominated by high levels of Fe(II) particulate matter. In the near field close to the hydrothermal source, this precipitates out immediately, extremely rapidly, as sulphides e.g. at TAG this process has been estimated to happen as quickly as within 15 seconds of the plume beginning to rise (Rudnicki & Elderfield, 1993).

Further removed from the hydrothermal source, oxidation of the plume Fe forms predominantly Fe(III) (hydr)oxides. As these precipitate from the plume, they undergo numerous scavenging reactions with the dissolved constituents of seawater, altering the trace elements concentrations of the plume particles (Feely et al., 1987,1990a,b, 1992; Dymond & Roth, 1988; Trocine & Trefry, 1988; Trefry & Metz, 1989; German et al., 1990, 1991; Metz & Trefry, 1993). The subsequent hydrothermal fall out settles out of the plume gravimetrically and forms the basis of highly trace element enriched metalliferous sediments. The alterations that occur during plume formation, transit and deposition could potentially be imprinted on the underlying sediments.

1.3. Trace element distributions in marine sediments

Fe(hydr)oxide precipitation from hydrothermal sources is not considered to be a significant flux of Fe (hydr)oxides in the marine environment (Canfield, 1998; Poulton & Raiswell, 2002). However the reactivity of these precipitates in the water column is such that the scavenging of dissolved trace elements (e.g. U, P, V and As) from seawater is highly efficient (e.g. Berner, 1973; Trocine & Trefry, 1988; Olivarez & Owen, 1989; Trefry & Metz,1989; Feely et al., 1991; German et al., 1990; Edmonds & German, 2004) and a potentially important part of the chemical budgets of these elements. The behaviour of these trace elements post deposition is dependent on composition of these sediments, local redox conditions (e.g. Barnes & Cochran, 1990) and the effects of non-steady state conditions (e.g Thomson et al, 1996; Thomson et al., 1990)

1.3.1 Uranium

Uranium and the uranium-series nuclides are useful as tracers for continental weathering (Henderson & Anderson, 2003), hydrothermal processes (Cochran, 1992), and as chronometers for coral growth (Ku et al., 1990) and many other systems such as the dating of basalts (Hegner et al., 1984). Authigenic uranium content is also used as a proxy for deepwater oxygen concentrations (Francois et al., 1997) and past productivity (Kumar et al., 1995).

The uranium-series nuclides primarily enter the ocean system via riverine input (Dunk et al., 2002). The primary sink of uranium is the various methods of sequestration to the ocean sediments (Cochran, 1992). In many sediment types the concentration of uranium can become elevated (e.g. Klinkhammer & Palmer, 1991; Rydell et al., 1974; Schaller et al., 2000; Shimmield & Price, 1988; Thomson et al., 1990) depending on the type of sediment and how this affects uranium geochemistry, particularly the redox state.

The most common oxidation states of uranium in the natural environment are U(IV) and U(VI) (Bourdon et al., 2003). Uranium geochemistry is strongly influenced by the oxidation state of the local environment, and in oxygenated seawater uranium is stably dissolved in the U(VI) form as a uranyl carbonate species, $UO_2(CO_3)_3^{4-}$ (Anderson et al., 1989), in relatively high concentrations (~14nM) in comparison to the other transuranic elements (Chen et al., 1986). Under reducing conditions U(VI) is reduced to the insoluble U(IV), a particle reactive species that is rapidly removed from solution. The uranyl carbonate species has a mean oceanic residence time (MORT) of approximately 4×10^5 years (Cochran, 1992) and is a conservative element in the oceans. As the MORT of uranium is so much greater than the mixing time of the oceans (ca. 10^3 years), this means the oceans are well mixed with respect to uranium (Dunk et al., 2002).

The uranium input and removal fluxes balance within the estimated errors (Dunk et al., 2002). However these errors have a significant magnitude, therefore the uranium mass balance remains uncertain. The major fluxes of uranium are summarised in Table 1.1

Table 1.1: The preanthropogenic uranium budget of the oceans (after Dunk et al., 2002)

		(Mmol/year)
Input of U to the ocean		
Major	Riverine (surface + base flow)	42.0±14.5
	Sub surface groundwater	9.3±8.7
Minor	Aeolian	1.8±1.1
Coastal zone retention		-11.2±5.6
Total		**41.9±17.8**
Removal of U to the ocean		
Major	Anoxic sediments	11.6±6.0
	Suboxic sediments	15.3±10.6
	Biogenic carbonate	13.3±5.6
	Basalt alteration	5.7±3.3
Minor	Metalliferous sediment	1.0±0.8
	Opaline silica	0.6±0.3
	Pelagic clay	0.4±0.2
Total		**47.9±13.8**

Sediments in the southeast Pacific show enrichment in U with respect to normal pelagic sediments with concentrations of up to 30ppm (Rydell et al., 1974; Schaller et al., 2000; Shimmield & Price, 1988; Dunk, 2004). Detrital concentrations of uranium are only ~1-4ppm (Ku, 1966). There are a number of different mechanisms by which uranium can become enriched in marine sediments.

Uranium enrichment via reductive processes is common in anoxic environments because the reduction of U(VI) to U(IV) produces a particle active insoluble species. Deposition of authigenic uranium occurs around the depth of Fe remobilisation in anoxic sediments (Morford & Emerson, 1999). A combination of the organic carbon rain rate, bottom water oxygen concentration and bioturbation determines how extensive the penetration of oxygen into the pore waters below the sediment water

interface is, and how reducing the sediment is. Authigenic uranium enrichment becomes significant where the penetration of oxygen into the sediments is less than 1cm (Morford & Emerson, 1999).

As a result of the reduction of uranium, and thus its immobilisation in the solid phase, the pore water concentration should show depletion at depth (Barnes & Cochran, 1990). Some studies (e.g. Cochran et al., 1986; Colley et al., 1989; Kolodny & Kaplan, 1973; Toole et al., 1988) have reported pore water concentrations in suboxic to anoxic regions that are greater than the overlying water. Barnes & Cochran (1988; 1990) propose that some of these values can be explained by oxidation of the reduced uranium on the sediment surfaces, as artefacts introduced during processing. They suggest pore water samples taken in situ (by probe or harpoon) as more reliable than porewater U analyses from sediment cores (Barnes & Cochran, 1990).

The enrichment in the solid phase uranium content is particularly evident in sediments where nitrate reduction was almost complete and Mn reduction is occurring (Barnes & Cochran, 1988). It has been proposed that, if uranium reduction is the cause of the solid phase profile, then this reduction, coupled to the oxidation of organic matter, must occur at a pE intermediate between that of Mn reduction and Fe reduction (Cochran et al., 1986). Other potential explanations of the porewater depletion include a U(V) intermediate (Kniewald & Branica, 1988). If sulphate reduction is occurring in the sediment, then the uranium depletion in the porewaters is even more pronounced (Barnes & Cochran, 1990). Reduction of uranium and removal from the porewaters creates a down-core diffusive flux from the overlying water into the sediments. The diffusive flux can be represented in terms of Ficks' first law as applied to sediments (Berner, 1981).

$$J_u = -D_s \Phi \left(\Delta U / \Delta X \right)_{x=0}$$

J_u = ^{238}U flux into sediments (dpmcm^{-2}ky^{-1} or µgcm^{-2}ky^{-1})
D_s = Molecular diffusion coefficient for U corrected for tortuosity (cm^{-2}y^{-1})
Φ = Porosity
x = depth (cm)
$\Delta U/\Delta X$ = gradient dissolved U at x=0

Deep-sea sediments are often oxic to considerable depth because of low carbon supply to the seafloor and high bottom oxygen content. The depth of the oxic/post-oxic

boundary is responsive to the sedimentation rate in deep-sea sediments. Reconcentration peaks of redox sensitive elements have been observed in discontinuously accumulated turbidites (Thomson et al., 1993). Periodic emplacement of organic carbon rich turbidites that are subsequently oxidised by progressive penetration of oxygen through the turbidite layer, leads to enrichment of U at the 'burn-down' front (Colley et al., 1984).

An episode of hydrothermal activity can also lead to uranium enrichment in sediments Metalliferous sediments receive two distinctive inputs from hydrothermal systems – fallout from the plume (Fe-oxyhydroxide particles and sulphides) and their oxidation products from mound features via mass wasting events (Mills et al., 1993).

Uranium is quantitatively stripped from seawater during hydrothermal circulation through young oceanic crust, where it is reduced to the insoluble (IV) valence state, meaning vent fluid is depleted in uranium. Sulphides that precipitate from the plume are correspondingly poor in U. However U is co-precipitated with Fe (hydr)oxide phases and therefore metalliferous sediments forming from this phase can become enriched with seawater uranium. (Mills et al., 1994) These metalliferous sediments usually exhibit seawater U isotope signatures (Mills et al., 1994). Further enrichment can occur due to the circulation of low temperature hydrothermal fluid-seawater through the sediment (Dunk et al., 2002)

Redox sensitive trace metals, such as uranium, iron, and manganese are redistributed during non-steady state diagenesis. Uranium develops a diagenetic concentration peak in reducing conditions i.e. just below the oxidation front, and as this front moves further down into the sediments the uranium is constantly remobilised in front of it. The uranium peaks formed remain as relict indicators of this oxidation front process, known as "burn down" (Colley & Thomson, 1985).

Reconcentration peaks also appear where sedimentation rates have changed, causing the oxic/post-oxic boundary to be localised at the same depth for a length of time e.g. in glacial/interglacial transitional sediments (Thomson et al., 1996). Changes in the sediments flux are apparent at the glacial/interglacial boundary in cores from the Armorican Seamount, shown by the age/depth relationships of Heinrich events

(Thomson et al., 1996). The sediments in these cores show a sequence of peaks in redox-sensitive elements in order of Eh value; Mn, Mo; Fe, As, P; Se, V; Cd; U which form at successive depths due to localisation of the oxic/post-oxic boundary at a particular level in the sediments.

1.3.2 Behaviour of some other oxyanions: Phosphorus and Vanadium

Uranium is not the only oxyanion that is scavenged by hydrothermal particulate matter and deposited in the metalliferous sediments. Phosphorous and Vanadium are present in seawater as HVO_4^{2-} and HPO_4^{2-} and also undergo scavenging from seawater by the Fe and Mn phases.

Dissolved P in the ocean is an important micronutrient that is potentially one of the limiting factors on primary production (e.g. Karl et al., 1993). There have been numerous evaluations of the global P cycle, summarised in Table 1.3.1. The largest marine input of P is riverine, with only a minor aeolian flux (Duce, 1986). Marine sedimentation is a significant sink of P. The uptake of dissolved phosphate from seawater by hydrothermal plume particles and hydrothermal circulation through both the axis and ridge flanks is an important sink in the global P cycle (Berner 1973; Froelich et al.,1982, Feely et al., 1990, Wheat et al., 1996). Hydrothermal processes are a significant sink for phosphorus, potentially removing up to 33% of the global riverine input (Wheat et al., 1996).

P enrichment in the hydrothermal plume occurs quickly i.e. within minutes of formation of the Fe oxide phases (Feely et al., 1992; 1994b), suggesting primarily a co-precipitation mechanism for P enrichment rather than adsorption (Rudnicki & Elderfield, 1993; German et al., 1991). The extent to which P is scavenged relates to both the dissolved concentration in seawater and the concentration of Fe and the molar ratio in newly formed hydrothermal particles behaves predictably on a global scale.

In the absence of diagenetic processes, plume particle P/Fe ratios (and other oxyanions) should be recorded in the sediment column (German et al., 1997; Feely et

al., 1998; Schaller et al., 2000). However under suboxic and anoxic conditions soluble V(V) is made insoluble by reduction to the particle reactive V(III) (similarly to the reduction of soluble U (VI) to the particle reactive, insoluble U(IV)). This process is potentially a source of enrichment to the sediments (e.g. Emerson & Huested, 1991). Conversely, remobilisation of P is common in mildly reducing hemipelagic sediments (Gieskes, 1983). So the redox status of the sediments is critical to the degree of preservation of the plume material, and reductive processes can cause redistribution.

Table 1.3.1 The Preanthropogenic budget of P (Wheat et al., 1996)

		Flux (10^{10}mol/year)
Input of U to the ocean		
Major	Riverine – dissolved *Froelich et al., 1982*	3.0
	Riverine - soluble particulate *Berner & Rao., 1994*	4.8
Minor	Aeolian *Duce (1986)*	0.3
Total		**8.1**
Removal of P from the ocean		
Sedimentary *Ruttenburg (1993)*	Organic	-4.1
	Loosely sorbed	-1.3
	Authigenic	-2.2
Plume particles	Upper limit *(Wheat et al., 1996)*	-0.55 to -1.00
	Lower Limit *(Dunk, 2004)*	-0.14 to -0.26
Hydrothermal alteration *(Dunk, 2004)*	Ridge Axis	-0.01
	Ridge Flank	-0.65
Total		**-8.4 to -9.3**

1.4 Aims and objectives

Air-sea exchange of CO_2 in the southeast Pacific is of importance in the global CO_2 budget. Changes in circulation and ocean chemistry in this area have been a focus of interest for many years for their potential control on global climate. The EPR is also the location of intense hydrothermal activity and huge metalliferous sediment deposits that are enriched with trace elements derived from seawater by the hydrothermal plume.

This work takes a 800ka record from the EPR ridge flank that has shown extreme enrichment of trace elements, in particular uranium, in previous studies that have not been explained conventionally. The main aim of this work is to understand the mechanisms controlling the distribution of these trace elements and oxyanions in southeast Pacific sediments. Understanding distribution of these elements may allow their use as proxies for past ocean behaviour

The key objectives of this work are to

- Establish the bulk sediment composition for the core and compare this with regional trends
- Establish a coherent age model for accumulation of the sediments and assess the degree of lateral transport and the impact this has on sedimentation
- Identify the speciation of the Fe and Mn content in the different sedimentary phases and investigate the likely pathway of alteration post burial
- To identify the phase associations and degree of fractionation of the trace elements between the different sedimentary phases and evaluate the current redox status in the sediments.
- To use oxyanion distributions and Fe speciation in the sediment to establish variability in the redox status of the sediment through time, and to use these redox relationships to evaluate the effectiveness of the oxyanions as proxies for past ocean conditions.

Chapter Two: Analytical Methods

This chapter gives information on the sample collection of the core GS-7202-35 and techniques used for data analysis. Unless otherwise stated all sample preparation used Fisher Aristar grade acids and Millipore Milli-Q water (having a resistivity of 18.2 MΩ.cm). All masses were determined gravimetrically (Unless otherwise stated accurate to 0.0001g)

2.1 Sample processing

2.1.1 Sample collection and processing

Samples were collected during cruise GS-7202 of the University of Miami (Spring, 1972) from 82km west of the EPR ridge axis at 14^{o}47.9'S, 113^{o}30.1'W from a water depth of 3044m and comprise trigger and piston cores 1.7m and 8.47m in length respectively. The core is stored in the Miami Core Repository at 4^{o}C.

Cores were sampled in 5cm increments at Miami core repository. Depth integrated samples were dried in a thermostatically controlled oven at 70^{o}C for 48 hours then homogenised and ground in an agate mill with planetary spheres for 12-15 minutes. Small samples of unground material were retained for SEM and XRD analyses.

2.2 Sediment digestions

Several of the analytical techniques used required complete digestion of the samples prior to analysis.

2.2.1 Digestions for ICP-MS and ICP-AES

Samples were subjected to a total sediment digest procedure prior to analysis by ICP-MS and ICP-AES. Approximately 100mg of ground dried sediment was directly transferred to a 15ml Savillex Teflon scintillation vial and subjected to a 4 stage combined $HClO_4$/HF digestion procedure (Table 2.2.1).

Table 2.2.1: Protocol for total digestion of sediment samples by HF/$HClO_4$ attack

Stage	Reagents	Conditions
1	5 ml Aqua Regia	Reflux 90°C overnight, dried down at 100°C
2	4ml HF/ 3ml $HClO_4$	Reflux overnight at 150°C and dried down at 170°C. On observation of white fumes, dry down temperature increased to 190°C
3	4 ml $HClO_4$	Dry down immediately at 190°C
4	10g 8M HNO_3	Samples dissolved in HNO_3 and placed in a thermostatically controlled oven at 60°C overnight

After digestion samples were quantitatively transferred to 125ml Nalgene bottles and made up to a total weight of ~100g constituting a 1000-fold dilution of the original sediment sample.

2.2.2 Digestions for α-spectrometry

Approximately 0.5g dried ground sediment was directly transferred to a 15ml Savillex Teflon scintillation vial and subjected to the total digestion procedure outlined in table 2.2.1 in the previous section. Prior to digestion, each sample was spiked with a tracer for U-232 and Th-229 (GY/RAM/391, 40µl addition and SOC/RAM/283, 50µl addition, respectively). Exact masses of spikes used were determined gravimetrically (accurate to 0.00001g)

Two 0.5g digestions were completed for each sample then combined to give a total dissolution of 1g total for alpha spectrometry which was made up to 20g using 8M HNO_3. These solutions were then subjected to chemical separations to give a thorium and uranium fraction.

After digestion a 2 stage chemical separation was carried out to separate the uranium and thorium isotopes. Stage 1 was carried out using UTEVA resin in a 0.5cm diameter column, 4cm length (Table 2.2.2). The Th fraction was subjected to a second

extraction using Anion Exchange resin to ensure total removal of all Ca ions (Table 2.2.3).

Table 2.2.2 Stage one of chemical separation to isolate U and Th isotopes, carried out using 4cm UTEVA column with 0.5cm Ø

Step	Reagents and conditions
1 : Wash	UTEVA resin loaded into column an washed with 20ml 6M HCl, followed by 20ml 8M HNO_3
2 : Loading	Sample loaded in 8M HNO_3, washed through with a further 20ml 8M HNO_3
3 : Th elution	Th fraction eluted using 30ml 6M HCl
4 : U elution	U fraction eluted using 20ml 0.2M HCl
5 : Drying	U fraction dried down and brought up in 1ml 10% HCl for electroplating Th fraction dried down and brought up in 20ml 8M HNO_3 for further cleaning extraction

Table 2.2.3 Stage two of chemical separation, cleaning of Th fraction using 4cm Anion exchange resin column with 0.5cm Ø

Step	Reagents and procedure
1: Wash	Resin washed with 20ml HCl followed by 20ml HNO_3
2: Loading	Th fraction from separation 1 loaded in 20ml 8M HNO_3, washed with further 50ml 8M HNO_3.
3: Th elution	Th fraction eluted in 30ml 9M HCl
4: Drying	Sample dried down and brought up in 1ml 10% HCl for electroplating

5ml Ammonium oxalate was added to U and Th fractions followed by a rinse of 5ml MQ water, then samples were electroplated for counting.

2.3 Analytical techniques

2.3.1 X-ray fluorescence (XRF)

Geochemical analyses were carried out using a Phillips PW1400 fully automatic wavelength dispersive XRF on 27mm diameter pressed powdered pellets for trace

elements and 27mm diameter beads (Li tetraborate flux: sample 4:1) for major elements. Pellets were calibrated using matrix-matched standards comprising mixtures of USGS standards MAG-1, JLs-1, GXR-1, NIM-L, BE-N, SDo1, NOD-P-1 and NOD-A-1 (See Table 2.3.1). Precision was assessed by calculation of %RSD of 5 repeat analyses of unknown samples and is better than 2% for all elements of interest except Ti (%RSD = 3.5%) which is close to detection limit. Raw data is located in Appendix 1. Accuracy and data conflict with ICP-AES is discussed in detail in Appendix 2.

Table 2.3.1 Standard compositions for X-Ray Fluorescence Pellets were calibrated using matrix-matched standards comprising mixtures of USGS standards MAG-1, JLs-1, GXR-1, NIM-L, BE-N, SDo1, NOD-P-1 and NOD-A-1.

Std	SiO2 (%)	TiO2 (%)	Al2O3 (%)	Fe2O3 (%)	MnO (%)	MgO (%)	CaO (%)	K2O (%)	Na2O (%)	P2O5 (%)	Co (ppm)	Cr (ppm)	V (ppm)	I (ppm)	Ni (ppm)
1	11.0	0.28	4.21	5.12	5.75	2.09	35.28	0.86	1.02	0.38	750.48	21.08	212.80	75.00	1537.17
2	14.9	0.11	2.71	8.18	3.04	0.86	37.00	0.38	0.22	0.09	184.58	9.66	74.40	0.00	1088.36
2a	17.8	0.13	3.63	8.06	0.03	0.84	36.86	0.57	0.35	0.07	7.02	17.42	40.00	30.40	20.60
3	17.6	0.23	5.05	3.87	0.03	1.25	36.86	1.06	0.98	0.07	7.85	30.12	47.00	95.00	20.47
4	11.3	0.08	2.16	5.88	1.15	0.78	42.38	0.29	0.24	0.07	70.65	9.92	39.50	15.20	413.48
5	17.2	0.25	5.30	3.28	0.51	1.40	36.60	1.14	1.11	0.10	69.95	31.98	62.60	106.40	147.03
6	20.7	0.24	5.54	4.93	5.70	1.69	29.60	1.34	1.53	0.57	341.35	22.45	122.50	76.00	2023.79
7	24.4	0.26	5.81	7.89	4.32	0.97	26.50	1.74	2.13	0.11	254.54	14.01	108.91	7.60	1492.96
8	32.4	0.85	7.80	10.19	0.23	3.80	21.23	1.95	2.68	0.32	23.14	103.56	104.96	7.60	85.67
9	1.8	0.09	1.55	1.47	3.01	0.82	50.10	0.10	0.18	0.07	179.88	8.39	53.40	0.00	1076.28
10	3.1	0.14	3.30	2.39	0.39	0.66	49.95	0.09	0.10	0.04	24.55	18.97	28.40	7.60	145.56
11	5.2	0.29	6.60	3.90	1.14	0.76	44.46	0.22	0.27	0.06	71.47	35.58	61.50	19.00	424.12
12	6.8	0.1	2.0	1.8	1.9	1.0	46.8	0.4	0.5	0.1	114.2	12.4	44.1	38.0	676.4
13	8.3	0.1	2.2	2.8	1.9	1.0	45.2	0.4	0.5	0.1	114.5	12.7	46.5	38.0	677.6
14	10.7	0.1	2.6	4.5	1.9	1.0	42.4	0.4	0.5	0.1	114.9	13.2	50.5	38.0	679.6

Std	Sc (ppm)	Cu (ppm)	Zn (ppm)	As (ppm)	Bi (ppm)	Tl (ppm)	Pb (ppm)	Ba (ppm)	Rb (ppm)	Sr (ppm)	Y (ppm)	Zr (ppm)	Nb (ppm)	Hf (ppm)	S (ppm)	Th (ppm)
1	3.5	272.4	155.5	1.9	0.1	0.1	207.8	496.6	29.8	514.2	33.4	25.2	2.4	0.8	780.0	2.4
2	1.4	1146.8	286.6	91.0	275.0	0.1	192.6	449.8	12.9	307.8	17.2	20.8	1.1	0.6	4794.0	3.1
2a	2.8	229.2	169.4	91.7	275.0	0.1	150.2	220.1	24.8	265.1	11.9	30.9	2.0	0.9	5106.0	4.0
3	5.1	66.0	75.6	27.2	69.1	0.2	43.9	177.1	44.3	246.4	10.6	41.7	3.6	1.3	3778.5	3.7
4	1.3	514.5	171.1	66.6	207.0	0.1	127.9	244.1	11.8	291.7	10.0	15.7	0.9	0.5	2146.5	1.2
5	5.4	55.2	67.8	14.0	27.7	0.2	39.4	198.4	47.0	273.8	12.4	42.6	3.8	1.3	3283.4	3.9
6	4.2	1787.0	329.5	25.0	69.3	0.3	133.1	681.8	52.2	320.1	34.1	55.1	5.3	1.6	924.5	40.4
7	2.0	1397.1	354.0	54.8	151.8	0.1	153.9	598.8	58.3	1215.4	23.5	2334.9	203.2	40.6	6245.7	15.7
8	7.5	150.1	206.1	55.2	151.8	0.1	93.9	486.5	70.0	1438.7	20.7	2399.9	229.4	42.0	6320.7	18.3
9	1.2	931.5	139.4	6.7	13.8	0.0	54.4	276.1	0.2	322.8	10.1	11.4	1.0	0.4	25.7	1.0
10	3.4	149.8	47.9	18.9	41.5	0.0	34.7	67.1	3.6	286.9	8.2	31.2	2.9	1.0	155.1	2.8
11	6.9	381.6	87.4	24.9	41.6	0.0	53.3	150.0	8.2	280.8	16.6	62.4	5.8	1.8	272.1	5.7
12	1.8	600.2	110.4	9.6	27.6	0.1	44.8	230.4	15.2	299.8	8.1	13.4	1.2	0.5	441.4	1.2
13	1.8	633.5	133.1	22.4	69.0	0.1	66.7	252.9	15.6	299.2	9.1	14.5	1.2	0.5	518.5	1.3
14	1.9	689.0	170.9	43.7	138.0	0.1	103.2	290.4	16.3	298.1	10.7	16.4	1.3	0.5	647.0	1.4

Std	U (ppm)	La (ppm)	Ce (ppm)	Mo (ppm)	Sn (ppm)	Sb (ppm)	W (ppm)	Ag (ppm)	Se (ppm)	Cd (ppm)	Hg (ppm)	Ge (ppm)	Ga (ppm)	Br (ppm)	Cl (%)
1	0.5	37.0	193.8	107.8	5.8	0.2	0.3	0.0	0.2	0.0	0.0	0.0	4.1	50.4	0.6
2	10.9	13.0	33.9	75.3	11.0	24.4	32.8	6.2	3.3	0.7	0.8	0.0	4.1	0.1	0.0
2a	11.1	8.1	17.4	14.4	11.3	24.5	32.9	6.2	3.4	0.7	0.8	0.0	5.7	20.3	0.3
3	4.9	13.1	27.4	8.0	3.7	6.3	8.6	1.6	1.1	0.2	0.2	0.0	6.6	63.0	0.8
4	6.8	7.2	18.0	29.6	8.3	18.3	24.7	4.7	2.5	0.5	0.6	0.0	3.4	10.2	0.1
5	3.4	16.2	43.4	15.1	2.6	2.7	3.7	0.6	0.7	0.1	0.1	0.0	6.7	70.6	0.9
6	30.7	32.2	80.5	115.7	4.0	6.3	8.6	1.7	1.1	0.2	0.2	0.1	7.7	50.4	0.6
7	12.2	69.9	95.5	101.4	7.8	13.5	18.1	3.4	1.8	0.4	0.5	0.0	15.1	5.1	0.1
8	12.8	79.0	101.0	18.3	8.3	13.6	25.3	3.4	1.8	0.4	0.5	0.3	19.4	5.1	0.1
9	0.5	15.6	34.9	51.3	0.8	1.4	1.8	0.3	0.2	0.0	0.0	0.0	1.5	0.0	0.0
10	1.5	20.0	32.0	8.6	2.4	4.1	5.4	0.9	0.5	0.1	0.1	0.1	4.2	5.1	0.1
11	2.1	41.1	66.5	24.3	3.1	4.5	5.9	0.9	0.6	0.1	0.1	0.1	8.1	12.6	0.2
12	1.0	9.8	24.6	38.6	1.4	2.5	3.4	0.6	8.7	0.1	0.1	0.0	2.3	25.2	0.3
13	2.0	10.0	25.1	39.2	3.1	6.2	8.3	1.6	21.5	0.2	0.2	0.0	2.7	25.2	0.3
14	3.8	10.4	25.9	40.1	5.8	12.3	16.5	3.1	42.9	0.4	0.4	0.0	3.4	25.3	0.3

2.3.2 Inductively Coupled Plasma – Atomic Emission Spectrometry (ICP-AES)

A subset of samples was subjected to a total digestion procedure (Table 2.2.1) for analysis by ICP-AES. Analysis was carried out on a Perkin Elmer Optima 4300DV instrument with the assistance of Dr D. Green (NOC,S). Instrument calibration was carried out using a series of 5 matrix-matched standards Standard compositions are shown in Table 2.3.2. Data is corrected for instrumental blank and drift. Precision on previous analyses of unknown samples has been better than 3% (2σ).

Table 2.3.2 Composition of ICP-AES calibration standards

Element	Expected element range in samples (Based on XRF) (ppm)	Standard concentration in ppm				
		1	2	3	4	5
Si	0.5-12	0.5	1.25	2.5	5	12.5
Ti	0.05-0.2	0.02	0.05	0.1	0.2	0.5
Al	0.5-3	0.2	0.5	1	2	5
Mg	0.5-5	0.2	0.5	1	2	5
K	0.5-3	0.2	0.5	1	2	5
Na	5-40	2	5	10	20	50
P	0.5-8	0.4	1	2	4	10
Fe	5-80	5	12.5	25	50	120
Mn	2-40	2	5	10	20	50
Ca	20-300	20	50	100	200	300
Cr	0.002-0.02	0.002	0.003	0.006	0.015	0.03
V	0.02-0.4	0.02	0.04	0.075	0.2	0.4
Ni	0.01-0.2	0.01	0.02	0.038	0.1	0.2
Cu	0.02-0.5	0.025	0.05	0.094	0.25	0.5
Zn	0.01-0.2	0.01	0.02	0.038	0.1	0.2
As	0.02-0.4	0.02	0.04	0.075	0.2	0.4
Ba	0.2-2	0.1	0.2	0.375	1	2
Sr	0.2-2	0.1	0.2	0.375	1	2
S	0.2-3.5	0.2	0.4	0.75	2	4

USGS standard MAG-1 was used as a certified reference material to assess data quality. Accuracy and data conflicts are discussed in Appendix 2.

Calibration was carried out using a series of matrix-matched standards (Table 2.3.1).. Precision and data conflicts are discussed in detail in Appendix 2.

2.3.3 Inductively Coupled Plasma – Mass Spectrometry (ICP-MS)

ICP-MS analysis for Mo and U was carried out on a VG PlasmaQuad PQ2+ ICP-MS with the assistance of Dr J. A. Milton (NOCS). Prior to analysis the ICP-MS was tuned for optimum sensitivity and stability using a multi-element tuning solution containing Co, Y, In, La, Re, Bi, and U and left to stabilise.

Data was then acquired in peak-jumping mode, for a total of 2 minutes per sample/standard/blank analysis (4 x 30 second repeats). Data quality was monitored throughout the run by examination of the statistics produced after each analysis. Data is corrected for blank values, interference and instrumental drift and an internal (matrix) correction was applied to the data. Calibration was achieved using a multi-standard calibration based on the calculated values of 4 synthetic standards for each element (quantitatively diluted from traceable concentrate standards manufactured by Romil and SPEX).

2.3.4 X-ray diffraction patterns (XRD)

X-Ray Diffraction was used to determine the mineralogy of the samples. XRD analyses were carried out using a Phillips PW 1730 automated powder diffractometer using Co-K_α radiation (l = 1.7889Å) with the assistance of R. Williams (NOCS). Dry powder mounts were scanned between a 2θ of 3 – 76^o at intervals of 0.02^o and a scan rate of 0.2^{o}min^{-1}.

XRD patterns were obtained for a subset of 10 samples taken throughout the core. One sample was treated with acetic acid to remove the carbonate phase and a sodium citrate-dithionite buffer to remove oxyhydroxides (See table 2.3.3). The residue remaining was also analysed by XRF.

Table 2.3.3 Procedure for removing calcium carbonate and Fe-Mn oxyhydroxides

Stage	Procedure
1	Add 18ml of Mixed Reagent (comprising 8:1 0.3M Sodium Citrate: 1M Sodium Bicarbonate) to 0.5g wetted sediment
2	Incubate at 75^{o}C for 15 minutes
3	Add 3 aliquots of 0.4g Sodium dithionate with 4 minutes between additions
4	Add 10ml saturated NaCl and centrifuge at 3000rpm for 3 minutes. Discard supernatant fluid.
5	Repeat steps 1 – 4 using 9ml Mixed reagent and 0.2g sodium dithionate
6	Wash residue with 10ml MQ water and 0.5ml saturated NaCl solution

2.3.5 Scanning Electron Microscopy (SEM) and X-ray microanalysis

Samples representing low and high $CaCO_3$ (on basis of XRF Ca data) were analysed using Scanning Electron Microscopy. Polished sections were carbon coated and SEM analyses were carried out with the assistance of Dr R. Pearce, on a LEO1450 variable pressure SEM with a PGT energy dispersive X-ray microanalysis system. A visual inspection was carried out and X-ray point analysis carried out on any bright reflectors.

2.3.6 Inorganic Carbon and Total Carbon analyses

Selected samples were analysed for inorganic carbon content and total carbon using a UIC model 5012 carbon dioxide coulometer. 20mg of sample (accurate to ±0.0001g) was weighed directly into the sample measurement cup. Sample cups for total carbon were placed in a furnace prior to analysis to remove any potential organic carbon contaminant. Precision was assessed using multiple analyses of Fisher Analytical grade $CaCO_3$ and is +/- 2.2%. Standards and samples were dried overnight in a thermostatically controlled oven at 60^{o}C prior to analysis to ensure no water was present.

2.3.7 Stable Isotope Mass Spectrometry

$\delta^{18}O$ was measured on ground bulk sediment using a Europa Scientific GEO 20-20 Mass Spectrometer fitted with a Carbonate Automatic Preparation system (CAPS). (M. Bolshaw, NOCS). CO_2 evolved from the samples is measured with respect to a reference CO_2 stream (BOC). A linear drift correction is applied using in-house limestone standard H-1 at the beginning and end of each batch. Standard H-1 is calibrated against international standard NBS19.

2.3.8 Alpha spectrometry

U and Th isotope ratio data were collected using α-spectrometry. Prior to analysis the sediment was digested as described in section 2.2.2. Sample counting was carried out using an EG&G ORTEC Alpha spectrometer with the assistance of Dr P Warwick and Dr P Gaca (NOC,S). Samples were counted until ~200,000 counts had been recorded in the tracer region. Data was processed to identify the regions of interest then corrected for chemical recovery, background and counter efficiency.

2.3.9 Sequential leaches

A subset of samples was subjected to a sequential extraction procedure to investigate the partitioning of certain trace elements between different sediment phases. The extraction scheme was developed from Poulton and Canfield (2005) and is outlined in Table 2.3.4. The extraction separated the sediment into several operationally defined phases:

a) Easily reducible amorphous Fe (hydr)oxides (e.g. ferrihydrite)

b) Reducible Fe phases (e.g. Goethite & Haematite)

c) Non-reducible residue (calculated difference between bulk analysis and the sum of a+b)

Table 2.3.4: Sequential extraction procedure

Target phase	Extraction conditions
a) Easily reducible amorphous Fe(hydr)oxides (e.g. Ferrihydrite)	1M Hydroxylamine-HCl in 25% v/v acetic acid for 48 hours
b) Reducible Fe phases (e.g. goethite, haematite)	Sodium dithionite ($50gl^{-1}$) buffered to pH 4.8 with 0.35M acetic acid/0.2M sodium citrate for 2 hrs
c) Residual material	Estimated by difference between bulk analysis and a+b

Sequential extractions were performed by Paula Sanchez and data are reproduced by kind permission

2.4 Construction of a continuous record from piston and trigger cores

Samples from site GS 7202-35 comprise two cores, a trigger core and a piston core. An unknown quantity of sediment was missing from the top of the piston core; therefore there is potential for a degree of overlap between the sediment collected in the trigger core and the sediment collected in the piston core. The trigger and piston cores were combined into one continuous record using a combination of the downcore $\delta^{18}O$ (Figure 2.4.1; Figure 2.4.2) and several elements as measured by XRF (U and Mo). The overlap was initially assessed by visual inspection of the different records, then by calculating the Pearson correlation coefficient (r) between the core profiles at varying degrees of overlap (Equation 2.4.1). The best correlation for all records occurred when the piston and trigger core were overlapped by 27.5-32.5cm.

$$r = n(\Sigma XY) - (\Sigma X)(\Sigma Y)/(\sqrt{[n\Sigma X^2-(\Sigma X)^2][n\Sigma EY^2-(\Sigma Y)^2]}) \qquad \text{Equation 2.4.1}$$

Table 2.4.1: Calculated correlation between piston core and trigger core records at different degrees of overlap

Depth in Piston core trigger core starts (cm)	Overlap (cm)	Pearson correlation coefficient		
		$\Delta^{18}O$	U	Mo
115.5	52.5	0.468	0.366	0.610
120.5	47.5	0.659	0.685	0.548
125.5	42.5	0.766	0.840	0.924
130.5	37.5	0.903	NM	NM
135.5	32.5	0.964	0.911	0.684
140.5	27.5	0.918	0.940	0.650
145.5	22.5	0.709	0.730	-0.200
150.5	17.5	0.544	NM	NM

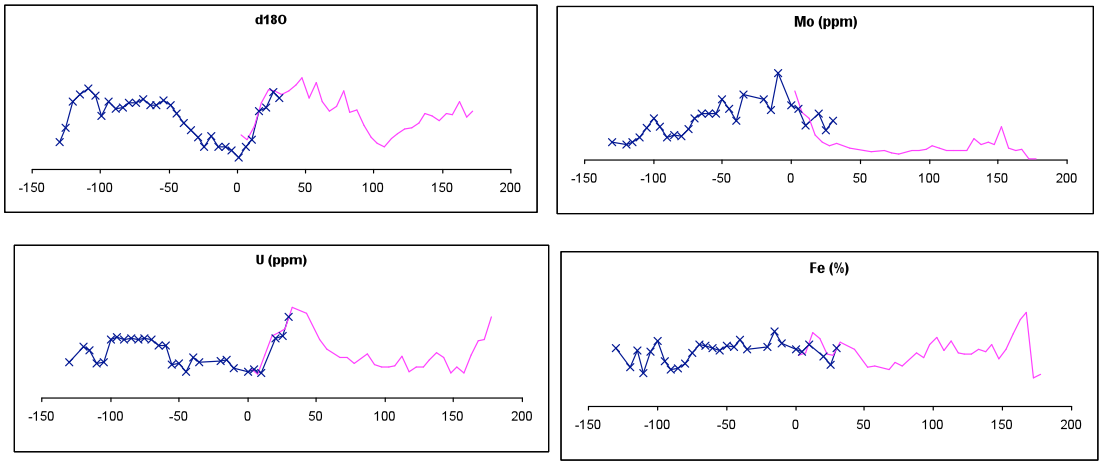

Figure 2.4.1: $\delta^{18}O$ and selected geochemical profiles at best calculated and visual overlap (30 cm)

a)

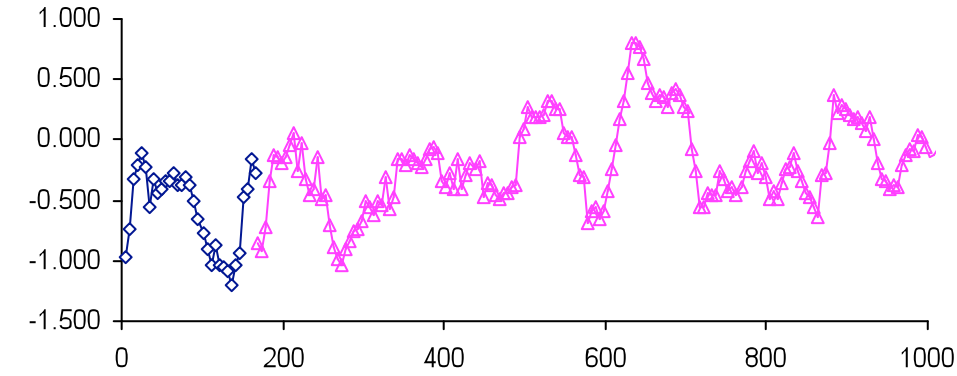

b)

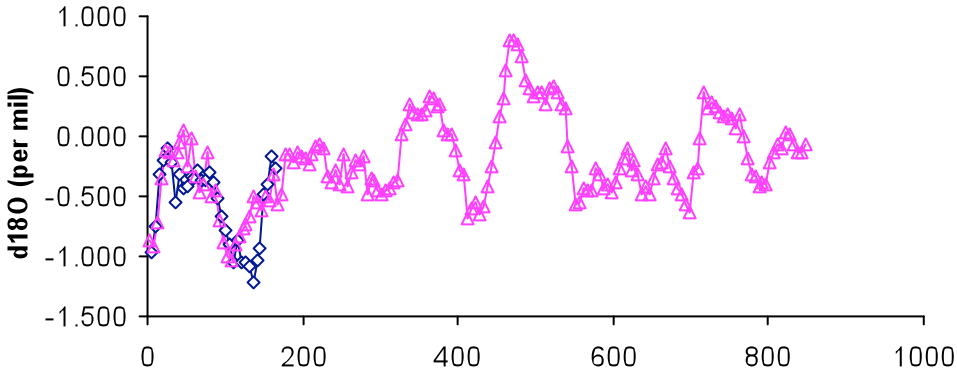

c)

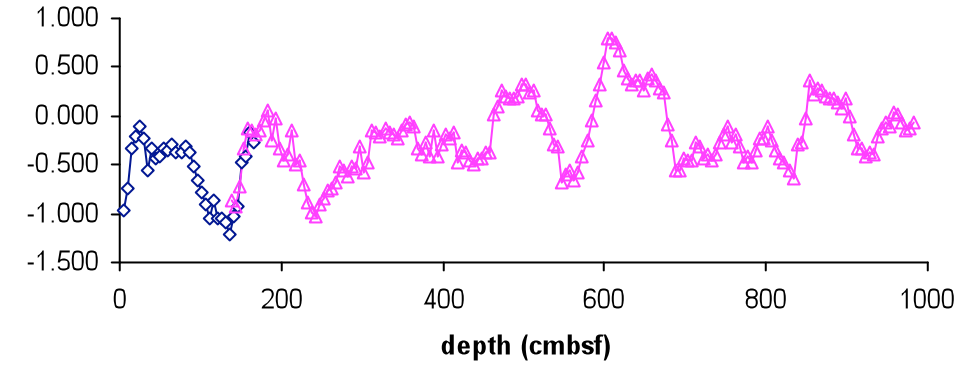

Figure 2.4.2: Downcore oxygen isotope profiles with a) No overlap of trigger (blue) and piston core (pink) b) Total overlap of trigger core and piston core c) Overlap 27.5 cm

Chapter 3: Sediment composition and accumulation at 14°S on the EPR

3.1 Aims

The overall aim of this chapter is to compare the bulk sediment composition from 14°S with the regional sediment trends and construct an accurate age model for the accumulation of sediment at this site. These aims are achieved by major, minor and stable isotope analysis of ~10m of sediment core. Sediment geochemistry is interpreted within the framework of previous studies in this region (Rydell et al; 1974, Bender et al, 1971; Schaller et al, 2000; Shimmield et al., 1988). The age model is determined by correlation of the bulk sediment $\delta^{18}O$ record with a composite time series.

3.2 Introduction: Sedimentation on the SEPR

The main sources and gross composition of sediments in the southern East Pacific Rise has been studied in detail (Dymond, 1981). The dominant component is biogenic (mostly calcareous) ooze. In the modern day eastern equatorial Pacific the calcite lysocline is ca. 3500m (Berger et al., 1976), although significant dissolution occurs at depths above the lysocline (e.g. Milliman et al., 1999). The calcite saturation horizon ($\Omega_{CALCITE}$, the point of thermodynamic equilibrium between calcite and the surrounding water mass) shoals significantly along the SEPR axis from ca. 3000m at 30°S to ca. 2000m at the equator (Feely et al., 2002).

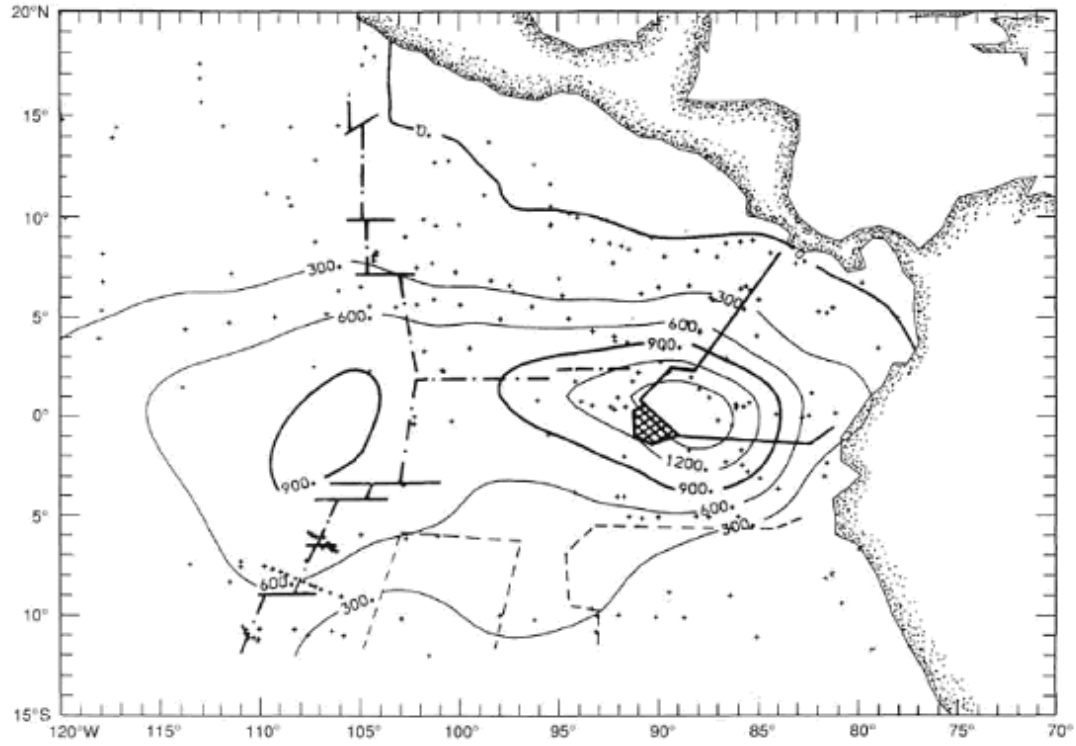

Figure 3.2.1: Distribution of calcite in the SEPR region (taken from Lyle, 1992) Contour units are mg.kg^{2}ka.

Carbonate accumulation is at its highest in the equatorial regions of the east Pacific (Figure 3.2.1). South of the equator, high accumulation rates are centred on the high topography of the EPR. As distance from the ridge axis increases, accumulation of carbonate decreases. The high rate of mass accumulation of carbonate suggests that in the eastern tropical Pacific, biological productivity has an important role in the calcite flux to, and burial in, the sediment. The sediment carbonate content is higher west of the EPR than in the basins to the east of the axis which lie closer to sources of terrigenous input, meaning carbonate preservation is higher is the Pacific Basin proper than in these basins. This is probably due to the less corrosive nature of the bottom waters west of the axis, where there is a lower organic carbon flux further from the continental region (Lyle, 1992).

Preservation of calcite at 14^{o}S can be calculated from the total alkalinity and total dissolved inorganic carbon in the bottom water using the program developed by Lewis and Wallace (1998) according to the equation

$(\Omega_{CALCITE}) = [Ca^{2+}][CO_2^{3-}]/K'sp$ Equation 3.2.1

where [Ca^{2+}] is estimated from salinity, [CO_2^{2-}] calculated from total alkalinity and dissolved inorganic carbon (ΣCO_2). This calculation assumes that bottom water temperature and salinity are the same as those measured at the EXCO sites east of the ridge crest at 14°S (Devey et al., 2000) (1.83°C and 35‰, respectively). Values for total alkalinity (2420 $\mu eqkg^{-1}$), ΣCO_2 (2320 $\mu molkg^{-1}$), dissolved silica (150 $\mu molkg^{-1}$) and phosphate (2.5 $\mu molkg^{-1}$) were taken from the JGOFS/WOCE dataset where line P18 (105°W) intersects line P21 (17°S). Results are shown in table 3.2.1. Values > 1 indicate that the water is saturated with respect to calcite.

Table 3.2.1: Degree of saturation of calcite (Ω)

Core ID	Crustal age (Ma)	Latitude	Longitude	Water Depth (m)	Ωcalcite
Core GS 7202-35	0.825	14°47'S	113°30.1'W	3044	1.03
EXCO 12	0.36	14°16.48'S	112°19.38'W	3047	1.03
EXCO 10 (Dunk, 2004)	1.9	14°33.67'S	111°15.20'W	3190	1.00

Within 100km of the ridge axis hydrothermal plume fall out is also extremely significant. Extensive ^3He and Mn anomalies are observed at 15°S as far as 2000km from the ridge crest (Klinkhammer & Hudson, 1986; Lupton & Craig, 1981; Reid, 1981). Figure 3.2.1 shows the extent of the ^3He anomaly along a transect of 17°S. This plume coincides with the distribution of metalliferous sediments (Figure 3.2.2) along the ridge flanks (Bostrom & Peterson, 1969). The distribution is consistent with the local hydrography as mapped by Reid (1981), with bottom currents transporting the hydrothermal components westward north of 30°S (Dymond, 1981).

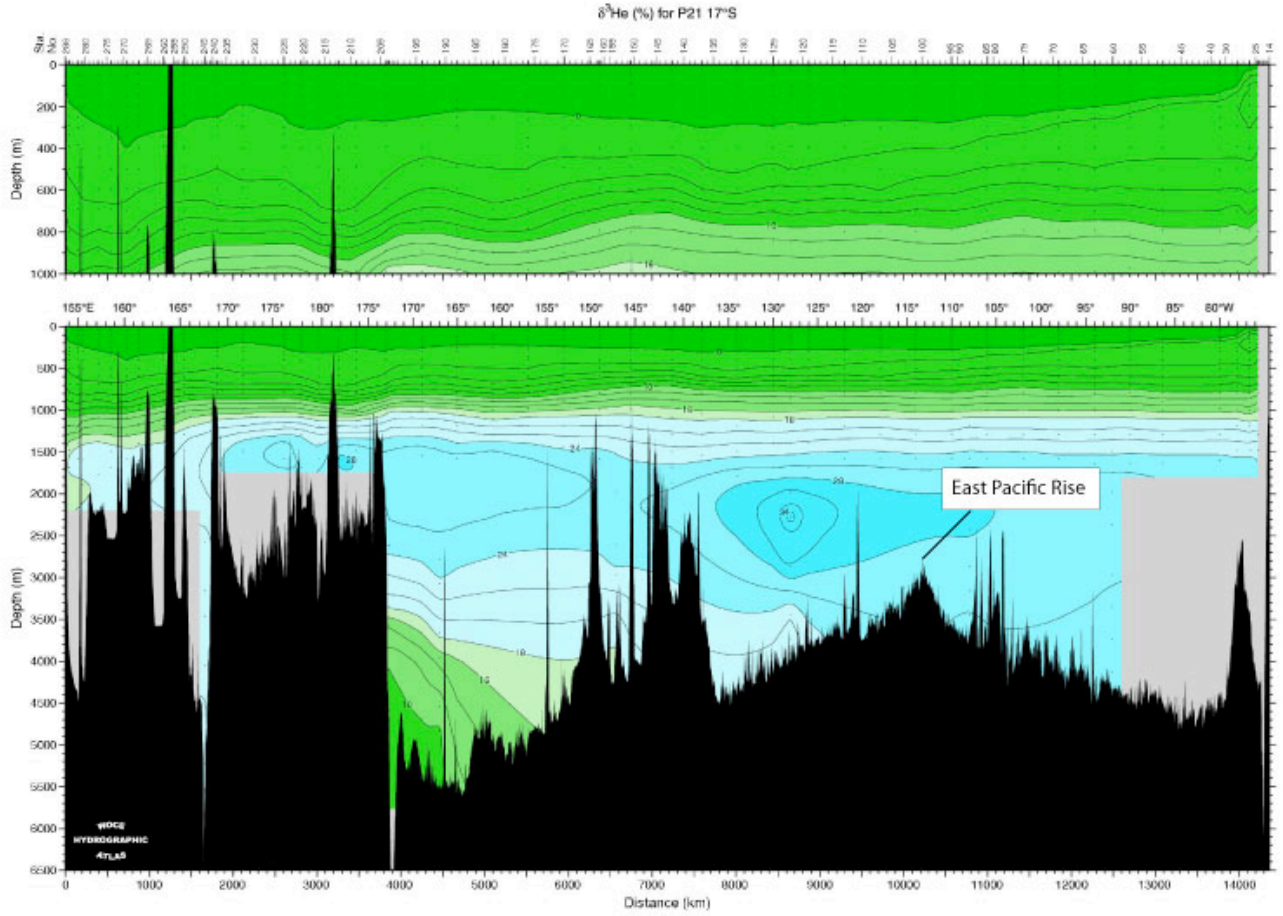

Figure 3.2.2: δ ^{3}He distribution along WOCE line P21 (17°S). Reproduced from the WOCE Pacific Ocean Atlas, (Talley, 2007)

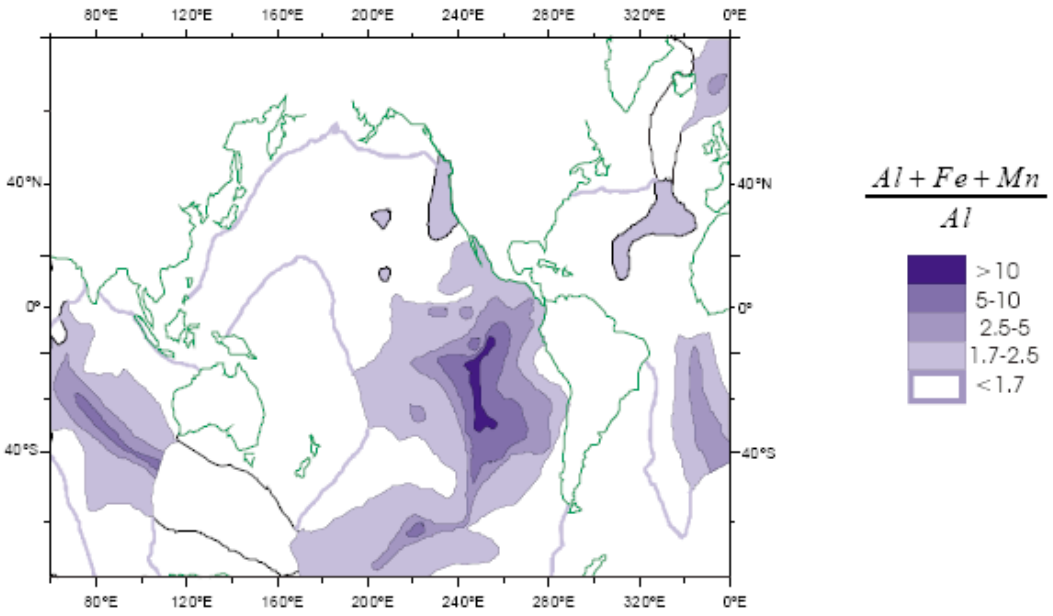

Figure 3.2.3: Distribution of metalliferous sediment in the SEPR region (Bostrom & Peterson, 1969), overlaid with the regional hydrography (Reid, 1981). High ratios indicate highly metalliferous sediments

Core GS 7202-35 was collected during cruise GS-7202 of the University of Miami (Spring, 1972) from 82km west of the EPR ridge axis at 14°47.9'S, 113°30.1W, water depth 3044m (Figure 3.2.3). Basement age inferred from a spreading rate of 143-150mmyr-1 (Cormier et al., 1996; Demets et al., 1994; Grevemeyer et al., 2002) is ~1.1Ma. The core was recovered from a bathymetric high elevated 50-200m over the surrounding area covered by a well developed sediment cap (~80km^2), selected to minimise any sediment focussing due to down slope sediment transport (Bostrom et al., 1974).

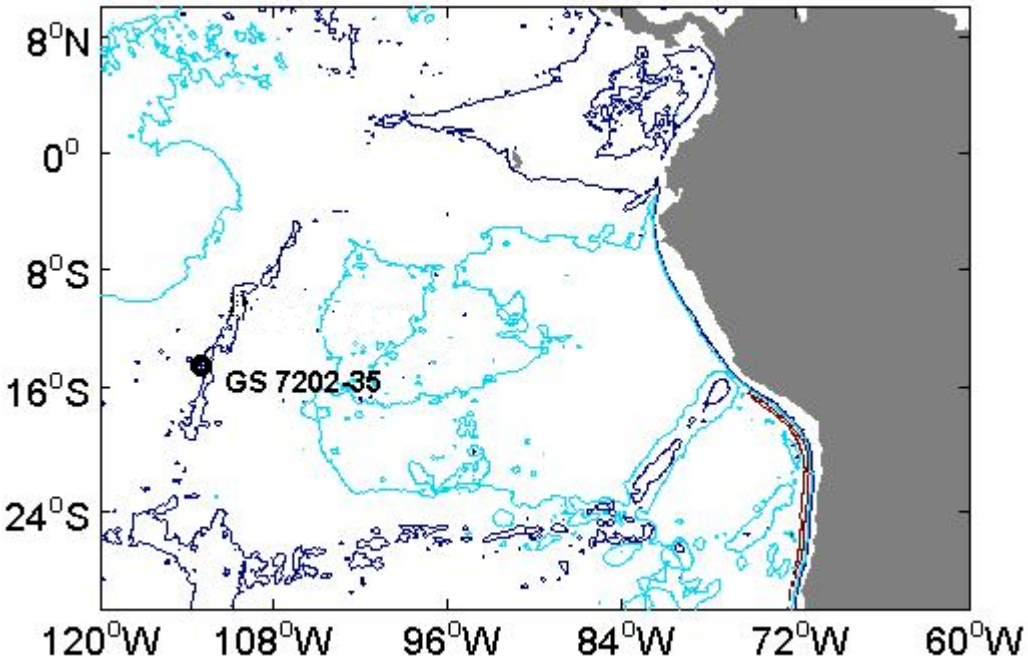

Figure 3.2.4: Map showing the location of core GS7202-35. Depth contours are at 1000m intervals from 3000m, the major bathymetric high is the East Pacific Rise.

A high quality seismic reflection and sediment echo sounding study across the EPR at 15°S indicates an average sedimentation rate of ~ 1cm ka^{-1} for the last 7Ma (Hauschild et al., 2003). This study indicates that in general sediment ponding occurs on the west flank of the EPR, implying transport and resedimentation by turbidity currents. However, it also suggests a lack of ponding on crust <2Ma. At 15°S the sediment appears to uniformly drape the seafloor with little indication of lateral transport (Hauschild, Pers. Comm; Figure 3.2.4). Two-way travel times (TWT) taken from seismic sections of the ridge crest indicate a sediment thickness of ~12-15m.

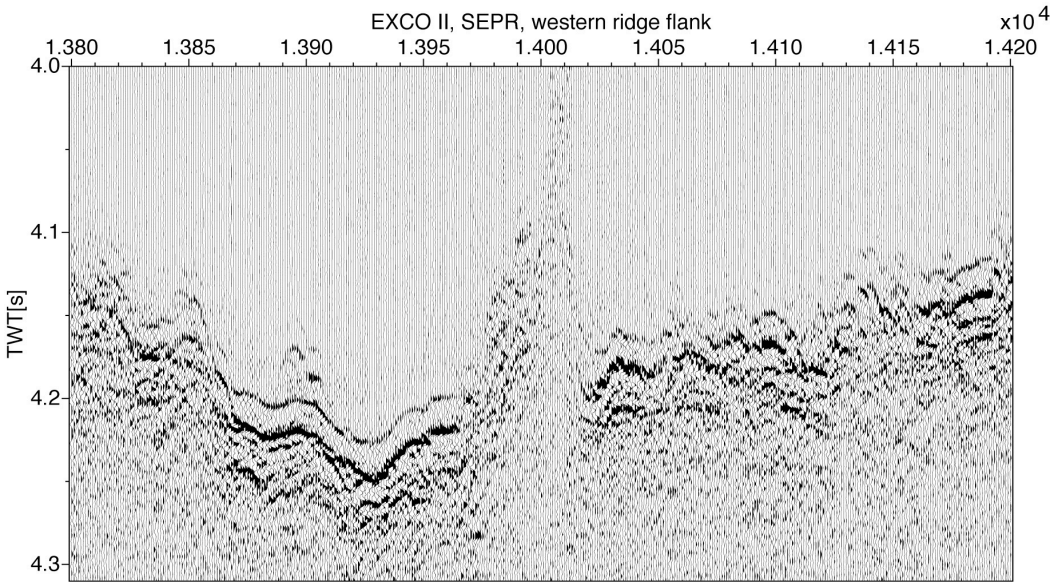

Figure 3.2.5: Seismic section of SEPR ridge flank showing two-way travel time (TWT) vs. distance across the EPR ridge. The even deposition of sediment is shown by the regular distance between the first two horizons either side of the ridge crest. (Hauschild, Pers Comm)

3.3 Results

3.3.1 XRD and mineralogy

XRD analyses were conducted at intervals through the trigger and piston cores (Figure 3.3.1). These showed only calcite and halite (from precipitated porewater salts) throughout the core. The high background is a result of the high percentage of Fe/Mn oxyhydroxides present. Chemical removal of the calcite and Fe-Mn oxyhydroxide material left a clay-like residue resembling illite [$K_{0.5}Al_2(Al_{0.5\text{-}0.75}Si_{3.25\text{-}3.5}O_{10})(OH)_2$] (Figure 3.3.2)

Samples representing low and high $CaCO_3$ (on basis of XRF Ca data) were analysed using Scanning Electron Microscopy. The sediments are predominantly calcite nanofossils (coccolithophores). Energy dispersive X-ray analysis of SEM images showed the presence of Fe/Mn micronodules and a small proportion of barite, with no evidence of other crystalline material.

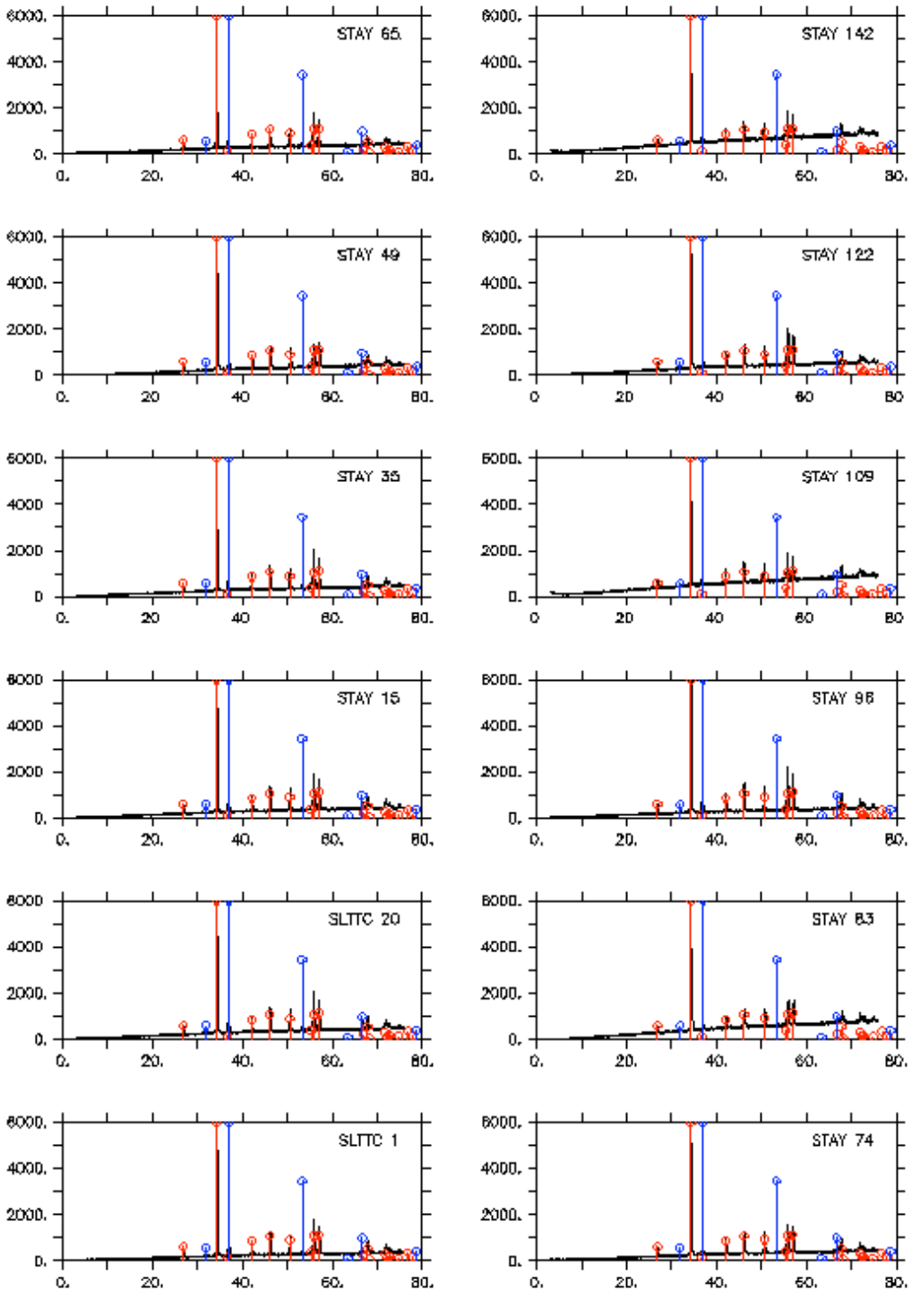

Figure 3.3.1: XRD patterns through trigger core and piston core. The expected peak positions of calcite (red) and halite (blue) are also indicated. Elevated background is indicative of a high level of amorphous Fe/Mn oxyhydroxides

Figure 3.3.2 XRD spectrum of residue after chemical removal of calcium carbonate and Fe/Mn hydroxide phases

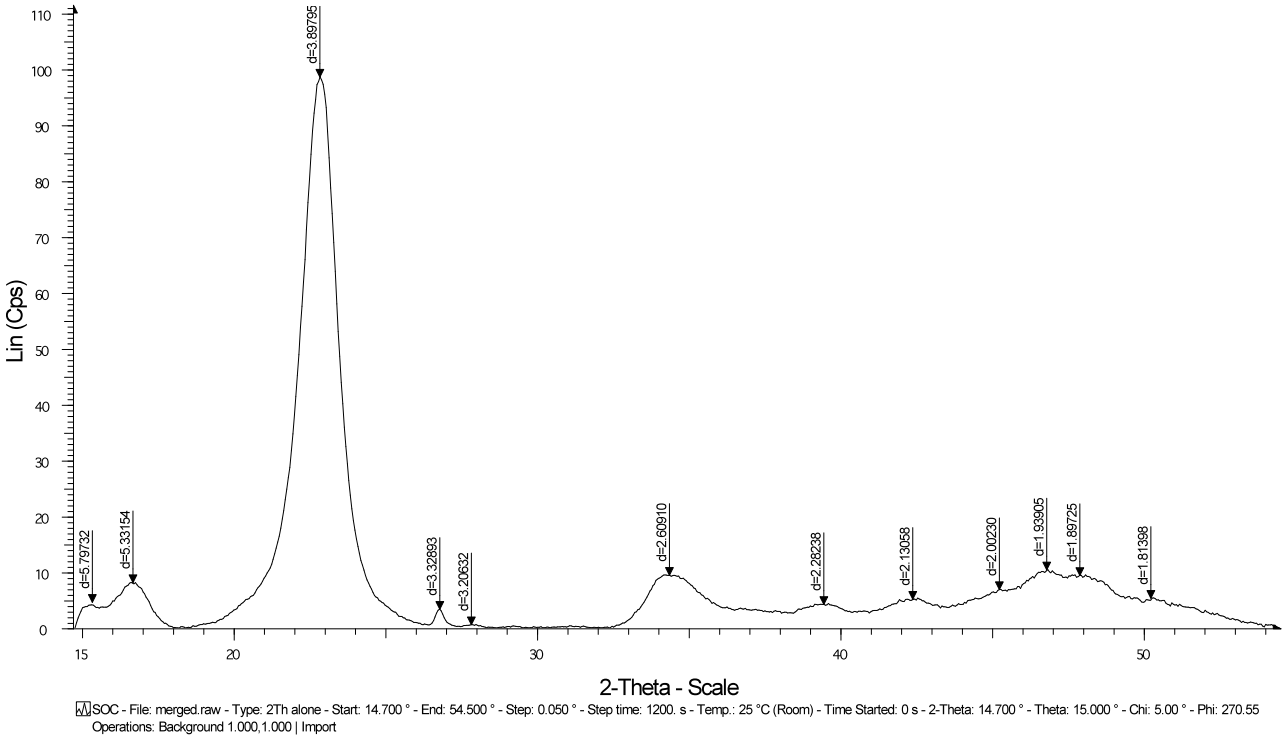

3.3.2 Oxygen isotope record, construction of age model

Variations in oxygen isotope ratios through time are preserved in calcareous marine organisms. This variation is primarily the result of changes in the volume of continental ice sheets (Shackleton & Opdyke, 1973). Bulk carbonate oxygen isotope data were obtained throughout both trigger and piston cores at 5cm resolution (see Appendix 1 Table A1.7) and are presented in Figure 3.3.3

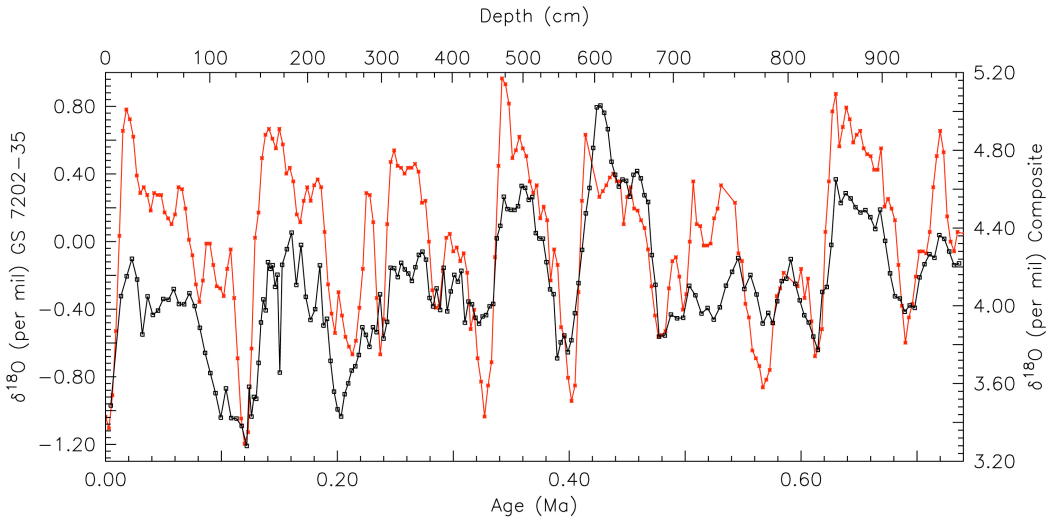

Figure 3.3.3: $\delta^{18}O$ values for GS 7202-35 (blue line) and a composite record of cores V1930 and ODP 677 (red line) used to establish time series

An age model for the sediment accumulation was constructed by correlation of the bulk sediment $\delta^{18}O$ record with a composite time series obtained from core V1930 and ODP 677 (available at http://delphi.esc.cam.ac.uk; (Shackleton et al., 1990; Shackleton & Pisias, 1985) using the Analyseries software (Palliard et al., 1996). The time series was obtained by visually matching the isotope record from core GS 7202-35 - 5 to the composite record. The data was tied at 9 depth/time points.

Table 3.3.1 shows the tie points used in the correlation. A linear sedimentation rate was assumed between consecutive tie points.

Table 3.3.1: Tie points used in correlation of sediment d^{18}O data to composite records in construction of age model

adj Depth (cm)	Age (Ma)
21.41	0.02
134.52	0.12
213.03	0.18
472.58	0.34
578.00	0.41
688.88	0.48
776.36	0.57
853.02	0.63
973.00	0.73

Table 3.3.2: Model derived ages of the sediment horizons in core GS 7202-35 at which *Emiliania Huxleyi* appears and *Pseudoemiliania Huxleyi* becomes extinct and corresponding literature values (Thierstein et al., 1977)

Depth in piston core	Biostratigraphy (Bostrom et al., 1974)	Depth adjusted to include trigger core depth	Age from model	Literature age
0-200cm	Abundant *Emiliania Huxleyi*	138-338cm	124-261ka	*EHux* arrival ~278kaBP
200-490cm	No *E. Huxleyi*, no *Pseudoemilinia Lacunosa*	343-628cm	264-440ka	*P. Hux* extinction
500-850cm	*P. Lacunosa present*	628-983cm	440-740.5ka	MIS 12 ~458kaBP

The depth horizons of certain biostratigraphical markers were used to check the age model (The arrival of *Emiliania Huxleyi* at ~278 ka BP and the extinction of *Pseudoemiliania Lacunosa* in isotope stage 12, ~458ka BP, (Thierstein et al., 1977). The ages of these depth horizons generated by the age model are consistent with literature values. (Table 3.3.2)

An unknown depth of sediment was missing from the top of the piston core; therefore there was potential for overlap between the piston core and the trigger core. The extent of this overlap is established in Chapter 2.4

3.3.3 Geochemistry

Bulk geochemical analysis was carried out using X-Ray Fluorescence, because this technique allowed a direct and complete survey of the core without need for chemical digestion of the samples. ICP-AES and ICP-MS measurements were made for comparison and to enable direct comparison to sequential leaches carried out on the samples and with previously published data from 14^{o}S.

The trigger and piston core were both analysed by XRF Beads for major elements (Al, Ti, Si, Fe, Mn, Mg, Ca, P, Na) and pellet for minor elements (As, Ba, Br, Cl, Cr, Cu, Mo, Ni, Sr, U, V, Zn). The results are presented in Appendix 1 Table A1.1. Data comparison between the ICP-AES data and the XRF data indicated a systematic offset in most elements as measured by XRF, thus all data presented are ICP-AES-corrected XRF values (Table A2.3) or ICP-AES values (Table A1.2). The data correction is discussed in Appendix 2. Total bulk digests and solutions from two sequential extraction schemes of selected samples were analysed by ICP-AES (Ca, Ti, Al, Mg, Fe, Mn, Co, Ni, Cu, Zn, V, P, As). A comparison of the data quality of the ICP-AES vs. the XRF is located in Appendix 2.

3.4 Sediment accumulation rates

3.4.1 Estimation of Linear sedimentation rate

Linear sedimentation rates were inferred from the age model in this core and are between 0.95– 2 cm/ka (see Table 3.4.1). The age model is unable to resolve the first ~4.5ka BP, due to either absence of sediment from the core top, or mixing of the surface sediments due to bioturbation.

Table 3.4.1 GS 7202-35 linear sedimentation rate inferred from $\delta^{18}O$ age model

Depth Range (cm)	Sedimentation rate (cm/ka)
5.25 – 130.5	1.11
138 – 208	1.23
213 - 468	1.64
473 - 578	1.63
583 – 693	1.58
698 – 778	0.95
783 – 853	1.23
8.58 – 983	1.18

These sedimentation rates are typical for the EPR and are consistent with other similar sediments (Table 3.4.2) (e.g. Dunk, 2004; Oxburgh, 1998; Schaller et al., 2000; Shimmield & Price, 1988).

Table 3.4.2: Linear sedimentation rates for cores at selected locations in the SEPR region

Core	Location	Linear Sedimentation rate (cm/ka)
EXC0 12 (Dunk, 2004))	14°16.48'S, 112°19.4W	1.72
V19-54 (Oxburgh et al., 1998)	17°02'S, 113°54'W	0.75-1.5
Y-71-7-53P (Schaller et al., 2000)	10°53'S, 110°44'W	1.3
TGT-154-18 (Shimmield & Price, 1989)	20°01.9'S, 113°51.4W	0.4

3.4.2 Mass accumulation rates

Assuming age model sedimentation rates and a dry bulk density of 0.59 g/cm^3 (Rydell et al., 1974) gives a range of bulk sediment accumulation rates of 559.2 – 967.0 mg/cm/ka (See Table 3.4.3).

Table 3.4.3: GS-7202-35 Bulk sediment accumulation rates, derived from linear sedimentation rates assuming a dry bulk density of 0.59 g/cm^3

Depth Range	Age Range	Bulk Sediment accumulation	
Cm	ka	cm/ka	mg/cm/ka
5.25 - 130.5	4.5 - 117.5	1.11	654
138 – 208	123.9 - 180.9	1.23	725
213 – 468	184.9 - 340.5	1.64	967
473 - 578	343.6 - 408	1.63	962
583 – 693	411.2 - 482.5	1.58	933
698 – 778	487.7 - 571.7	0.95	559
783 – 853	575.6 - 630.0	1.23	759
858 – 983	634.2 - 740.5	1.18	694

These data are in good agreement with the EXCO sediments (14^{o}16'S, 112^{o}19'W), which show an average linear sedimentation rate of 1.5cm/ka and bulk accumulation rate of 825 mg/cm/ka (Dunk, 2004; Hauschild et al, 2003). They are also consistent with the rise crest sediments from 5 – 31^{o}S presented by Dymond (1981) which have an average bulk sediment accumulation rate of 661 mg/cm/ka.

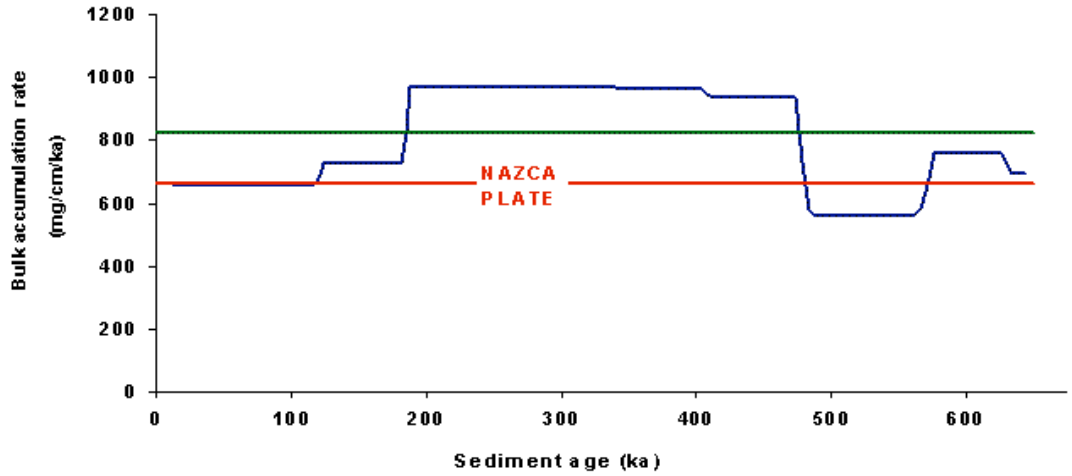

Figure 3.4.1: Bulk sediment accumulation rate (blue line) compared to average bulk values for Nazca plate (Dymond, 1981; red line) and the EXCO sediments (Dunk, 2004; green line)

3.5 ^{230}Th-normalised sediment accumulation rates

The problem with calculating mass accumulation rates using the linear sedimentation rate between dated horizons is that the temporal resolution is poor, the dry bulk density is generally uncertain and there is no distinction between vertical and lateral sediment fluxes (Francois et al., 2004)

Lateral transport of sediments in the SEPR is potentially significant and its occurrence is hard to identify, especially if occurring at the same time as original deposition. The $^{230}Th_{xs}^{0}$ content of seafloor sediments can be used as a flux gauge to estimate preserved vertical rain rates of different sedimentary components (Francois et al., 2004). This method assumes that the measured sedimentary inventory is equal to the known water column ^{230}Th production rate. If scavenging of ^{230}Th is less than 100% efficient, or if there is significant down-slope transport of ^{230}Th depleted material which dilutes the $^{230}Th_{xs}^{0}$ value, then the flux gauge will overestimate the preserved vertical rain rate Thus the values obtained using this method are upper limits of the preserved vertical rain rate in this setting.

Uranium and Th activity and age-corrected unsupported ^{230}Th values are presented in Table 3.5.1. Variation in ^{230}Th/^{234}U ratio through time is presented in Figure 3.5.1. Data were measured by α-spectrometry. All α-spectrometry data carry the caveat that the chemical separation was not effective; either due to incomplete cleaning of the column, or overloading, and therefore all the Th and U isotope data carries a high level of uncertainty. Nevertheless, the ^{230}Th values are consistent with the previous analysis by Rydell et al., (1974).

The degree of sediment focusing (the focusing factor, Ψ) can be calculated from the activity of scavenged ^{230}Th ($^{230}Thxs_0$). If the flux of scavenged ^{230}Th is equal to its rate of production in the water column, and there is no syn-depositional transport of sediment, then the inventory of scavenged Th between two given depth horizons should equal the production ($^{230}Th_{prod}$) integrated over the time of accumulation of the depth range (Equation 3.5.1)

$$\int^{230}Th_{xs} \,.\, \rho \,.\, dz = \int^{230}Th_{prod}\, dt \qquad \text{Equation 3.5.1}$$

where:

ρ is the in-situ bulk density, calculated using the $CaCO_3$ content for the Pacific Ocean (~72%) and the age model derived linear sedimentation rates (1.11 cm/ka).

dz = depth interval

dt = time taken for sediment in depth interval to accumulate

Therefore:

$$\Psi = \int(^{230}Th_{xs} \,.\, \rho \,.\, dz / (\int^{230}Th_{prod}\,(t_2\text{-}t_1) \qquad \text{Equation 3.5.2}$$

An important caveat to the data is that the model of ^{230}Th scavenging and production might not hold true in this setting, as the hydrothermal plume is a significant source of particles that are laterally advected at a depth of only 100-200m above the sediment (as opposed to a water column depth of 3044m)

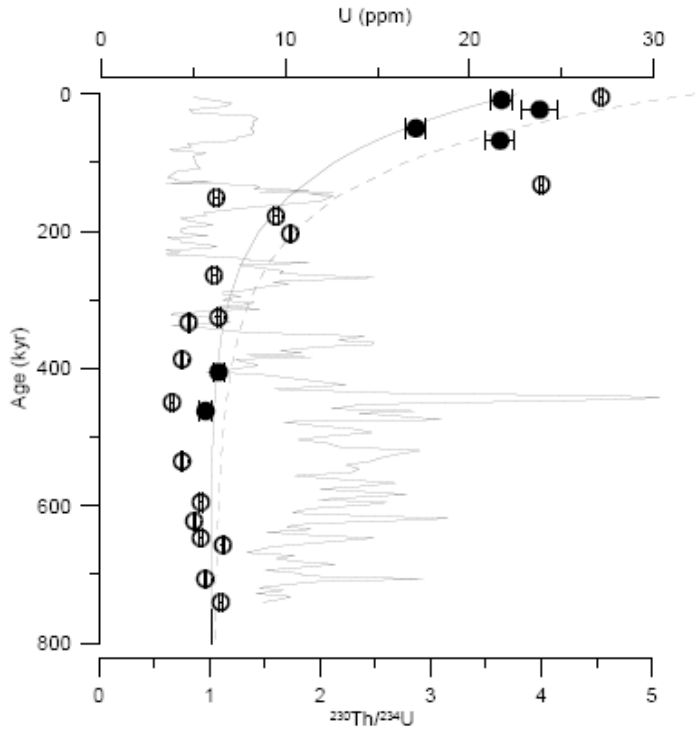

Figure 3.5.1: Downcore $^{230}Th/^{234}U$ ratio. The solid line indicates the bulk U concentration in the sediment in ppm. Closed circles are $^{230}Th/^{234}U$ ratios for GS7202-35 taken from Rydell et al., 1974. Open circles are $^{230}Th/^{234}U$ as measured by alpha spectrometry.

The calculated focussing factors (Table 3.5.1) suggest that there is a significant amount of focussing occurring. The focussing appears relatively constant over the last ~50 ka, but seems to have been higher at ~75 ka BP.

A recent study of several cores from the eastern equatorial Pacific (Kienast et al., 2007) applying ^{230}Th normalisation found a coherent regional pattern in the bulk sedimentation and organic carbon fluxes through the Holocene that was consistent with the current oceanographic conditions. This finding was in direct contrast with estimates of sedimentation using mass accumulation rates calculated using core chronologies, which are higher with greater variability between sites. Focussing factors calculated for these sediments imply significant lateral transport of sediment in the EEP and a compilation of core records suggests that it is highly variable, both spatially and temporally.

Table 3.5.1: Uranium and Thorium isotopes measured by alpha spectroscopy and the sediment flux and focussing factors calculated according to Equations 3.5.1 and 3.5.2

Sample ID	Depth	Age	^{232}Th	±	^{230}Th	±	^{238U}	±	^{235}U	±	^{234}U	±	$^{230}Th_{xs}{}^{0}$	±	Flux	±	Focussing
	cmbsf	Ka	dpm/g		dpm/g		dpm/g		dpm/g		dpm/g		Dpm/g		$g/cm^2/ka$		Factor
TC2	10	9	0.31	0.05	14.73	0.85	3.36	0.34	0.48	0.10	4.05	0.39	15.47	0.92	0.52	0.03	1.33
TC3	15	13	0.52	0.11	15.79	1.41							17.60	1.60	0.45	0.04	1.51
TC5	26	23	0.07	0.04	12.76	1.04	2.96	0.21	0.38	0.06	3.20	0.23	14.92	1.29	0.54	0.05	1.28
TC7	36	32	0.07	0.02	13.84	0.70							18.53	0.94	0.43	0.02	1.59
TC11	56	50	0.04	0.03	14.01	0.91	5.65	0.55	1.89	0.25	4.89	0.49	18.45	1.48	0.43	0.03	1.58
TC15	76	68	0.07	0.03	16.91	1.25	3.90	1.37	1.46	0.77	4.66	1.58	27.76	2.69	0.29	0.03	2.38
TC18	91	81	0.05	0.05	13.22	1.34							27.98	2.83	0.29	0.03	3.23
PC88	573	405			3.21	0.29	3.07	0.29	0.18	0.06	2.97	0.28	1.49	17.41			
PC94	603	424					7.77	0.54	1.41	0.15	6.53	0.47	Nd		nd		nd
PC98	623	436					11.22	1.50	0.38	0.15	11.63	1.55	nd		nd		nd
PC103	648	452	0.06	0.05	12.59	1.17	3.32	1.12					nd		nd		nd
PC106	663	462			9.20	1.00	9.92	1.11	0.53	0.14	9.54	1.07	nd		nd		nd
PC109	678	471					11.50	0.65	1.21	0.12	9.83	0.57	nd		nd		nd

nd=not determined

3.6 Bulk sediment composition

The major sedimentary sources to this region of the SEPR have been previously identified as a three-component mixture comprising a minor detrital input, a biogenic input (primarily calcareous ooze), and a significant hydrothermal input (e.g. Dymond, 1981; Dunk 2004). Visual inspection, XRD and SEM of GS 7202-35 show a majority of calcitic nanofossils and foraminiferal ooze, with a significant amorphous Fe-Mn (hydr)oxide component.

3.6.1 Carbonate input

$CaCO_3$ was calculated using ICP-AES Ca data (Equation 3.6.1). It is assumed there is negligible detrital Ca input to the sediment on the basis analysis of XRD and SEM, both of which indicated the presence of little crystalline material other than calcite and a negligible quantity of halite precipitated from porewater salts) (See Appendix 3 for explanation of data correction).

$$CaCO_3 = Ca_{ICP\text{-}AES} * (100.08/40.08) \qquad \text{Equation 3.6.1.}$$

Where (100.08/40.08) is the ratio of the relative molecular mass of $CaCO_3$ to that of Ca and $Ca_{ICP\text{-}AES}$ is the concentration of Ca measured via ICP-AES

$CaCO_3$ was also calculated from inorganic carbon measured via coulometry for purposes of comparison (Equation 3.6.2).

$$CaCO_3 = C_{COUL} * (100.08/12.011) \qquad \text{Equation 3.6.2}$$

Where C_{COUL} is the concentration of inorganic carbon measured via coulometry and (100.08/12.011) is the ratio of the relative molecular mass of $CaCO_3$ to that of carbon.

Both methods yield carbonate content between 55-80% wt% (Figure 3.6.1) for the core with a general trend of decreasing carbonate with increasing age.

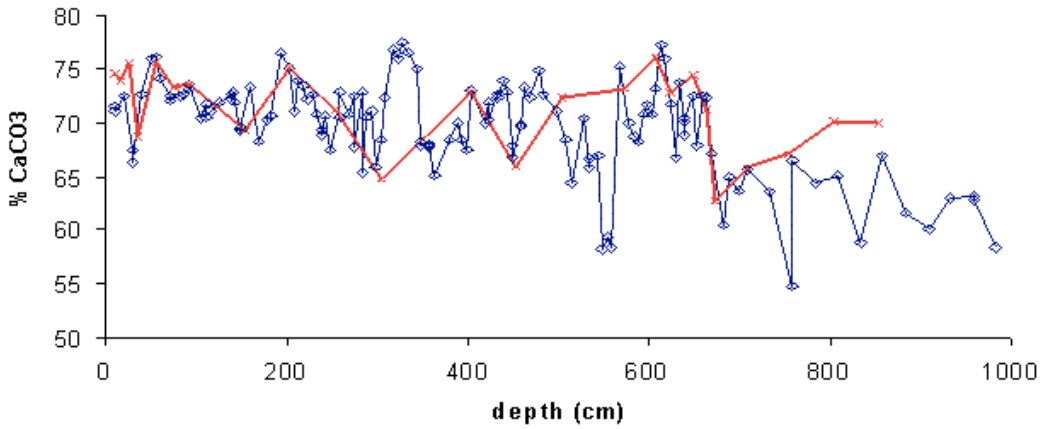

Figure 3.6.1 % calcium carbonate in core calculated from a) Ca^{2+} concentrations measured by XRF with ICP-AES correction applied (red line) and b) Inorganic carbon measured using coulometry (blue line)

In general the agreement between the corrected XRF data and the coulometry data is good (Figure 3.6.1), supporting the assumption that most of the Ca present in the core is bound in a carbonate phase.

Scanning Electron Microscopy showed no evidence of any non-calcite crystalline material. Samples with high XRF Ca were subjected to a sequential leach protocol to remove calcite and iron and manganese hydroxides, leaving a minor residue. However XRD analysis of the residue indicated only the presence of a small amount of an unidentified clay mineral (resembling illite).

Sequential extraction data on the EXCO sediments east of the axis demonstrate 98-99% of the total Ca is removed in the carbonate fraction (Dunk 2004). Sequential extraction data for core GS 7202-35 indicate a significant percentage of calcium still remaining in the reducible oxide phase, suggesting the presence of a non-carbonate calcium-bearing phase.

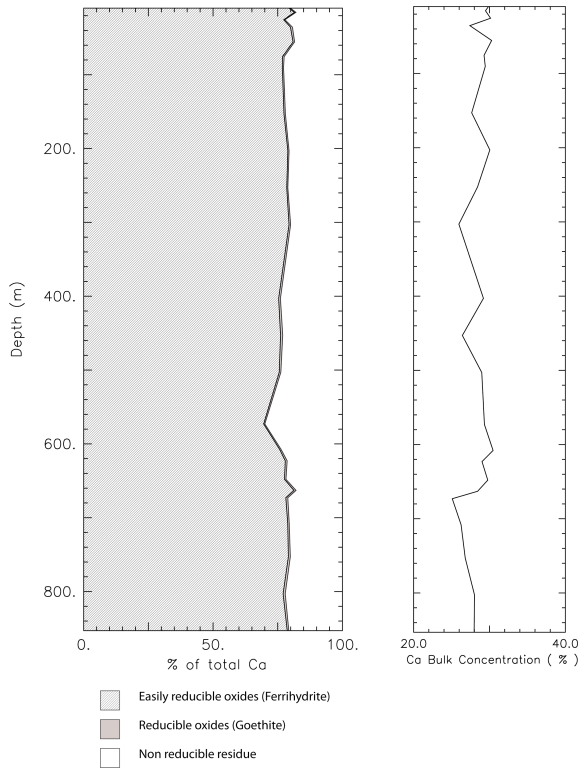

Figure 3.6.2: Downcore bulk Ca concentration (wt%) and partitioning of Ca between phases according to sequential leach data. Sequential leach data is presented as % of the bulk concentration in each phase.

Both the SEM images and XRD data show no evidence of any crystalline or detrital phases, which would indicate the absence of non carbonate Ca bearing species. As mentioned previously, calculations using the ICP-AES and coulometry data are consistent with all the Ca being calcium carbonate. A possible explanation is a Ca-bearing carbonate phase present that is not as susceptible to dissolution as pure calcite. A further possibility for this conflict is a matrix effect in the analysis of the sequential extraction solutions suppressing the calcium measurements. Further analysis of the sequential extraction solutions is required using standards that are better matched to the sample matrix is required to help resolve this conflict.

3.6.2 Hydrothermal Input

Hydrothermal plume fallout in the far-field is dominated by Fe and Mn (oxy)hydroxides. Fe and Mn should therefore make effective tracers of the hydrothermal fraction of the sediments. Down core profiles are shown in figure 3.6.3

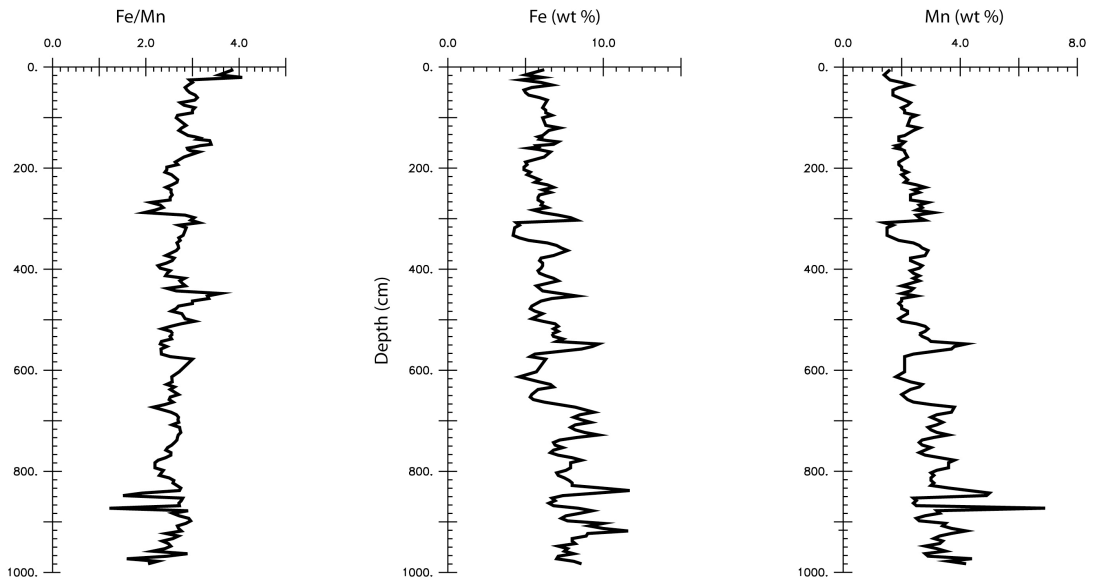

Figure 3.6.3: a) Down-core distribution of Fe, Mn and Fe/Mn against depth

Dymond (1981) and Ruhlin & Owen (1986) have suggested there is no evidence for variation in Fe/Mn along the SEPR, either in space or time. These sediments show an general decrease in Fe/Mn with increasing depth in the core (i.e. in sediment of increasing age and that was deposited when the core was closer to the ridge axis.)

.

3.6.3 Detrital input

It is typical to use either Ti or Al concentrations to calculate the detrital contribution to the sediment, making the assumption that all the Al and Ti are of lithogenic origin. Earlier studies of the region (e.g. Dymond, 1981) have used this method. However it has been

suggested that Al is an unsuitable tracer for detrital inputs in areas where it is very low, such as the equatorial Pacific (Murray et al., 1997; Murray & Leinen 1996; Dymond, 1997) as a significant fraction is scavenged from seawater. Sequential extraction work on sediments from the EXCO site supports this assumption at 14^{o}S east of the ridge axis (Dunk, 2004), suggesting Ti would be a more suitable detrital tracer. Figure 3.6.5 shows the partitioning of Al between the easily reducible, reducible residual phases. It can clearly been seen from this data that the Al is not limited to the detrital phase as there is a significant percentage associated with other phases.

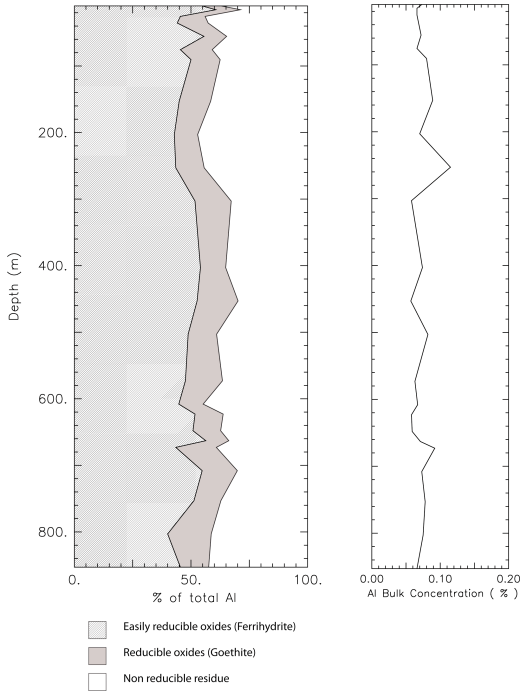

Figure 3.6.5: Bulk Al concentration (wt%) and partitioning of Al between phases according to sequential leach data (as % of bulk concentration)

In these sediments the Al concentration is below the detection limit of the XRF. ICP-AES data indicate detrital correction to the data is unnecessary, as it is significantly less than the precision of the bulk element concentration measurement (Appendix 3)

3.7 Oxyanion behaviour in the sediments: Mo and U

In addition to Fe and Mn, hydrothermal sediments are highly enriched with a number of oxyanions whose distribution is sensitive to the redox status of the sediment (e.g. Mo, U). The distribution of these elements can be used to investigate the variations in the redox status of the sediments through time. Molybdenum behaves conservatively in oxic seawater. It also becomes enriched in anoxic sediments (Bertine et al., 1972; Francois, 1988) as Mo (VI) is reduced to insoluble Mo (VI) (e.g. Bertine, 1972; Calvert & Pedersen, 1993). Seawater MoO_4^{2-} is has been found to preferentially adsorb to MnO_2 (Shimmield & Price, 1986). The Mo/Mn ratio in oxic sediments is relatively constant at 0.002, but it has been previously shown that Mo is remobilised during suboxic diagenesis (Shimmield & Price, 1986)

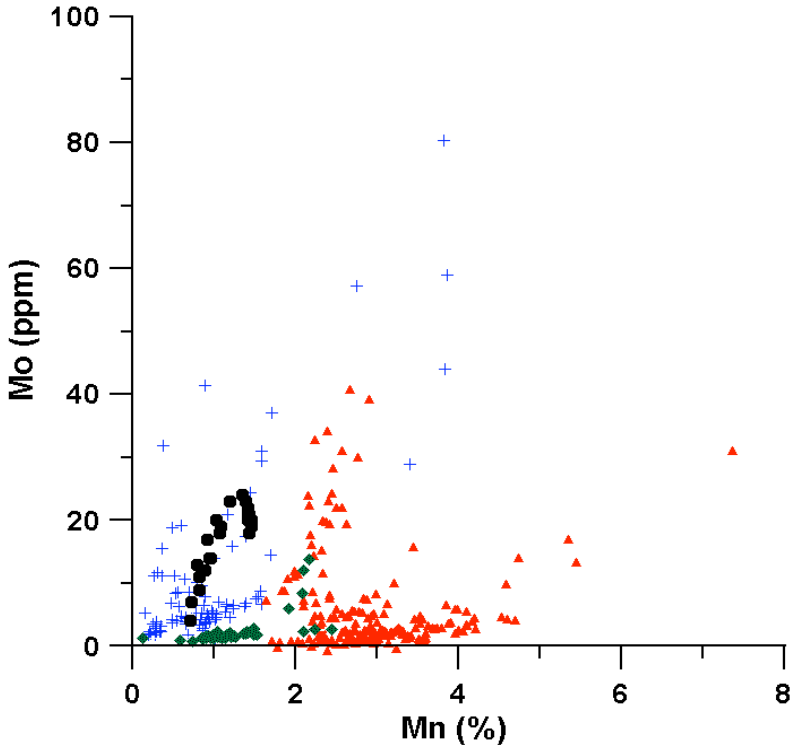

Figure 3.7.1 Mo vs. Mn content from EPR sediments from 14°S (Red triangles; Core GS 7202-35, this work, blue crosses; EXCO, Dunk 2004, Black circles; 20°S oxic sediment, Shimmield & Price, 1988, Green diamonds; 10°S, Schaller et al., 2000.)

Suboxic diagenesis and Mn cycling lead to Mo remobilisation below the redox front. Mo forms strong associations with sulphide species under reducing conditions so low Mo/Mn ratios are indicative of Mn cycling in the absence of S cycling. Under suboxic conditions in the SEPR high Mo/Mn ratios indicate more oxic sediments and lower Mo/Mn ratios more reducing conditions. This core exhibits two distinct types of behaviour. The upper core shows higher Mo/Mn values. Below ~1.4m, the ratio is consistently lower, indicating that conditions have been reducing. (Figure 3.71)

In a hydrothermal setting U is scavenged from seawater via a co-precipitation mechanism with Fe oxyhydroxides (Mills & Elderfield, 1995). The U/Fe ratio of EPR in these sediments is much higher than those in similar hydrothermal sediments from the Atlantic. This may reflect a higher U/Fe ratio in the plume in the Pacific. Sediment trap data from the EPR (German et al., 2002) contain a large amount of sulphate material, while plume particles from the TAG MAR site contain predominantly oxides (German et al., 1991) – the U/Fe ratio of these different particle populations are very different.

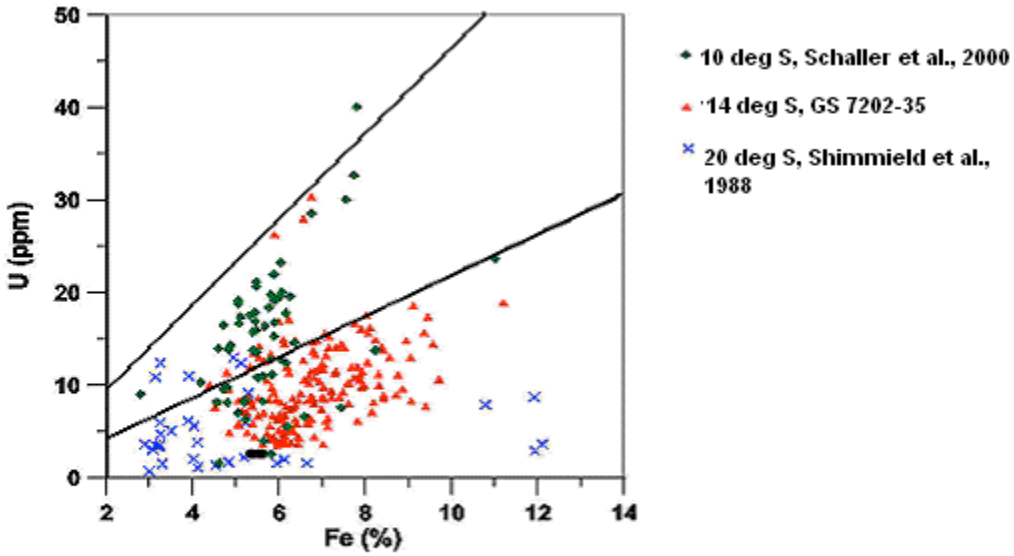

Figure 3.7.2 U vs. Fe content in EPR sediments from 14°S (Core GS 7202-35, this work), 10°S (suboxic; Schaller et al., 2000) and 20°S (fully oxic; Shimmield & Price, 1988) Black lines indicate the range of values observed in EPR plume particles from (German et al., 2002)

Sediments at 10°S are suboxic below ~3-4cm depth (Schaller et al., 2000). There is evidence that the U/Fe ratio reflects the high sulphide input from the plume at this latitude. Over time the sulphides are oxidised within the sediment column but release of U is limited by pervasive suboxic diagenesis throughout the core.

At 14°S comparison of sediment U/Fe to the plume particle ratio indicates some release of U, decreasing the U/Fe ratio (Figures 3.7.2; 3.7.3a). Uranium behaviour in these sediments and the symmetrical shape of peaks in the profile are not consistent with a classic burn down mechanism of U enrichment, instead suggesting a deepening then shallowing of the redox front during the glacial periods.

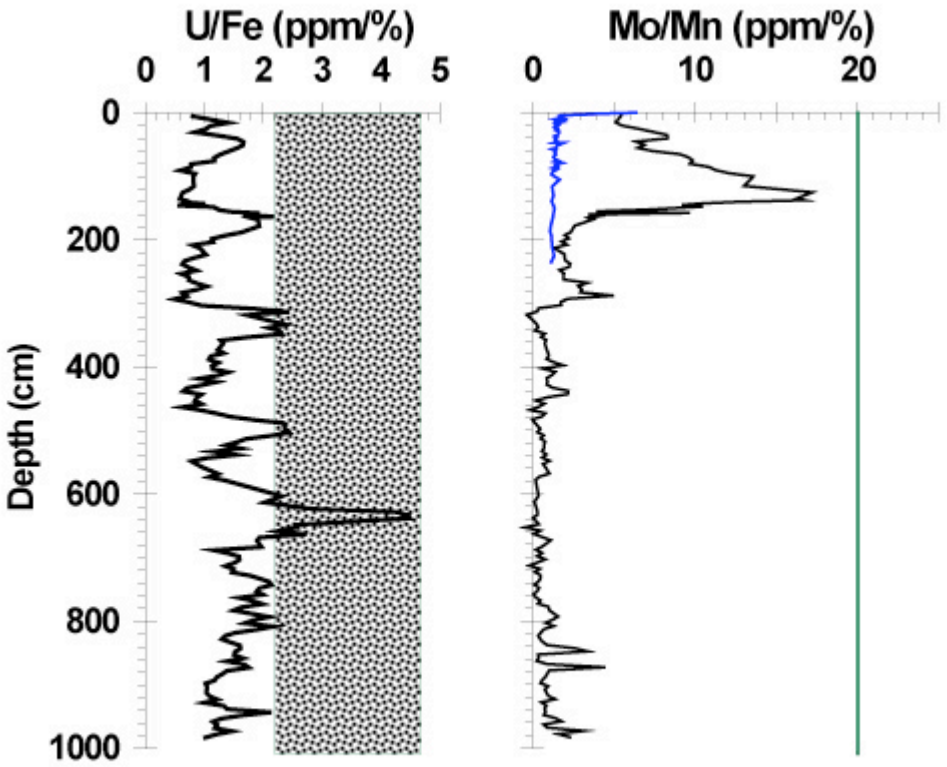

Figure 3.7.3: (a) U/Fe distribution with depth. The hatched area indicates the hydrothermal plume ratio (German et al., 2002) (b) Mo/Mn distribution with depth at 10°S (blue line; Schaller et al., 2000) and 14.5°S (black line; GS 7202-35). The green line indicates the ratio in fully oxic sediments at 20°S (Shimmield & Price, 1986)

There is a latitudinal gradient in the redox status of the sediments along the SEPR from extremely suboxic at 10°S (Schaller et al., 2000) to fully oxic at 20°S (Shimmield & Price 1988), in line with decreasing productivity (and thus export) moving southwards of the equator.

The U/Fe and Mo/Mn ratios in the sediments record this gradient in redox status. Sediments collected from the western ridge flank at 10°S (Schaller et al., 2000) become suboxic within centimetres of the sediment water interface. The Mo/Mn profile reflects this with high Mo/Mn at the core top, reducing to values consistent with pelagic clays at ~5cmbsf (Figure 3.7.3b), while at 14°S the redox boundary is much deeper in the sediment. U/Fe ratios shift from near-plume values at 10°S where suboxic conditions prevent release of U, decreasing in the increasingly oxic sediments further south where U can be released from the sediments (Figure 3.7.2).

While data available from 17°S was limited (Bender et al., 1971; Oxburgh, 1998) it appears that this core behaves intermediately between the fully oxygenated behaviour observed at 20°S (similar to TAG) and the behaviour at 14°S, i.e. there is some diagenesis occurring at this site. Sediments at 17°S (Bender et al., 1971) have a similar accumulation rate to that of this core of ~1.5 cm/ka (assuming Oxburgh 1998 age model).

General circulation models are now routinely used for estimating carbon fluxes through the ocean system (e.g. Popova et al., 2006). Carbon export over the EPR was modelled using an OCCAM 1° model extended to include biogeochemical cycles (Ochllies et al., 2001; Marsh et al., 2005). Modelled export over the EPR is ~5x greater at 10°S than at 14°S (K Popova, A Yool, pers. Comm; Figure 3.7.4). Further work is required to refine this initial modelling. This is consistent with observational estimates (e.g. Antoine et al., 1996)

There is also a gradient in redox status from east to west across the ridge axis at 14-15°S. The EXCO study carried out by the University of Hamburg and University of Bremen (2000, Cruise SO-145/2 of the RV Sonne) collected a number of cores in a transect along

the eastern flank of the EPR at ~14°S. These sediments appear fully oxic (Dunk, 2004). However, on the western flank at similar latitude the sediments show evidence of significant suboxic diagenesis.

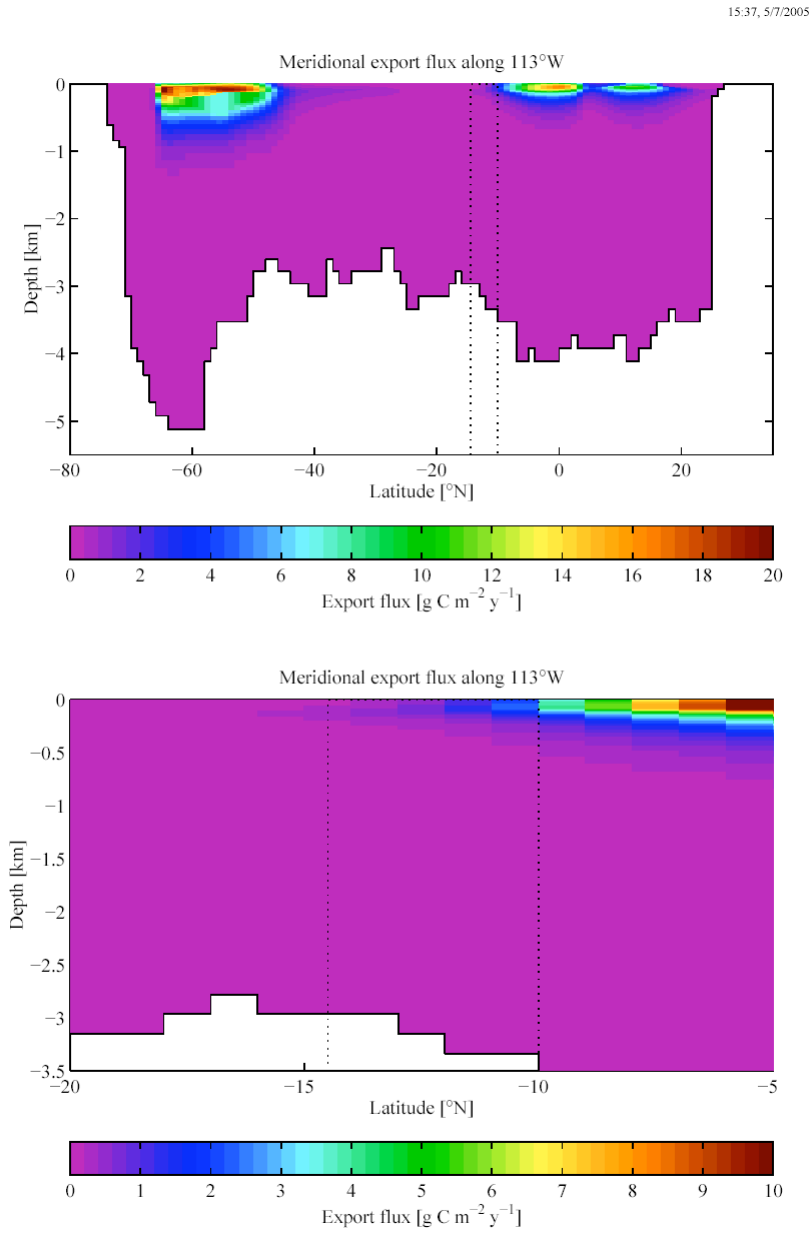

Figure 3.7.4: Meridional export flux along 113°W modelled using OCCAM 1° ocean general circulation model extended to include biogeochemical cycles (Marsh et al., 2005, Sinha & Yool, 2006). Dashed lines indicate locations of cores at 10°S and 14°S.

There is also a gradient in redox status from east to west across the ridge axis at 14-15^{o}S. The EXCO study carried out by the University of Hamburg and University of Bremen (2000, Cruise SO-145/2 of the RV Sonne) collected a number of cores in a transect along the eastern flank of the EPR at ~14^{o}S. These sediments appear fully oxic (Dunk, 2004). However, on the western flank at similar latitude the sediments show evidence of significant suboxic diagenesis.

3.7 Summary

This chapter aimed to establish the bulk sediment composition of core GS-7202-35 and compare this with regional sedimentation trends.

The eastern tropical Pacific is the locus of high sediment accumulation. Seismic reflection studies indicate there is little lateral sediment transport on crust <2Ma at 15^{o}S. However calculation of the degree of focussing using ^{230}Th normalisation techniques suggests that there has been significant focussing in this area. The focussing factor for the last 50 ka is relatively constant at 1.3-1.6, while the focussing seems to be almost twice as great at before 75ka BP.

An age model was constructed from $\delta^{18}O$ and used to infer linear sedimentation rates of 0.95-1.64 cm/ka. This is consistent with other sedimentation in the region. Bulk mass accumulation rates range from 654 – 967 mg/cm/ka. Again this is consistent with the accumulation found at the EXCO sites and with values from analysis of sedimentation across the Nazca plate.

The sediment in core GS 7202-35 can be represented by a simple two-component model of calcium carbonate diluted with a large metalliferous hydrothermal input. The detrital input is negligible and correction of data for detrital content is unnecessary, as the Al and Ti data from the core indicate any correction would be smaller than the error associated with the analytical techniques.

The water column at site GS 7202-35 is saturated at depth with respect to calcite ($\Omega_{CALCITE}$ = 1.03). The bulk of the sediment is calcium carbonate (calcite; 60-80%). The XRD, SEM and coulometric data all indicate that the Ca is bound to carbonate phases.

The calcite in the core is diluted by a large hydrothermal input. Fe and Mn make effective tracers of hydrothermal input to the sediment from the plume. Seawater Mo and U are also scavenged by hydrothermally precipitated Fe and Mn (hydr)oxides. In GS 7202-35 Uranium is greatly enriched, although U/Fe ratios indicate there has been some release of U with respect to the hydrothermal plume. The enrichment peaks do not have the

distinctive shape associated with a classical burn down mechanism, instead suggesting a shift in the depth of the redox front through time. U/Fe and Mo/Mn ratios in the sediment record a latitudinal gradient in redox status from extremely suboxic at 10^{o}S (Schaller et al., 2000) to fully oxic at 20^{o}S (Shimmield & Price, 1988) which is in line with the trend of decreasing productivity (and thus export) moving south of the equator along the East Pacific Rise.

Chapter 4: Controls and mechanisms of trace metal and oxyanion diagenesis

4.1 Chapter Aims

Significant enrichments in trace elements are observed in the sediments to the west of the ridge axis at 14°S on the SEPR, which are attributed to axial hydrothermal input. These sediments are suboxic in nature i.e. hydrothermal sediments are known to be major sinks for certain elements from seawater but the ultimate fate of metals in these sediments depends on post depositional reactions occurring after burial. The focus of this chapter is the investigation of the mechanisms controlling the distribution and fate of these elements in a ridge flank setting. Specifically this chapter aims to:

(a) Identify the speciation of the Fe and Mn content within different operationally defined sedimentary phases and investigate the likely pathway of alteration post burial.
(b) To identify the associations of the trace metals Cu^{2+} and Zn^{2+} and the oxyanions of P, V, As, Mo and U and identify the controls on their distribution through the sediment.

4.2 Introduction

Hydrothermal vent fluids are enriched in dissolved Fe and Mn, which precipitate as ambient seawater is entrained into the rising buoyant plume, forming particulate oxides and sulphides. In the far-field the fallout is dominated by the (hydr)oxide phases, primarily ferrihydrite, $Fe(OH)_3$ (Campbell, 1991; Feely et al., 1994b). Mn also forms a distinct amorphous (hydr)oxide phase (Savenko, 2001). Fall-out from the hydrothermal plume forms the dominant source of Fe and trace elements to the sediment (Dymond (1981). Dissolved oxyanions in the seawater (e.g. As, U, P and V) are scavenged by the particulate Fe (and Mn), and have been observed to correlate linearly with Fe in particulate hydrothermal particles collected from the neutrally buoyant plumes from various ocean basins (Trefry & Metz, 1989; Feely et al., 1990a,b, 1994a, 1996; German et al., 1991; Metz & Trefry, 1993). Certain divalent trace metal cations (e.g. Ni, Cu, Zn) are also enriched in hydrothermal fluids with respect to seawater and co precipitate with Fe

(hydr)oxides (e.g. Ford et al., 1997, 1999; Martinez & McBride, 1998; Savenko, 2001). The trace metal-Fe relationship in hydrothermal plumes has been interpreted to be controlled by co-precipitation followed by particle removal via gravitational settling of heavier sulphide particles close to the hydrothermal source

The sediments underlying the hydrothermal plume are enriched in Fe oxide and sulphide phases and the trace elements that are scavenged by the hydrothermal particles (e.g. Dymond, 1981; Metz et al., 1988; Shimmield & Price, 1988; German et al., 1997) and therefore these sediments could record the plume values (German et al., 1997, Feely et al., 1998), unless post depositional processes alter the oxyanion/Fe ratios.

P/Fe ratios in both the Atlantic and Pacific have been found to vary consistently with inter-ocean variability of dissolved phosphate concentration (Feely et al., 1998). It has been suggested that the higher phosphate concentrations in the Pacific act to suppress the co-precipitation of V, reducing the V/Fe ratio in the plume particles and thereby the underlying sediments (Feely et al., 1994, 1998). Variations in As/Fe ratios have also been assigned to concentration differences in the deep ocean (Feely et al., 1996)

Sedimentary diagenesis acts to alter the oxyanion/Fe ratios from plume particulate values (e.g. Feely et al., 1998; Schaller et al., 2000). The redox status of the sediment has a significant affect on the oxyanion distribution, while the Fe and Mn phases are also diagenetically altered in both plume and sediment, with the metastable amorphous phases (e.g., ferrihydrite) being transformed to more crystalline forms (e.g. goethite) (Cornell et al., 1989; Schwertmann & Taylor, 1989)

Plume element/Fe ratios in the SEPR are well constrained (RIDGEFLUX; Feely et al., 1996, German et al., 2002) and an extensive study of the oxic sediments on the eastern ridge flank has been carried out (EXCO; Dunk, 2004). This study offers the opportunity to extend this to suboxic sediments at the same latitude and to place these results in the wider context of SE Pacific hydrothermalism and sediment geochemistry.

4.3 Results

ICP-AES corrected XRF data are presented in Appendix 2. The bulk sedimentary composition of the sediments has previously been discussed in Chapter 3. It has been shown that the sediments can be best represented by a simple 2 component mixing model, and that correction of the data for detrital content is not required because the local basalt input to this site is very low. All elemental ratios are presented on a wt/wt basis.

Results of a sequential leach carried out on selected samples are presented in Appendix 2 Table A2.4. The method used was developed from Poulton & Canfield (2005) and is discussed in Chapter 2.3.9. Sequential extractions were performed by Paula Sanchez and are reproduced here by kind permission.

4.4 Plume Derived Fe and Mn (hydr)oxides

Both amorphous Fe and Mn (hydr)oxides are subject to alteration with time, both as a hydrothermal plume ages, and after deposition in the underlying sediment. The dominant process of alteration is the transformation of the chemically unstable amorphous material (ferrihydrite) to more stable increasingly crystalline forms (goethite, haematite), through direct transformation (i.e. coagulation of colloidal aggregates, Halbach et al., 1981) and/or a process of dissolution and then recrystallisation from the dissolved pool Manganese oxyhydroxides (10Å Manganate in an aged, neutrally buoyant plume) are also likely to undergo dissolution and reprecipitation processes to form more stable crystalline forms from the fully hydrated form in the plume to fully dehydrated δMnO_2.

Plume Mn/Fe ratios in the Pacific show some variability with distance from source. Near field particles are dominated by Fe species. The plume Mn/Fe ratio increases with distance from vent site as the Mn(II) species in the plume are oxidised to Mn-oxyhydroxides during transit. In the neutrally buoyant plume further from the vent site the Mn/Fe ratio becomes relatively constant. The Mn/Fe supplied from the plume to the sediment west of the ridge axis is therefore inferred to be relatively constant.

In hydrothermal sediments post depositional variability of the Mn/Fe ratio is predominantly thought to be the result of fractionation occurring during early sediment diagenesis. This fractionation is caused by the differing reaction kinetics of Mn and Fe: the oxidation of Mn(II) to MnO_2 is kinetically slower than the oxidation of Fe(II) species to Fe(III). Aqueous Mn(II) species are also remobilised at a less negative Eh value than aqueous Fe(II) species.

Down core profiles of bulk Fe concentration and Mn/Fe ratio are shown in Figure 4.4.1a. Mn/Fe values range from 0.27 – 0.47 (Fe/Mn = 2.12-3.70). This range of values is relatively consistent with other sediments at 14°S east of the axis (EXCO: Mn/Fe = 0.21 - 0.33, Dunk 2004) 18°S (0.30 +/- 0.05; Marchig et al., 1986) and 20°S (0.32 +/- 0.03; Shimmield & Price, 1986), but there is more Mn present in the sediments relative to other sediments in the area (Figure 4.4.1b) with significantly more manganese present deeper in the core.

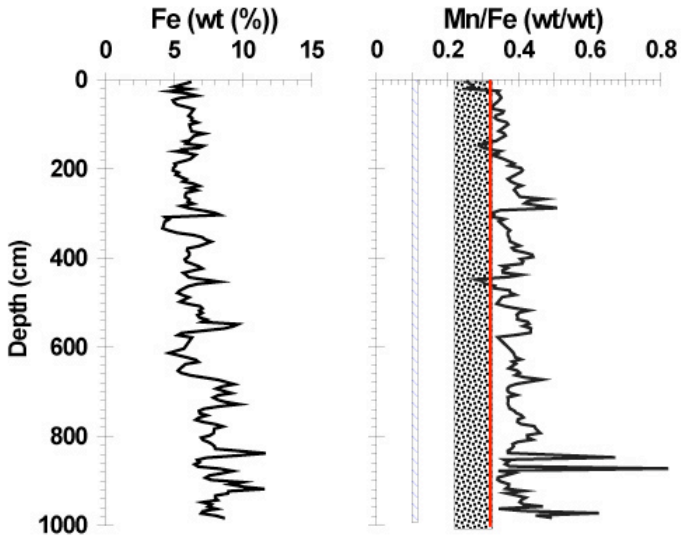

Figure 4.4.1a: Downcore bulk Fe content (wt %) and bulk Mn/Fe (wt/wt). The red line indicates the mean Mn/Fe ratio in fully oxic sediments (20°S; Shimmield & Price, 1986). The grey shaded area indicates the range of Mn/Fe found in other 14°S sediments (EXCO; Dunk, 2004). The hashed area indicates the ratio found in particulate matter below the non-buoyant EPR plume (Feely et al, 1996)

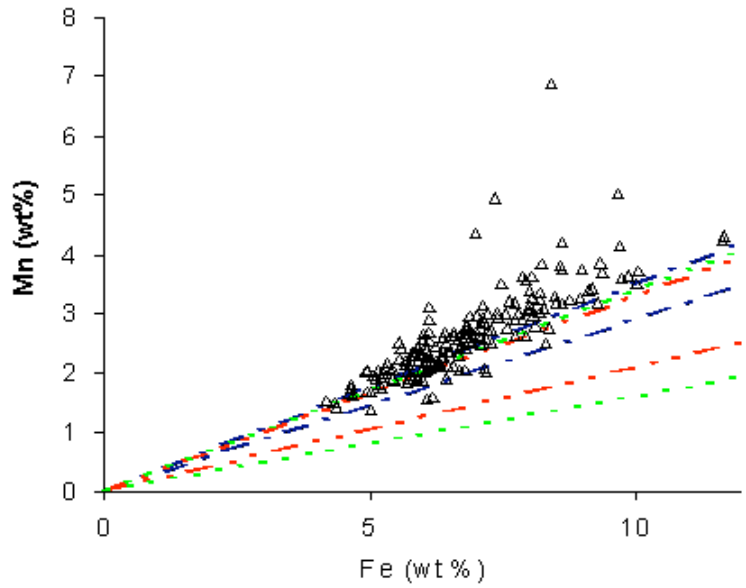

Figure 4.4.1b: Mn vs. Fe content of core GS 7202-35 (wt/wt). Dashed lines indicate the upper and lower ratios found in other EPR sediments (Green: 18oS, Marchig et al, 1986; Blue: 20oS, Shimmield & Price, 1988; Red: EXCO, 14oS, Dunk, 2004)

The significant variation in Mn/Fe ratio downcore implies that there has been either a variation in source Mn/Fe or post depositional reaction associated with suboxic conditions. The Mn/Fe ratio of hydrothermal sediments along the EPR has been previously treated as a relative constant (Dymond, 1981, Ruhlin & Owen, 1986) and the measured ratio in plume particles from this region is 0.1-0.12 (Feely et al., 1996). The excess Mn in these sediments must therefore be associated with post depositional uptake of Mn from seawater or from low temperature fluids circulating through the ridge flanks sediments. For MnO_2 precipitation to occur the sediments must be close to oxic in nature as Mn(II) is extremely mobile under suboxic conditions. There is very little organic matter present in the sediment (Figure 4.4.2) and no sulphides are detectable, meaning that there is a limited supply of electron donor to reduce the Mn present to Mn(II)aq and transport this via diffusion to the redox boundary.

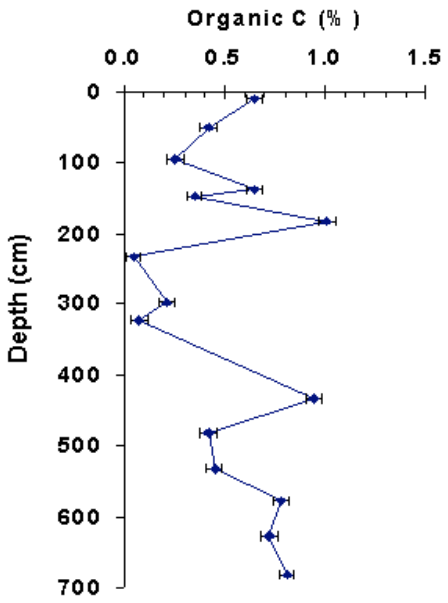

Figure 4.4.2: Down-core organic carbon distribution. Organic C is calculated as the difference between the total C and inorganic C as measured by coulometry

Dymond (1981) and Ruhlin & Owen (1986) have suggested there is no evidence for variation in Mn/Fe along the SEPR, either in space or time. However results from the EXCO transects across the ridge access at 14^{o}S (Dunk, 2004) have shown an increase in Mn/Fe with increasing distance from the ridge axis, which is explained in part by the differential oxidation kinetics of Fe^{2+} and Mn^{2+} as the plume disperses and in part by remobilisation of Fe and Mn during diagenetic processes.

These sediments show a general increase in Mn/Fe with increasing age of the core. The Fe and Mn fractionation with depth (and therefore increasing age) was examined using the sequential extraction data. The sediments were partitioned according to the following operationally defined pools: (a) easily reducible oxides (b) reducible oxides leaving a residual containing non reducible Fe phases (c) Residual phase. These data show that the bulk of both the Mn and the Fe are found in the easily reducible (i.e. amorphous) phase (60-70%). A small percentage of Fe is found in the more crystalline reducible fraction, increasing from 0 to ~4.3% with increasing depth. A significant proportion of both Fe and Mn in found in the non reducible residual phase (20-28% and 17.5-27% respectively) (Figure 4.4.3).

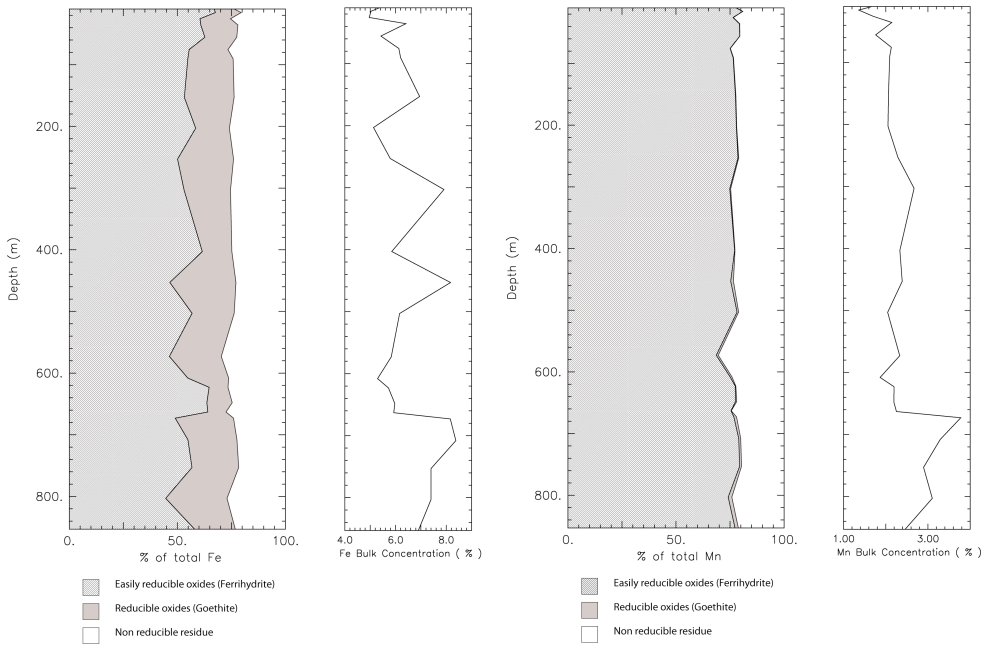

Figure 4.4.3: Fractionation of Fe and Mn and corresponding bulk element concentrations (wt%). The sequential leach separates the bulk concentration into fractions: Easily reducible oxides (hatched); Reducible oxides (grey) and the non reducible residue (white). Data is presented as % of the bulk concentration in each phase.

This partitioning implies a significant amount of the ferrihydrite has been transformed to more crystalline phases such as goethite. Ferrihydrite is chemically unstable under most environmental conditions. The time taken for ferrihydrite to transform to goethite can vary greatly, but it has been shown to be retarded by the co-precipitation of oxyanions and divalent trace metals (Zhao et al., 1994; Cornell & Schwertmann, 1996) and has also been shown to be stabilised by certain bacteria (Kennedy et al., 2004). Previous studies (Poulton & Canfield, 2006; Dunk, 2004) have approximated the overall ferrihydrite transformation as a first order process. The transformation process is represented using equation 4.1

$$-d(Fe_{Fer}/Fe_{tot})/dt = k(Fe_{Fer}/Fe_{tot})^{a} \qquad \text{Equation 4.1}$$

where Fe_{Fer} is the proportion of Fe in the ferrihydrite phase, Fe_{tot} is the total Fe, k is the rate constant and 'a' is the reaction order. Assuming first order reaction kinetics allows estimation of the half-life ($t_{1/2}$) of the transformation process (Equation 4.2)

$$t_{1/2} = \ln(2)/k \qquad \text{Equation 4.2}$$

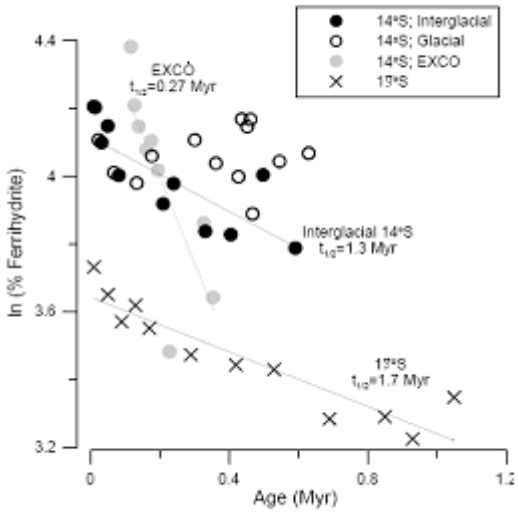

Figure 4.4.4: Ln(% ferrihydrite) plotted against inferred sediment age for sediments from 14°S compared with the 0.36Ma EXCO site (Dunk, 2004) and sediments from 19°S (Poulton & Canfield, 2006). $t_{1/2}$ is the half-life of the conversion of ferrihydrite to goethite (assuming first order reaction kinetics). The 14°S data have been separated into glacial and interglacial sections. Solid lines represent least squares fits through the data.

The transformation in the 14°S sediments is obviously more complex than a first order process because the data do not fall on a linear array when plotted as Ln (% ferrihydrite) against age. The interglacial sediment exhibits a similar half-life for transformation from ferrihydrite to goethite (1.3 Myr) as sediments from 19°S (1.7 Myr; Poulton & Canfield, 2006). However in the glacial sediments there appears to be no trend with age. The sediments from the 0.36Ma EXCO site (Dunk, 2004) show completely different behaviour to both the suboxic 14°S sediments and the more oxic 19°S sediments with much faster alteration of ferrihydrite phases to a more crystalline goethite phase. It appears that the interglacial sediments at 14°S show similar behaviour to the 19°S site, but undergo a distinct behavioural change under glacial conditions. Either ferrihydrite transformation in glacial periods is somehow impeded, perhaps by the redox status of the sediment and increased suboxic diagenesis, or there is an excess of ferrihydrite in the sediment that not supplied directly from the hydrothermal plume. Ferrihydrite could be produced as the results of oxidation of sulphide material during early diagenesis. Increased supply of

particulate sulphides to the sediments from the plume during glacial periods would result in an increase in the amount of ferrihydrite in the sediment

4.5 Behaviour of the divalent cations, Cu and Zn

Both Cu and Zn display a linear relationship with Fe and Mn (Figure 4.5.1). This implies they are strongly associated with the hydrothermal plume fallout. Although Cu and Zn are usually considered to be chalcophile elements that associate primarily with the sulphide phases that form the initial fallout from the buoyant hydrothermal plume (Feely et al., 1992), in these sediments Cu and Zn elements are dominantly associated with the amorphous Fe and Mn oxides. Both Cu and Zn have previously been found to associate with Fe and Mn (hydr)oxides in Pacific hydrothermal sediments (Cronen & Hodkinson, 1997). The co-precipitation of Zn and Cu within the buoyant hydrothermal plume is very efficient, and the ratio to Fe dependent on the element/Fe of the original solution (Savenko, 2001). As the Cu/Fe covaries closely with Zn/Fe and Mn/Fe distribution could also largely be controlled by phase transformations during early diagenesis.

The similarity between the trace metal/Fe ratio of the 14^{o}S sediment cores and that of the Nazca plate end member (Dymond, 1981) suggests that the vent source is the dominant input to sediments at this latitude. Deep Pacific water would impart a Cu/Zn ~0.3 if both elements are scavenged quantitatively from seawater, whereas in these sediments Cu/Zn = 2.51 ± 0.56 confirming the dominant hydrothermal source of metals to this sediment site.

Table 4.5.1: Divalent cation/Fe ratios in SEPR sediments

	Cu/Fe wt/wt *10^{-3}	**Zn/Fe** wt/wt *10^{-3}
GS7202-35 (14.5^{o}S)	5.4 (1.0)	2.1 (0.3)
Dunk (2003)		
EXCO 0.36 Ma site	4.1 (0.7)	1.7 (0.2)
EXCO 1.9 Ma site	5.1 (0.9)	2.3 (0.7)
Dymond (1981)		
Nazca Plate HT End Member	4.2	1.9

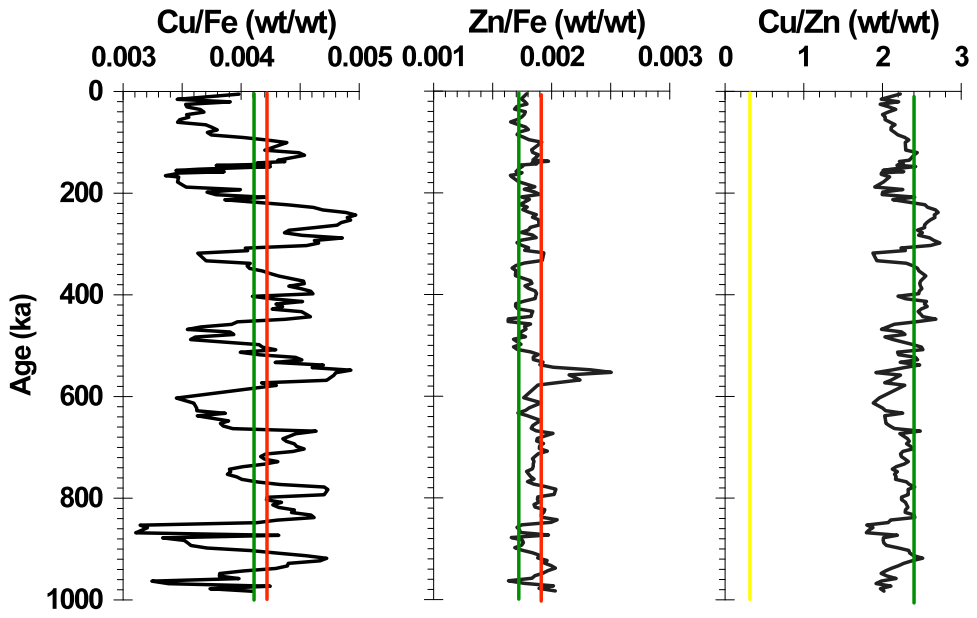

Figure 4.5.1: Down core Cu/Fe, Zn/Fe and Cu/Zn ratios. Red line indicates the ratio in the Nazca plate hydrothermal end member (Dymond, 1981). Green lines indicate the ratio in the 0.36Ma EXCO site at 14°S (Dunk, 2004) and the yellow line indicates the Cu/Zn ratio in deep Pacific seawater

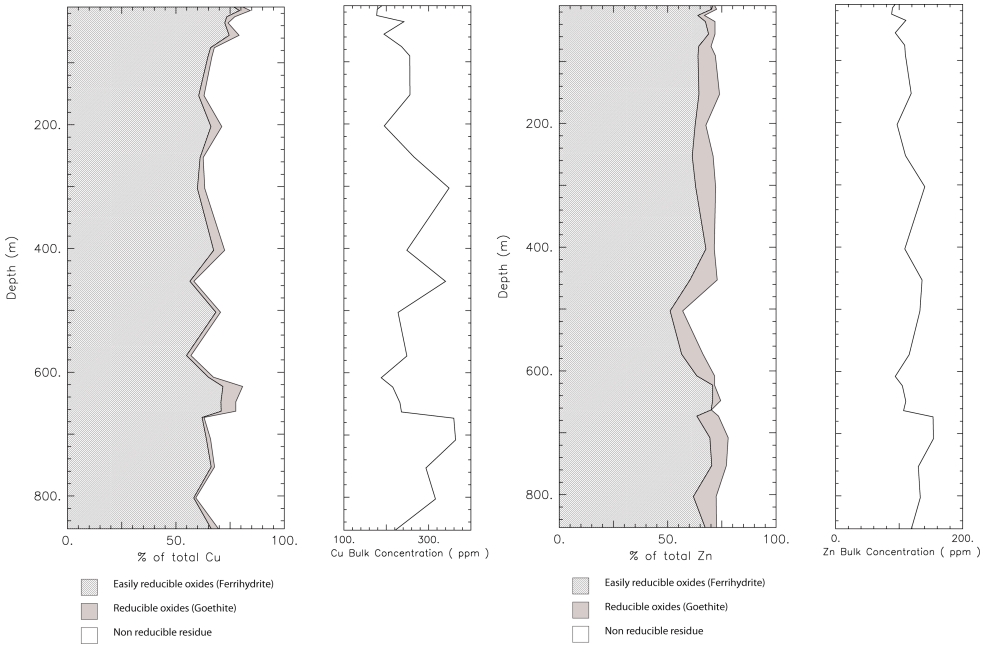

Figure 4.5.2: Fractionation of divalent trace metals Cu and Zn and corresponding bulk element concentrations. The sequential extraction separates the bulk solution into 3 fractions: Easily reducible oxides (hatched); Reducible oxides (grey) and the non reducible residue (white). Data is presented as % of the bulk concentration

Sequential extraction data for Cu, Zn, Ni are contained in Appendix 2 Table A2.4. Cu and Zn have a similar distribution down-core. The easily reducible fraction shows an increase from ~42% at the core top to ~55% at the core bottom. Cu has a small concentration in the more crystalline reducible fraction (~2.7-4.5%), while Zn does not. The residual fraction is similar for both elements (~17-28%).

4.6 Oxyanion behaviour in the sediments: V, P and As and U

The primary source of the oxyanions HVO_4^{2-}, HPO_4^{2-} and $HAsO_4^{2-}$ to the sediment is scavenging by the Fe and Mn phases precipitating from the plume. P/Fe, V/Fe and As/Fe have been found to be constant in the neutrally buoyant plume over distances of 25km (Rainbow vent field, Feely et al., 1992; Edmonds & German, 2004). Table 4.6.1 shows Oxyanion/Fe ratios in different EPR sediments. As and V behave linearly with Fe in the sediment (Figure 4.6.1). The As/Fe ratio of the sediments is consistent with that of the overlying plume and other sediments in the area. However the mean V/Fe is elevated with respect to both plume values and those of oxic sediments from the same latitude (Table 4.6.1).

V/Fe ratio is consistently higher than the ratio of the overlying plume. The difference becomes more pronounced with depth. The higher ratios indicating more V is present than can be accounted for by the overlying plume alone. P/Fe in the sediment is considerably lower than might be expected from the plume ratios. P/Fe also deviates significantly from linearity

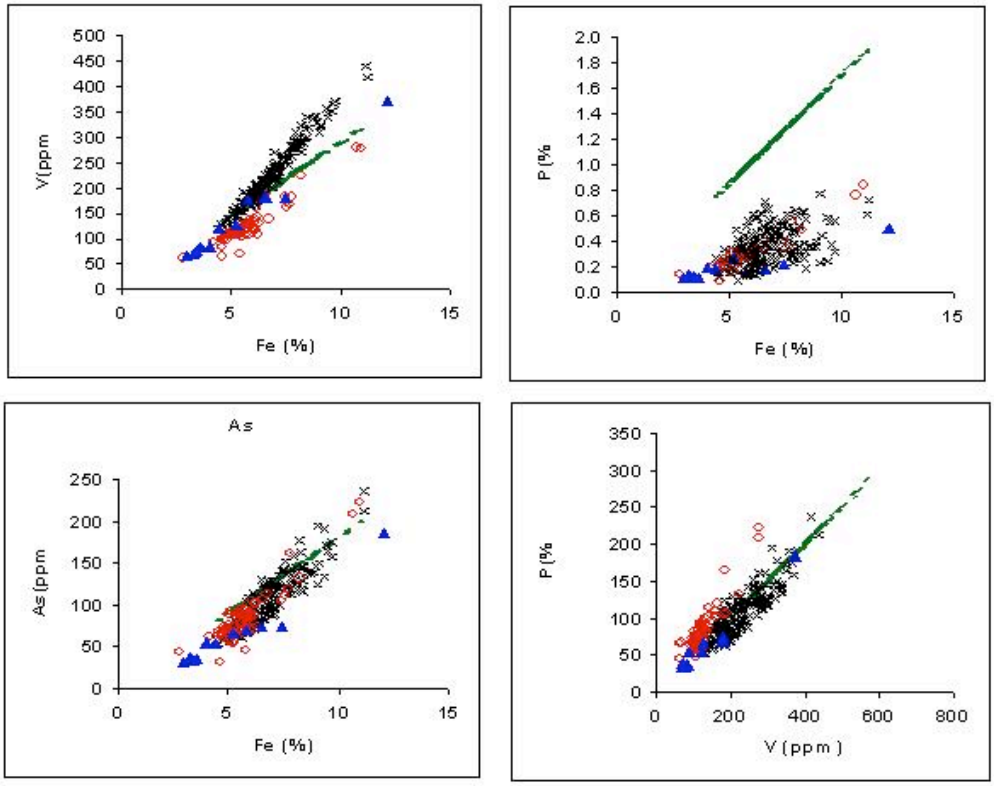

Figure 4.6.1: Oxyanion/Fe ratios in SEPR sediments from 14°S west of the axis (Black crosses), oxic sediments at 14°S east of the axis (blue triangles; EXCO core 12, Dunk 2004) and suboxic sediments at 10°S (Red circles; Schaller et al., 2000). The green line indicates the ratio in the 13-19°S hydrothermal plume (Feely et al., 1996)

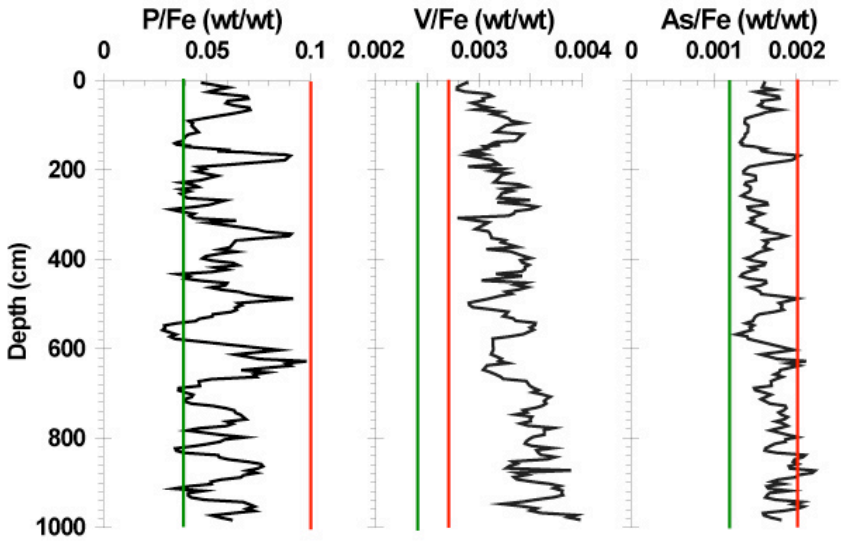

Figure 4.6.2: Downcore oxyanion/Fe ratios. The red line indicates the mean ratio in the overlying plume (Feely et al., 1996) and green lines indicate the mean ratio for the 0.36Ma EXCO sediments.

There is a strong inverse correlation between phosphate concentration in deep ocean waters and V/Fe in the underlying hydrothermal sediment. This is inferred to be due to the competition between P and V in scavenging by Fe. Variations in P and V in metalliferous sediment could therefore potentially reflect the variations in the concentrations of these elements in seawater through time (Feely et al., 1990b; German et al., 1991b). The sediments ratios of V/Fe and P/Fe are broadly mirror images, with peaks in P/Fe corresponding to troughs in V/Fe and vice versa (Figure 4.6.2). The As/Fe ratio behaves similarly to the P/Fe. However V is significantly mobilised when conditions are even mildly suboxic, therefore the sedimentary V/Fe is greatly compromised (Schaller et al., 2000). There is a strong positive relationship between P/Fe in ferrihydrite precipitates and seawater dissolved phosphate. Inter-ocean variability in dissolved P controls the P/Fe and V/Fe in primary hydrothermal Fe precipitates. Variation of phosphate through time could potentially be caused by changes in hydrothermal activity (on Ma timescales) or by redistribution of nutrients (on glacial-interglacial timescales). The controls on oxyanion/Fe ratios through time are discussed in Chapter 5.

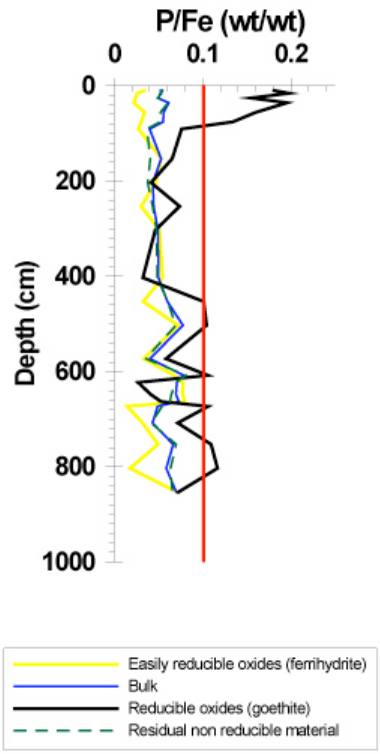

Figure 4.6.3: Downcore P/Fe distribution in different phases. Red line indicates ratio of overlying plume (Feely et al., 1996)

Table 4.6.1 Oxyanion/Fe ratios in SEPR sediments (Figures in brackets are 2σ)

	V/Fe	P/Fe	As/Fe
GS7202-35 (14.5°S)	0.0033	0.053	0.0015
Dunk (2004)			
EXCO 0.36 Ma sediment	0.0024 (0.0003)	0.039 (0.008)	0.0012 (0.0002)
EXCO 1.9 Ma sediment	0.0023 (0.0003)	0.039 (0.010)	
Feely et al. (1996)			
13-19°S plume	0.0027	0.100	0.0020
Schaller et al. (2000)			
10°S sediment	0.0022 (0.0003)	0.049 (0.011)	0.0014 (0.0003)
Marchig et al. (1986)			
18.5°S sediment		0.055	0.0017

Sequential extraction data show that only a small amount of V is bound to the easily reducible hydrous ferric oxides; it is predominantly associated with a non-reducible phase (~91-93%) - i.e. a more crystalline phase (Figure 4.6.4). However both P and As have a significant easily reducible fraction (~51-68%; ~43-74% respectively) bound to the easily reducible amorphous oxyhydroxides, with a small percentage found in the reducible oxides. There is still an appreciable fraction (P: 24-30%; As: 14-36%) of both elements bound to a non-reducible phase. This is more variable for the As.

The V/Fe ratios in the ferrihydrite and goethite phases are significantly lower than those in the overlying plume (Figure 4.6.5) – these phases are depleted in vanadium with respect to the plume Fe input. However the non-reducible phase shows a V/Fe greatly in excess of the plume values i.e. the majority of the vanadium in the sediments is associating with the non-reducible phases. This is in contrast to the behaviour displayed in the EXCO sediments, where the majority of the V is associated with the amorphous (i.e. easily reducible phases). The low V/Fe in the residual phase here is explained by discrimination of V during the transformation of ferrihydrite to goethite. As there is still agreement between the V/Fe (amorphous + residual) and the overlying plume ratios in the EXCO sediments, it is assumed that rejected V is retained in the sediment column. At 14^{o}S the V content of the goethite phase is negligible – all the V is contained within the easily reducible (ferrihydrite) and non-reducible (residual) phases. This suggests that the V has undergone transport to a phase that is not readily reducible, but is not crystalline in XRD.

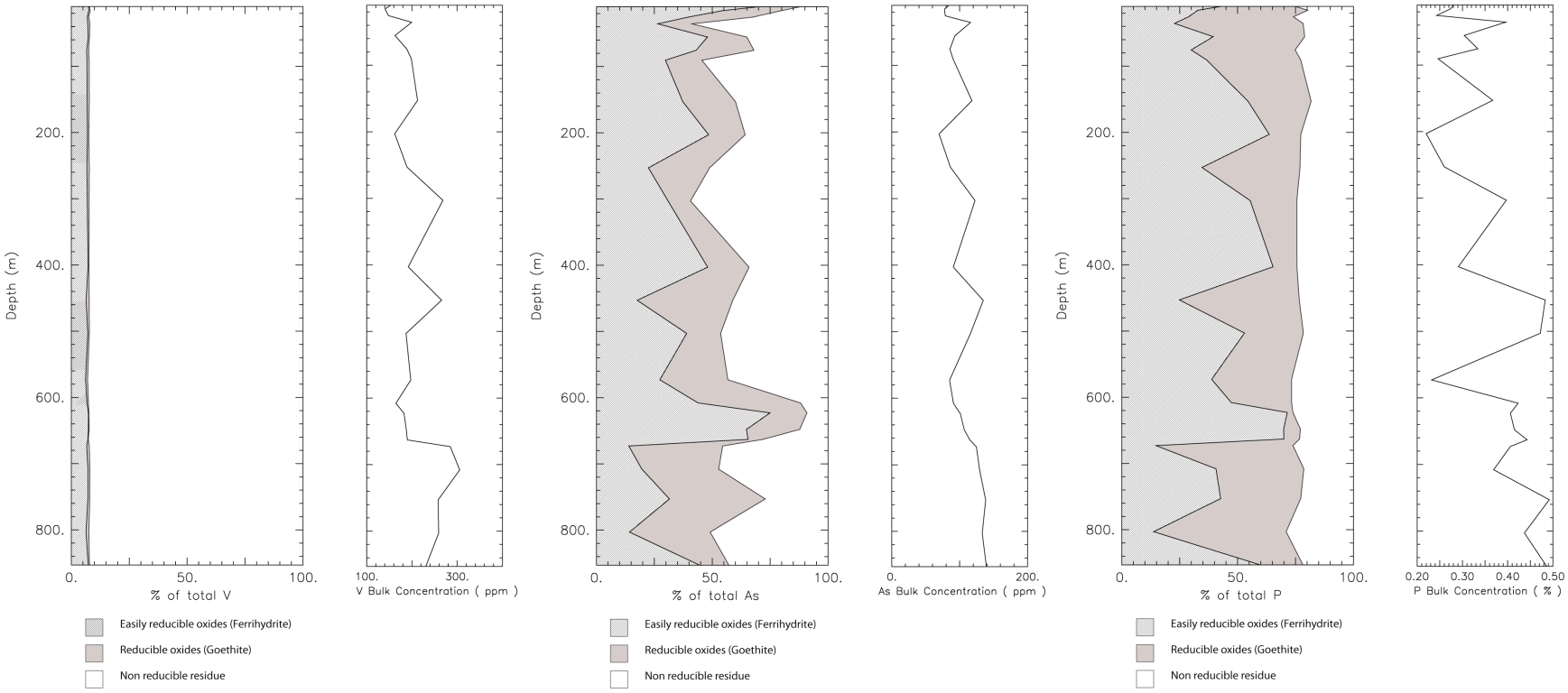

Figure 4.6.4: Fractionation of oxyanions V, As and P. This sequential leach separates the bulk solution into 3 fractions: Easily reducible oxides (hatched); Reducible oxides (grey) and the non reducible residue (white). The data are presented as % of the bulk concentration.

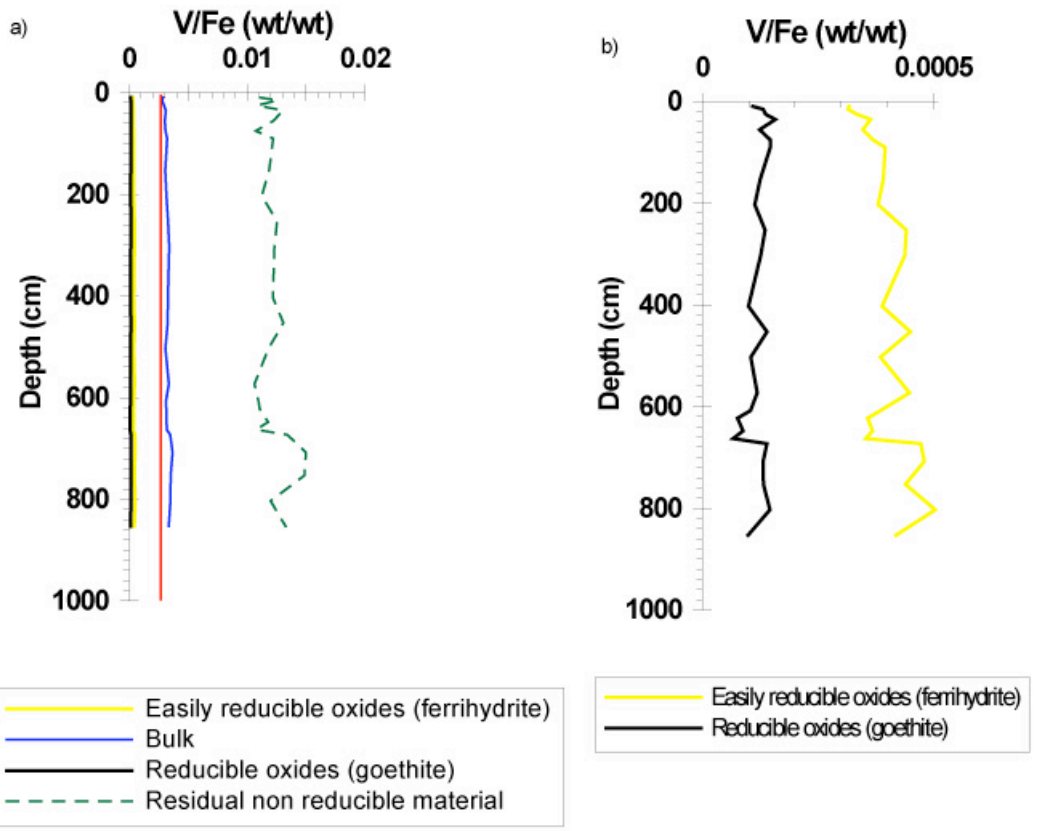

Figure 4.6.5: a) Downcore distribution of V/Fe in different phases. Red line indicates the plume ratio b) V/Fe in easily reducible and reducible phases (expanded scale from a)

The behaviour of uranium as a redox-sensitive element and variations in the bulk U/Fe ratio have previously been discussed in Chapter 3.7. Sequential extraction shows some partitioning of U between the different Fe phases (Table 4.7.1) The majority of the U is associated with the amorphous ferrihydrite phases, but there is still a significant fraction in the reducible and residual phases (Figure 3.7.5) in the top 5 metres of the core. The highest concentrations (and U/Fe ratios) in the residual fraction correspond to the highest U enrichment peaks, which indicate the prevalence of more suboxic conditions. Below 5m, (the point of highest U concentration) the U content of the residual phase drops to near zero and the majority of the U is located in the amorphous phases.

Table 4.6.1: Partitioning of U between sequential leach Fe phases. U_{bulk} is the U concentration measured by ICP-MS. U_{ferr} corresponds to the easily reducible phase (i.e. associated with ferrihydrite), U_{goet} corresponds to the reducible phase (i.e. associated with goethite) U_{res} is the $U_{bulk} – (U_{goet} + U_{ferr})$

Sample ID	Age (ka)	Depth (cm)	U bulk (ppm)	U_{ferr} (ppm)	U_{goet} (ppm)	U_{res} (ppm)
SLTTC3	13.326	15.5	5.5	3.51	1.21	0.785
SLTTC5	22.793	25.5	3.7	2.40	0.89	0.407
SLTTC7	31.810	35.5	6.4	3.67	1.68	1.074
SLTTC11	49.842	55.5	5.8	4.01	0.85	0.911
SLTTC15	67.875	75.5	5.7	3.53	0.98	1.177
SLTTC18	81.399	90.5	2.7	2.12	0.48	0.055
SLTPC4	133.125	153	6.2	4.27	0.46	1.455
SLTPC14	176.804	203	2.9	2.26	0.11	0.547
SLTPC24	209.352	253	2.6	2.11	0.37	0.152
SLTPC34	239.859	303	4.7	2.96	0.32	1.464
SLTPC54	300.874	403	4.2	3.13	0.15	0.931
SLTPC64	331.382	453	5.3	3.75	0.69	0.828
SLTPC74	361.99	503	12.1	9.38	0.90	1.821
SLTPC88	404.933	573	4.4	3.63	0.23	0.551
SLTPC95	426.969	608	15.7	12.29	1.00	2.367
SLTPC98	436.453	623	15.7	11.67	0.28	3.775
SLTPC103	452.261	648	15.1	10.86	0.41	3.783
SLTPC106	461.745	663	13.0	9.63	0.25	3.167
SLTPC108	468.068	673	14.2	8.71	1.97	3.552
SLTPC115	498.28	708	11.4	9.38	0.89	1.104
SLTPC124	545.760	753	12.4	11.48	1.12	0.000
SLTPC134	591.106	803	11.9	10.07	1.48	0.302
SLTPC144	629.953	853	8.4	8.09	0.58	0.000

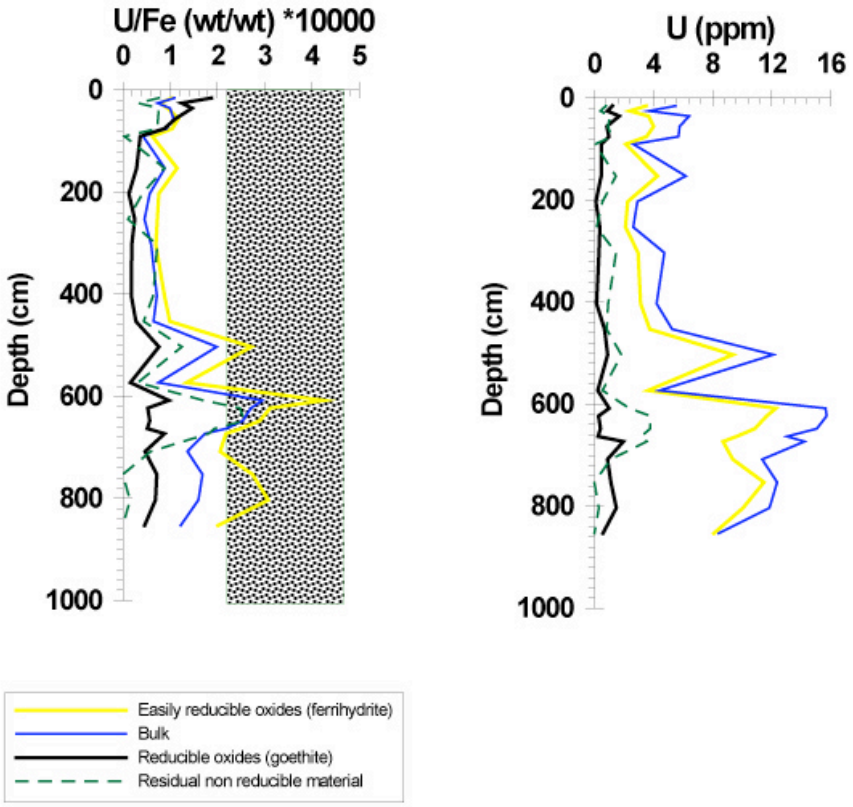

Figure 4.6.6: a) Fractionation of a) U/Fe and b) bulk U with time. The hatched area indicates the ratio in EPR plume particles (German et al. 2002)

4.7 Summary

This chapter aimed to investigate the mechanisms controlling the distribution of trace elements and oxyanions in a ridge flank setting.

Plume derived Fe and Mn (hydr)oxides are subject to alteration both in the ageing neutrally buoyant plume and after sedimentary deposition. Variability in the Fe/Mn ratio is the result of fractionation during early sedimentary diagenesis and variation at source. The Fe/Mn range in these sediments (2.12-3.7) is consistent with other sediments from the area, but the mean value is low. There appears to be an excess of Mn with respect to Fe compared to other sediments in the area. Plume Fe/Mn is relatively constant, therefore this must be associated with post depositional uptake of Mn from either seawater or low temperature circulating fluids. Precipitation of Mn oxide phases requires that the sediment be close to oxic in nature, a result of the limited amount of electron donor available due to the low levels of organic material in the sediment and that there are no fine grained sulphides remaining.

Sequential leaches of the sediment show that significant ferrihydrite has been transformed to goethite and other non-reducible phases. Using a first order kinetic model, the degree of transformation can be assessed using a plot of ln(% ferrihydrite) against time (as derived from the age model) The glacial and interglacially deposited sediments in this core display two distinct behaviours. The interglacial sediments display behaviour similar to that observed at 19^{o}S with a half life for ferrihydrite phases of ~1.3 Myr. However ferrihydrite transformations under glacial conditions appear to be impeded; there is little change in the proportion of more crystalline phases downcore. This is inferred to be a function of a distinct change in sediment redox status under glacial conditions.

The divalent cations Cu and Zn are hydrothermally derived and co-vary with the Fe and Mn content of the core. Both elements show similar portioning with the Fe phases, where the largest fraction is associated with the easily reducible ferrihydrite phase. The oxyanions P, V and As are scavenged by the Fe and Mn (hydr)oxides precipitated from the hydrothermal plume. As the P/Fe and As/Fe ratios of the sediment are less than that

of the overlying plume, the concentrations of these elements observed in the sediment could be completely supplied by the plume. The V/Fe is elevated with respect to plume values, i.e. V is enriched with respect to the Fe content of the sediment. This enrichment relative to Fe increases with increasing depth (i.e. increasing sediment age and increasing distance from axis). The strong inverse correlation between V/Fe and P/Fe is inferred to be the result of competition in the scavenging of the two elements by Fe. V is significantly mobilised in sediments that are only slightly suboxic. Sequential leach data indicate that the majority of the V is bound to a non reducible phase, with only a small (relatively constant) % associated with the amorphous ferrihydrite phases. The V/Fe in the ferrihydrite and goethite phases is considerably lower than that of the plume, while the ratio in the non reducible phase is greatly in excess of plume values i.e. V that has been discriminated against in the amorphous phase remains in the sediment column associated with the non reducible phase.

The majority of the U is located in the amorphous ferrihydrite phase. There is still a significant fraction in the goethite and non reducible phases in the top 5 m of the core, but below this horizon – which is the locus of the highest U enrichment - the fraction of U phases other than ferrihydrite reduces to practically 0. However, there is a significant fraction in the residual non-reducible fraction at the depth of the largest U enrichment.

The hydrothermal material in the sediment is recrystallised to more stable forms that become locked in the sediment. The scavenging of oxyanions by Fe and Mn oxyhydroxides acts as an effective sink of these elements. The elements are released during recrystallisation of Fe (hydr)oxides to more stable, non reducible, phases, during recrystallisation. The degree of alteration occurring appears to be controlled by the redox status of the sediments, which appears suppressed in glacial periods. Therefore the preservation of the hydrothermal material in the sediments and the degree to which they are a permanent sink for the oxyanions varies on a glacial-interglacial basis, which must be taken into account when considering the impact of the hydrothermal sink on trace element budgets in the oceans.

Chapter 5: Oxyanions as paleoproxies in hydrothermal sediments

5.1 Aims

The eastern equatorial and tropical Pacific regions are areas of significant air-sea flux and upper ocean-deep ocean exchange in the global CO_2 cycle, and therefore potentially exert an important control on global climate. Understanding changes to ocean chemistry and circulation in this region is therefore of great importance. Eastern Pacific paleoceanographic records of past ocean conditions are significantly perturbed by calcite dissolution and masked by hydrothermal inputs over much of the region. The redox status of Pacific sediments is controlled by organic carbon delivery to the seafloor and bottom water oxygen content. The distribution of redox sensitive elements in hydrothermal sediments could potentially be used to reconstruct past sediment redox conditions. The aim of this chapter is to evaluate the potential for use of oxyanions and trace metals associated with redox sensitive elements such as Fe and Mn as proxies for past ocean conditions.

5.2 Introduction

Sediments from the Eastern Equatorial Pacific (EEP) have been widely used for paleoceanographic reconstructions over glacial-interglacial timescales because this area is thought to be an important regulator of atmospheric pCO_2 (e.g. Tans et al., 1990). Shifts in the locus and magnitude of oceanic primary production and associated carbon export significantly affect the global carbon cycle and climate (e.g. Hansell et al., 1997). The sediment records from equatorial upwelling regions indicate that there has been significant change in productivity throughout the late Pleistocene (e.g. Sarnthein et al., 1988; Lyle et al., 1988; Pederson et al., 1988, 1991; Mix 1989). There is significant debate over the magnitude and even direction of the changes in the Eastern Equatorial Pacific (EEP) inferred from a range of different proxies in the sediment record and the implications for global climate (e.g., Loubere et al., 1999; Pederson et al., 1991; Sanyal et al., 1997; Schrader & Sorknes, 1990). Sediment accumulation has been previously found to be much higher during the Last Glacial

Maximum (LGM) than today (e.g. Lyle et al., 2002). This has been interpreted as reflecting an increase in upwelling, and an increase in the calcite flux (Paytan et al., 1996; Sanyal et al., 1997). The difficulty in using sedimentation rates as a proxy for past productivity is that they are very dependent on the age model applied to the sediment, and can be greatly influenced by sea-floor sedimentary processes such as focusing (Loubere & Richaud, 2007).

Alternative age-model independent proxies, and proxies that can be normalized to ^{230}Th, have been in direct conflict with sediment accumulation data, and indicate lower calcite production during the LGM (e.g. Loubere, 2000, Bradmiller et al., 2006). Suggested explanation for this disagreement has been increased lateral transport of sediment during the LGM elevating sediment accumulation rates as opposed to increase in the overlying productivity. However there is some dispute as to whether sediment supplies and distribution in the tropical East Pacific is sufficient to account for the degree of focusing required to account for the ^{230}Th normalization studies (Francois et al., 2007; Lyle et al., 2005). A recent re-evaluation of the age model applied to some sediment accumulation studies has revealed a systematic offset in the timing of the LGM to deglacial interval (Loubere & Richaud, 2007). Correction for this offset goes some way to bringing sediment accumulation data in line with other age-model independent proxies, although there is still a discrepancy between the different techniques, suggesting there is still a significant degree of lateral transport.

Low sediment accumulation rates in the East Pacific region (e.g. Dymond, 1981; Dunk & Mills, 2006; Hauschild et al., 2003) mean that the proxy record is poorly resolved and carbonate rich sediments only accumulate above the relatively shallow Pacific lysocline along the EPR where there is significant hydrothermal input. The East Pacific Rise at 15^{o}S is the locus of the largest metalliferous sediment anomaly (Bostrom & Peterson, 1969, Figure 3.2.2) and water column primordial helium (δ^{3}He) anomaly (Lupton & Craig, 1981) (Figure 3.2.1). The relatively smooth topography of the fast spreading ridge axis allows effective dispersal and linear sedimentation of hydrothermal inputs from the westerly-dispersed neutrally buoyant plume (Hauschild et al., 2003). These sediments are the target of this study to evaluate the preservation of primary paleoceanographic signals in hydrothermal sediments.

The trace element record in metalliferous sediments can potentially reveal past changes in ocean chemistry (e.g. Feely et al, 1991, 1996, 1998; German et al., 1997). This has been effectively exploited to determine the paleoceanographic Os isotopic composition of seawater (Ravizza & McMurtry, 1993; Oxburgh, 1998). Problems arise when using trace element distributions for paleoceanography because the record can be seriously perturbed during early sedimentary diagenesis (e.g. Schaller et al., 2000). Furthermore, in sediments with low accumulation rates, bioturbation and sediment redistribution smoothes record of past changes (e.g. Bender et al., 1971, Oxburgh 1998, Shimmield & Price, 1988).

Potentially the distribution of redox sensitive trace metals, such as U, Mo, P, As and V, is a powerful tool in the reconstruction of past redox conditions which in turn reflect productivity and export of carbon to the deep ocean (e.g., Pallier et al., 2002). Redox sensitive trace elements are present in seawater as oxyanions ($UO_2(CO_3)_3^{4-}$, MoO_4^-, HVO_4^{2-}, HPO_4^{2-} and $HAsO_4^{2-}$). Oxyanions exhibit a high affinity for the fine grained Fe-oxyhydroxide particles which precipitate rapidly in hydrothermal plumes as vent fluid mixes with ambient seawater (Rudnicki & Elderfield, 1993). The dissolved oxyanions are co-precipitated with the Fe-oxyhydroxides leading to a distinct oxyanion/Fe ratio in hydrothermal plume particles. This ratio reflects the local oxyanion distribution, rate of precipitation and proximity to the vent site (e.g. Feely et al., 1987, 1990; Metz & Trefry, 1993). Plume dispersion and the corresponding sedimentation leads to a significant flux of metals to the underlying metalliferous sediments. Metalliferous sediments act as a significant sink for some oxyanion species (e.g. Trocine & Trefry, 1988; Trefry & Metz, 1989, Feely et al 1991, 1994). If conditions in the sediment are fully oxic, then it appears that the oxyanion/Fe signal is preserved to a degree, although ridge flank hydrothermal circulation and hydrogenous enrichment of certain elements are important processes at many sites (Dunk & Mills, 2006) and can perturb the sedimentary ratios. The extent to which the oxyanion/Fe ratios are perturbed by diagenesis in suboxic sediments has been previously investigated (e.g. Schaller et al., 2000). The mechanisms and controls of these processes are not completely understood and the oxyanion distribution in hydrothermal sediments has yet to be effectively exploited for useful paleoceanographic reconstructions.

5.3 Results

Variation of oxyanion/Fe ratios through time has been assessed using the age model described in Chapter 3. The timing of Marine Isotope Stages was taken from Imbrie et al., (1984).

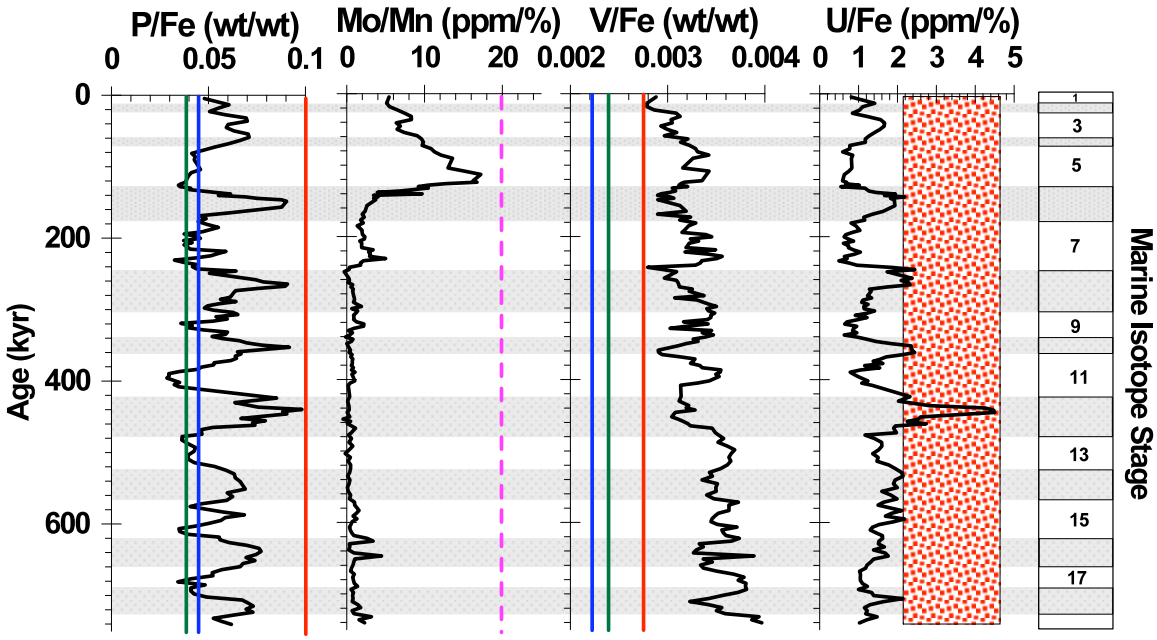

Figure 5.3.1 Downcore distribution of P/Fe, Mo/Mn, V/Fe and U/Fe. Red lines and red shaded area indicate oxyanion/Fe ratios as measured in the 13°-19°S Plume (Feely et al., 1996; German et al., 2002). Green lines indicate the ratio in the 0.36Ma EXCO sediments. Blue lines indicate the ratios in 10°S sediments (Schaller et al., 2000). The pink dashed line indicates the Mo/Mn ratio in oxic sediments. Glacial stages are indicated by shaded boxes, numbers refer to the marine isotope stages (1-19).

5.4 Behaviour of Phosphorus on an interglacial/ glacial timescale

As mentioned in Chapter 1, phosphorus is an essential nutrient in biogeochemical cycles. It has been implicated as a potentially important limiting factor for primary production in the ocean (Karl et al., 1993). The uptake of dissolved phosphate from seawater by hydrothermal plume particles and hydrothermal circulation through both the axis and ridge flanks is an important sink in the global P cycle (Berner 1973; Froelich 1982, Feely et al., 1990, Wheat et al., 1996). Hydrothermal processes are a significant sink for phosphorus, potentially removing up to 33% of the global riverine input (Wheat et al., 1996). P and Fe in Pacific Ocean hydrothermal plume particles exhibit relatively linear relationship (Feely et al., 1996).

There are several possible controls on the P/Fe ratio in the sediments. The P/Fe ratio is partially controlled by the bottom water phosphate content. This in turn is controlled by the 'age' of the water mass i.e. by the strength and patterns of the deep ocean circulation and can be variable both in time and space. The P/Fe ratio could also be affected by chemical alteration of the plume during transit and diagenesis in the sediments post deposition.

Near-field (<10 km from source) oxic hydrothermal sediments appear to retain the plume derived P/Fe ratio; sediments from beneath the Rainbow hydrothermal plume on the Mid Atlantic Ridge, where the bottom water is well oxygenated, have similar P/Fe ratios to those measure in neutrally buoyant plume particles (Cave et al., 2002). However, where suboxic and oxic diagenesis is occurring in sediments further removed from source, it appears that P is lost with respect to Fe. Suboxic sediments collected from 10^{o}S on the EPR have P/Fe ratios approximately 50% that of sampled plume particles (Schaller et al., 2000). The preservation of the primary P/Fe signal is inferred to be controlled largely by post depositional reactions (Poulton & Canfield 2006).

At 14°S the EPR axis at 2500m depth intercepts both a major oxygen minimum ([O_2] ~75 μmol/kg), and a dissolved phosphate maximum (Figure 5.3.2). Hydrothermal vent fluid in a rising buoyant plume would be injected into a water mass with low relative O_2, concentrations and high phosphate concentrations. These conditions could lead to slower oxidation of the fine grained sulphide particles precipitating from the hydrothermal plume, which would go some way to explaining the elevated P/Fe ratios in the 13°S-19°S EPR plume particles (Feely et al., 1996) with respect to plume particles forming in more oxygenated waters (e.g. Rainbow; Feely et al., 1992; Cave et al., 2002). Furthermore 14°S is located at the margins of sharp gradients in oxygen and phosphate, therefore it is reasonable to assume that a relatively minor alteration of the strength of ocean circulation could have significant implications for the P/Fe of the underlying sediments.

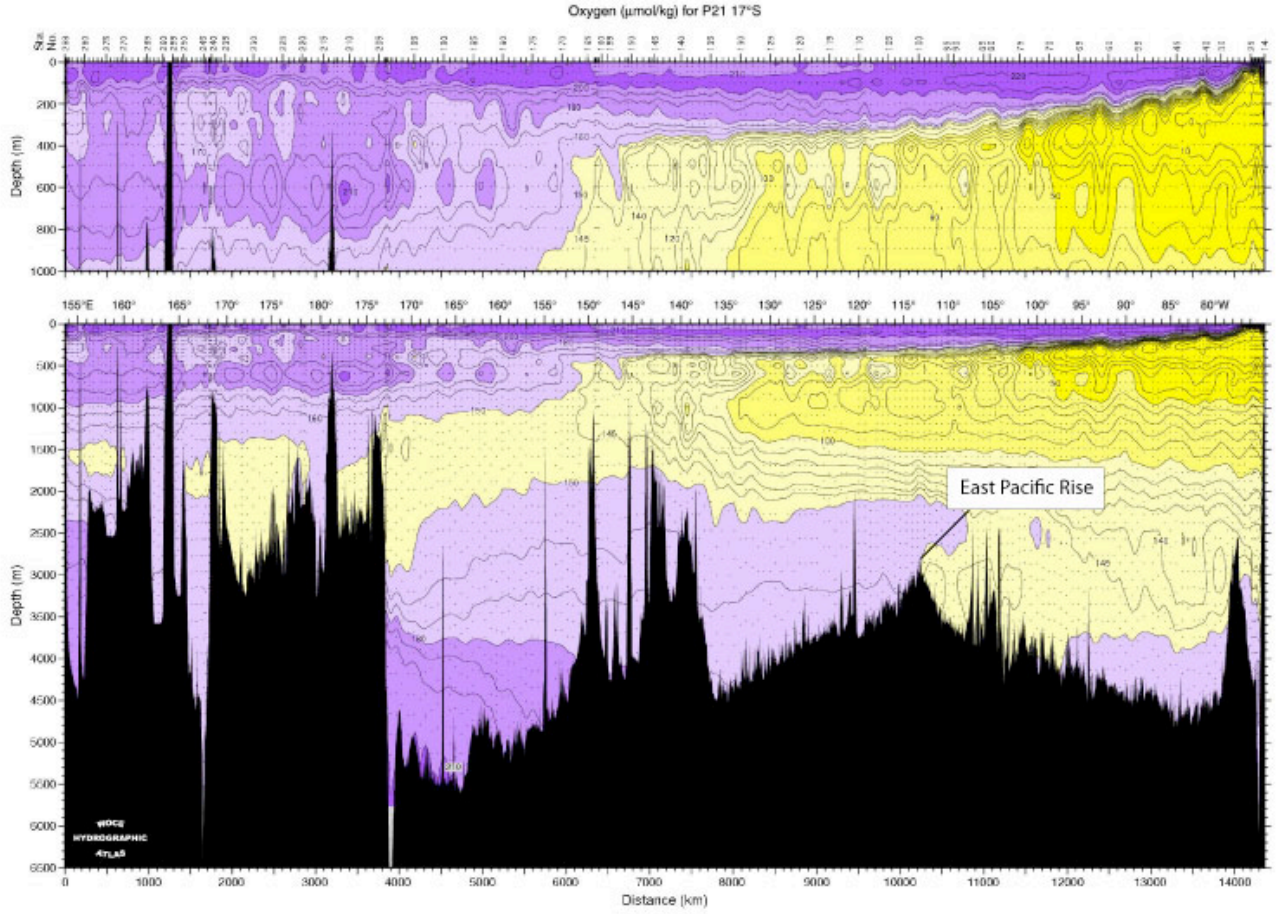

Figure 5.3.2: Dissolved oxygen distribution along WOCE line P21 (17°S). Reproduced from the WOCE Pacific Ocean Atlas, (Talley, 2007) Contour lines indicate oxygen concentration in µmol/kg Yellow shading indicates the area of oxygen depletion.

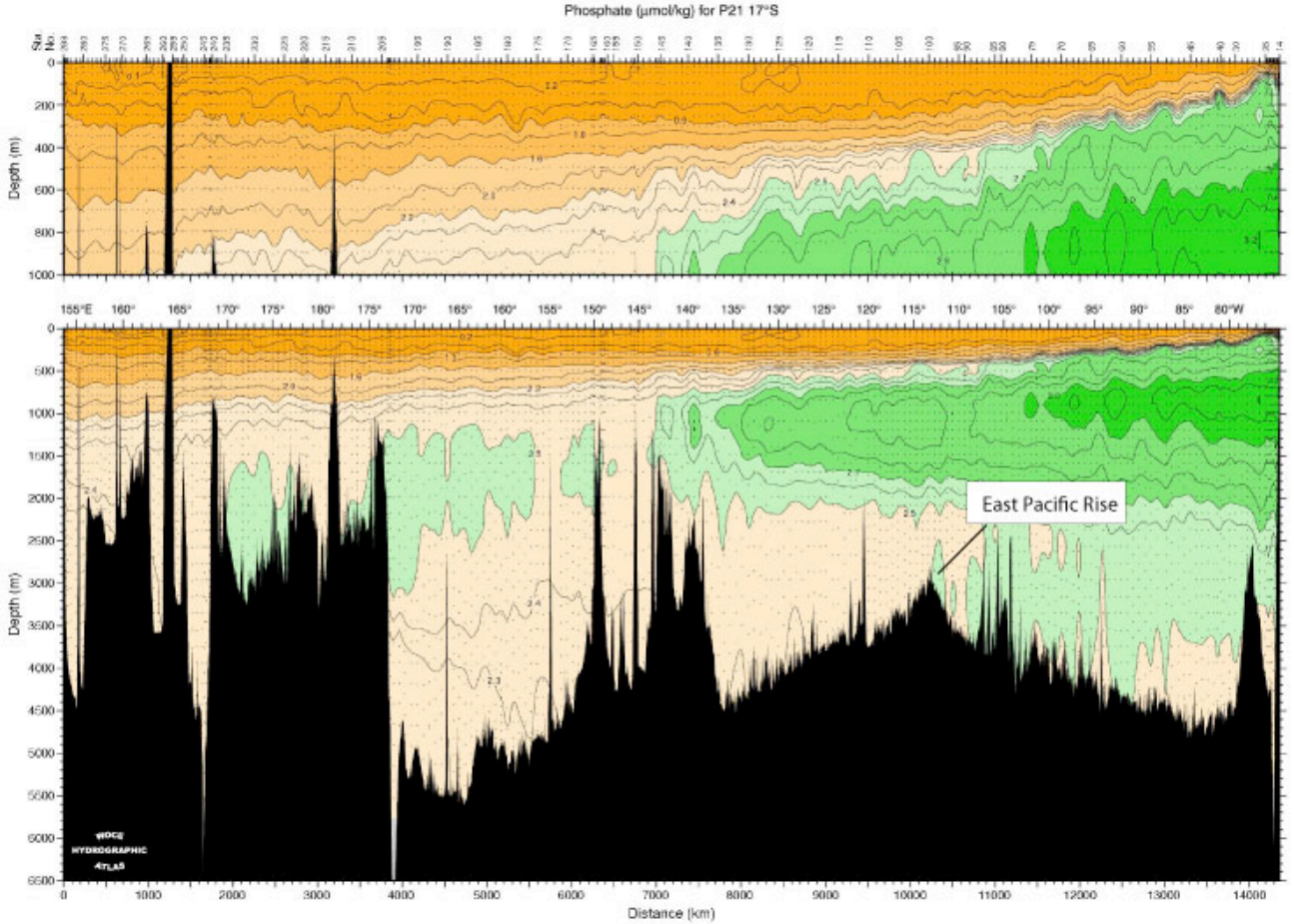

Figure 5.3.3: Dissolved phosphate distribution along WOCE line P21 (17°S). Reproduced from the WOCE Pacific Ocean Atlas, (Talley, 2007) Contour lines indicate phosphate concentration in µmol/kg. Green indicates the area of highest phosphate

Transformation of hydrothermally formed ferrihydrite to more crystalline phases can occur very quickly in the laboratory (half lives of days to weeks, Zhao et al., 1994; Cornell & Schwertmann, 1996). The Fe transformations kinetics in this core have been previously discussed in Chapter 4.4. This kinetic model can be used to give some insight into the impact of the water column on the degree of alteration of ferrihydrite in the sediments. Figure 4.4.4 shows ln(% Ferrihydrite) versus time (derived from the sediment age), and the ferrihydrite half-life was inferred, assuming first order reaction kinetics, to be much longer in this setting. The transformation of ferrihydrite can be described by equation 5.1.

$$-d(Fe_{ferr}/Fe_{bulk})/dt = k(Fe_{Ferr}/Fe_{bulk})^{a} \quad \text{Equation 5.1}$$

Where the gradient, k, is the rate of the chemical reaction, 'a' is the order of the reaction (1) and Fe_{ferr} and Fe_{bulk} are the Fe concentrations found in the ferrihydrite fraction and the bulk sediment respectively. The intercept is therefore approximates the % Ferrihydrite at t=0 i.e. the degree of ferrihydrite transformation that has already occurred in the water column prior to the sediments deposition.

At t=0 in the sediments from the 0.36Ma EXCO site the % Ferrihydrite is almost 100%, implying very little of the alteration is occurring in the water column. However, core GS 7202-35 has a significantly lower % ferrihydrite at t=0 – closer to 60%. This implies that the water column is having a much more significant effect on the transformation of Fe and that there is significantly more alteration occurring in transit of the hydrothermal plume. Alteration occurring in the sediment post deposition and uptake of P from seawater during sulphide oxidation will be offset by the loss of P due to recrystallisation.

While the sediments have trace metal distributions that are consistent with suboxic history, there is very little organic carbon present (0-1%±0.36; Chapter 4.4). Any organic carbon supplied to the seafloor from overlying productivity has been partially oxidised during early diagenesis. A potentially significant electron donor in this setting is plume transported sulphides derived from the vent system, which have subsequently been oxidised to Fe oxides. The lack of an electron donor means that

redox reactions within the sediments are suppressed and there is no evidence for ongoing mobilisation of elements such as Mn(IV) to $Mn(II)_{aq}$ at depth within the core.

Phosphorus is remobilised in the upper sediment column during both oxic and suboxic diagenesis, which implies relatively rapid transformation during sedimentary burial. The extent to which P/Fe ratios can be any use as an indicator of past ocean conditions is dependent on the extent to which P mobilisation occurs during diagenesis. There are three potential sedimentary sinks for P released as the recrystallisation of ferrihydrite occurs; (1) re-adsorption at the surface of the oxide mineral, (2) formation of an authigenic phase such as apatite ($Ca_5(PO_4)_3(F,Cl,OH)$), or (3) association with the newly forming secondary Fe phases such as goethite. (Poulton and Canfield, 2006) Any P not captured by any of these processes will diffuse from the sediment to the overlying water column.

As previously covered in Chapter 4, the mean bulk P/Fe in core GS 7202-35 is considerably lower than the values for SEPR hydrothermal plumes, but is consistent with other sediments from the region (e.g. Poulton and Canfield, 2006; Dunk, 2004). The P/Fe ratio varies on a glacial-interglacial timescale (Figure 5.3.4), being higher during glacial periods than interglacial periods. Oxic sediments from 0.36Ma EXCO site at 14^oS (Dunk 2004) exhibit P/Fe ratios with two distinct behaviours. Above 3m sediment depth, there is greater variability in the P/Fe ratio, which is slightly higher than at greater depth in the core (Figure 5.3.4). Below 3m the ratio becomes relatively constant.

P/Fe throughout the EXCO cores is depleted in P with respect to the values in the overlying hydrothermal plume. This is also true of the sediments form core GS 7202-35.

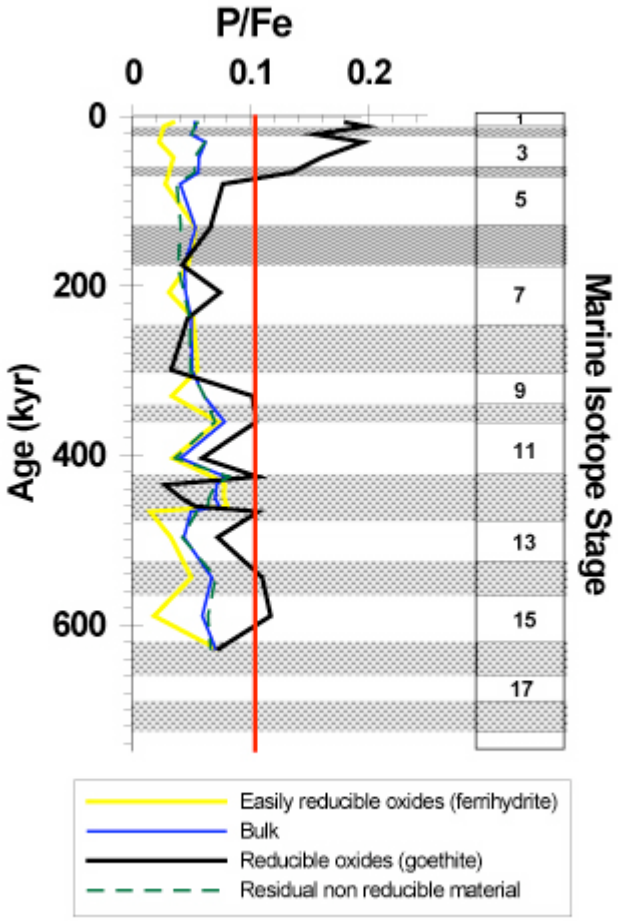

Figure 5.3.4 Downcore distribution of P/Fe associated with different Fe phases. The red line indicates oxyanion/Fe ratios as measured in the 13°-19°S Plume (German et al., 2002). Glacial stages are indicated by shaded boxes.

The partitioning of P with respect to Fe is discussed in Chapter 4.6. The P/Fe ratio in the ferrihydrite phase is lower than bulk ratios, while the P/Fe in the reducible goethite phase is dramatically higher in the top 0.5m of the core decreasing to a mean value slightly higher than the bulk sediment and other phases (Figure 5.3.4). This suggests that transformation to goethite can be a significant sink for P in this setting. The bulk sediment P/Fe at 10°S (Schaller et al., 2000) shows similar behaviour to the goethite phase here.

The % transformation of ferrihydrite to goethite is significantly different in glacial and interglacial stages, as shown in Chapter 4.4 (Figure 4.4.4). There is little

transformation during the glacial periods, resulting in high P/Fe ratios in the easily reducible Fe oxide fraction (ferrihydrite). During the interglacial periods, the sediments undergo a rate of phase transition similar to the sediments at 19^{o}S (Poulton & Canfield, 2006) and the P/Fe ratio of the ferrihydrite fraction is lower implying loss of P from this phase. This implies the glacial-interglacial variation in P/Fe is a function of the varied phase transformations observed downcore, which are in turn a function of the redox status of the sediment. The P/Fe ratio in the goethite fraction appears to be inversely related to the P/Fe in the ferrihydrite fraction, and the sum of the P/Fe in the two fractions equals that of the bulk sediment. This means that the P released when the ferrihydrite phase is transformed is largely locked into the newly forming goethite phase and thus remains in the sediment column. This means that despite release of P from ferrihydrite as it undergoes remineralisation the sediments remain a sink for P, it is not re-released to the water column.

Variation of deep water phosphate through time could potentially be caused by changes in hydrothermal activity or by redistribution of nutrients. The redistribution of nutrients is controlled by a combination of the strength of the ocean circulation and the degree of biological activity. Over a glacial interglacial timescale it is the redistribution of nutrients that is the more important factor.

A potential explanation for some of the changes is changes in the flow of North Atlantic Deep Water (NADW). During the mid Pleistocene revolution (0.35-0.95 my BP) there was a change from 41ka to 100ka periodicity and formation of NADW was suppressed (Raymo et al., 1997). At this interval there was a marked decrease in the P/Fe in the Pacific (Poulton & Canfield, 2006).

The variability in dissolved phosphate in these sediments is either controlled by the Fe diagenesis occurring, or variations in the deep water phosphate. The ferrihydrite transformation data suggest that alteration to goethite occurs in the interglacial sediments. This would lead to loss of P, and increasing V/Fe and could account for the majority of the signal. It seems unlikely that variations in dissolved phosphate in the bottom water could account for all the variability observed. However it is possible that this still has an effect on the ratio.

5.5 Behaviour of vanadium on a glacial/interglacial timescale

The V oxyanion is co-precipitated by Fe oxide particles in the hydrothermal plume. The V/Fe ratio in neutrally buoyant plume particles varies from ocean to ocean and shows a strong inverse correlation with bottom water phosphate concentration due to the competition between P and V in the scavenging process by Fe (Edmonds and German, 2004). Once formed, the V/Fe in hydrothermal particles is not generally altered by subsequent adsorption/desorption (Feely et al., 1992; Edmonds & German, 2004) or by variations in the concentration of dissolved P in the SEPR region (which could be the result of either variations in the hydrothermal input, or of redistribution of nutrients (a function of biology or circulation) (Poulton & Canfield, 2006).

Metalliferous sediments could potentially record seawater variations in both dissolved P and V through time, but significant vanadium is lost during only mildly reducing conditions, compromising the sedimentary V/Fe record (Schaller et al., 2000). In addition, under oxygen depleted conditions soluble V(V) is reduced to the insoluble V(III) and can become enriched in the sediment column via diffusion in from overlying seawater and precipitation at depth (e.g. Emerson & Huested, 1991; Klinkhammer & Palmer, 1991).

The distribution of V between the different sediment phases is discussed in chapter 4.6. The majority of the V is found in the residual non reducible phase (Fig 5.3.5). This means that during the transformation of ferrihydrite to goethite and further crystalline phases the V is locked away in the sediment, making them an effective sink for vanadium. There is negative correlation between V/Fe and P/Fe, which is consistent with there being competition occurring between P and V in the scavenging of these elements by particulate Fe. Loss of P occurs during oxic transformations, while V/Fe is preferentially taken up into the goethite and non-reducible phases. Thus V becomes enriched relative to Fe in the interglacial periods.

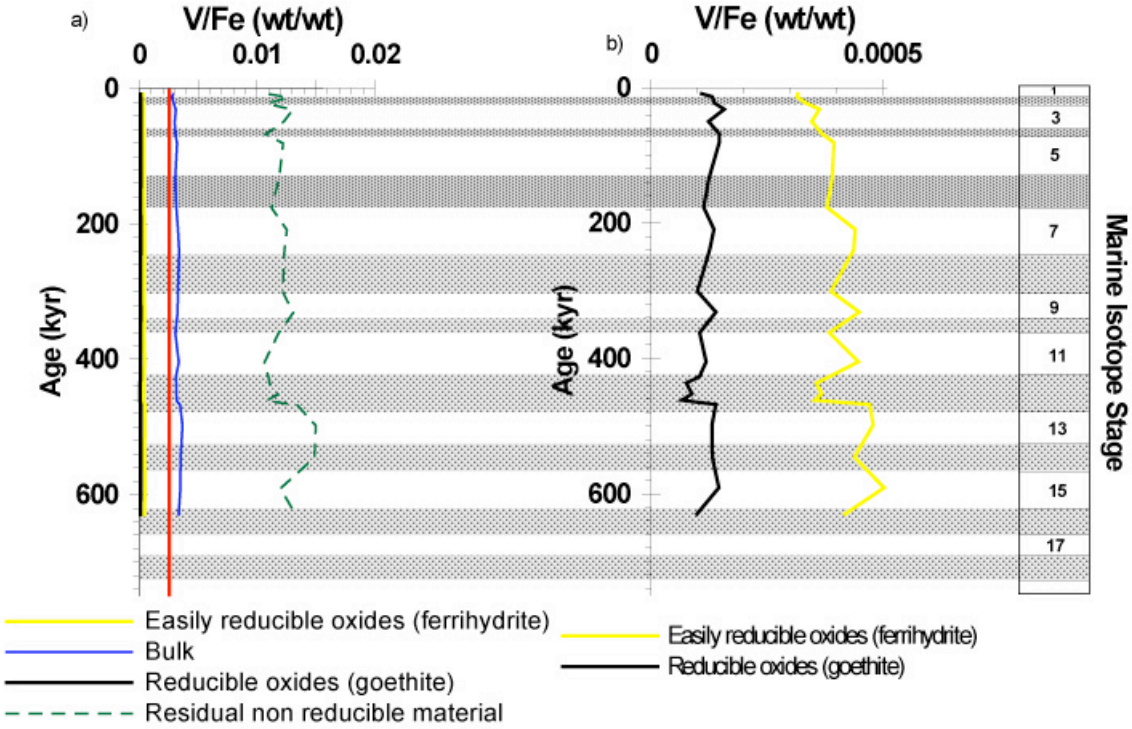

Figure 5.3.5 a) Downcore distribution of V/Fe associated with different Fe phases. The red line indicates oxyanion/Fe ratios as measured in the 13°-19°S Plume (German et al., 2002). Glacial stages are indicated by shaded boxes b) Downcore V/Fe in easily reducible and reducible phases (expanded scale)

5.6 Uranium and Molybdenum behaviour on a glacial-interglacial timescale

The downcore distribution of Mo and U and their behaviour during suboxic diagenesis is discussed in Chapter 4. It has been shown that Mn is variably enriched throughout the core compared to oxic metalliferous sediments east of the ridge axis (EXCO; Dunk, 2004).

Mo/Mn ratios are elevated in the upper part of the core (MIS1-5). Increased ratios reflect the more oxic conditions prevalent since MIS 6. The Mo/Mn peaks grow progressively larger and coincide with the onset of MIS 11, 9, 7 and 5. This suggests the onset of more oxic conditions in late Pleistocene interglacial transitions. Non-steady state paleo-redox fronts identified by the cross over of Mo/Mn and U/Fe are associated with glacial-interglacial transitions. The U/Fe and Mo/Mn records are decoupled during suboxic diagenesis.

Significant U/Fe peaks generally coincide with glacial periods indicating more reducing conditions in the interglacials. The variability of the U data appears to show a strong periodicity of approximately 100 ka, corresponding to the Milankovitch cycles. A spectral analysis is needed to fully evaluate the periodicity and significance of the data. Sequential extractions showed that the bulk of the U is associated with the amorphous ferrihydrite phase. During glacial periods, transformation of ferrihydrite to more crystalline phases is suppressed.

5.7 Mechanisms controlling the redox status of the sediments

The Fe and Mn phases and therefore the oxyanion/Fe ratios respond to redox changes in the sediment. Investigation of the transformation kinetics of ferrihydrite to goethite implies considerably more reducing behaviour in the glacial periods than the interglacial periods, which is supported by the fractionation of the P/Fe data. There are a number of different mechanisms that could control, separately or in combination, the redox status of the sediment:

(1) Changes in the overlying productivity, leading to an increased carbon rain rate to the underlying sediments. Increased organic matter in the sediments means an increase in the amount of electron donor, making the sediments more reducing at a shallower depth and increasing the rate and extent of diagenesis.
(2) Changes in the degree of sediment focussing. Increasing focussing would result in an increased rate of sedimentation, increasing the rate of burial of sedimentary components (including electron donor) and thus shallowing the redox boundary.
(3) Changes in bottom water oxygen concentration. This is a function of the strength of the deep ocean circulation and the 'age' of the deep water masses.
(4) Variability in the preservation of the deep sea carbonate component of the sediment. Decreased carbonate preservation would lead to apparent increases in the accumulation of non-carbonate phases. This is known to vary in a cyclic manner relating to glacial-interglacial changes in the system, and is driven by ocean pH and ultimately pCO_2 (Archer et al., 1994; Archer et al., 2000)

Of these explanations of changing sedimentary redox status, variability in the preservation of carbonate is unlikely to be of any significance. These sediments are deposited above the lysocline and there is no evidence in either SEM or sequential leach data that significant dissolution of carbonate has occurred. Calculation shows that the water column at this site is over saturated with respect to calcite ($\Omega_{CALCITE}$ = 1.03) and the inferred carbonate lysocline is deeper than the saturation horizon. Studies of the glacial equatorial ocean suggest that the calcite lysocline was shallower and that preservation was enhanced. Thus changes in lysocline depth are unlikely to affect sedimentation at this site.

Changes in focussing are also unlikely to be a significant cause of the variability seen in the oxyanion data. While $^{230}Th_{xs}$ calculations support the occurrence of a small degree of focussing occurring at 14°S, the focussing factor is relatively constant over the period of the last 50ka (FF=1.3 to the end of MIS 4) over a series of glacial interglacial cycles that show redox variability in the oxyanion profiles. Focussing could be a contributory factor though, as the focussing factors during the preceding extended interglacial, MIS 5, are higher by a factor of 2, and this period shows

decreased P/Fe ratios and increased partitioning of P from ferrihydrite to goethite i.e. a more reducing environment.

Decoupling the effects of changing productivity and changing bottom water [O_2] is more difficult. Changes in the strength of circulation could explain some variability. The bulk V/Fe and P/Fe ratios in core GS 7202-35 co-vary in the manner expected if they were controlled at least in part by competition in the scavenging reactions by the particulate Fe. While V is mobilised in even slightly suboxic sediments, the sequential leach data suggests that in this setting it is not lost from the sediments, but instead locked into a non-reducible phase. As shown in section 5.3, the 14^{o}S site is currently situated beneath an area of steep O_2 and dissolved Phosphate concentration gradients, therefore the changes in circulation required to have a noticeable effect on sedimentation need not be that large.

Increased productivity over the sediments would increase the delivery of organic C to the sediments, resulting in more reducing conditions. There is no evidence for this now, as C_{org} is negligible. Previous proxy studies of the LGM have posited a much higher sedimentation rate, which was inferred to be the result of an increased calcite flux, but there is dispute about the contribution of focussing to these accumulation rates. As mentioned above, certainly in these sediments focussing is an issue, but it does not appear to vary on a glacial-interglacial timescales and the exact controls are not completely understood.

5.8 Summary

The aim of this chapter was to evaluate the potential of oxyanions and trace metals associated with redox sensitive Fe and Mn for use as proxies of ocean conditions.

Sediments in the southeast Pacific are enriched in trace metals and oxyanions and the distribution of these trace elements could potentially reflect the redox status of the sediment through time.

Phosphorus is important biogeochemically as a nutrient. Hydrothermal uptake is a significant global sink. In the hydrothermal plume P/Fe initially behaves linearly. The P/Fe ratio is controlled by:

- Dissolved P in sea water (controlling initial scavenging reactions)
- Early sedimentary diagenesis (affects degree of preservation of ratio)

It has been observed that in the near field plume ratios are retained while in the far field P/Fe is depleted with respect to plume values. While dissolved P controls formation of the ratio in plume particles, diagenetic alteration in the plume and post deposition controls the degree of preservation of the ratio.

At 14^{o}S the plume is injected into a water mass of low oxygen concentration and high dissolved phosphate concentration leading to slow oxidation of the fine grained sulphides. This can explain the elevated P/Fe observed in Pacific plume particles compared to those formed in the Atlantic in fully oxic conditions (e.g. Rainbow).

The impact of diagenesis occurring in the water column can be assessed using the transformation of ferrihydrite to goethite and non reducible phases in the sediment by extrapolating the percentage transformation to the time of the deposition of sediment. In core GS7202-35 the percentage of ferrihydrite at t=0 is only 60% suggesting significant alteration has already occurred in the water column prior to deposition. In the 0.36 Ma EXCO sediment the percentage ferrihydrite at t=0 is 100% suggestion at this site there has been no alteration during plume transit. Uptake of phosphorus from sea water during sulphide oxidation is offset by release of P during these alteration recrystallisation reactions.

The trace element records indicate suboxic behaviour. However there is no electron donor left in the sediment. Organic carbon is negligible and all sulphides have already been oxidised. This suppresses further redox reactions, e.g. mobilisation of Mn to the redox boundary.

The extent to which P/Fe ratios can be used as a proxy is dependant on diagenetic mobilisation. There are three possible sinks for P released during diagenesis

- Readsorption to the oxide

- Incorporation into authigenic phases
- Association with newly formed secondary Fe phases

Any P not captured by one of these processes will escape to the overlying water column or a different sink layer within the sediment.

P/Fe in the sediment is consistent with plume values but varies on a glacial - interglacial time scale. P/Fe is higher during glacial periods suggesting that under glacial conditions Fe diagenesis is suppressed leaving the P in the ferrihydrite phase.

The V/Fe record inversely correlates with the P/Fe record. The ratio V/Fe in hydrothermal particles is generally not affected by variations in dissolved phosphate after formation. V/Fe is mobilised under even slightly suboxic conditions. The majority of the V/Fe in this sediment is partitioned into the non reducible phase and V/Fe is enhanced in interglacial periods where the most significant ferrihydrite transformation has occurred. Once incorporated into the non reducible phase the V is permanently locked away.

Mn is variably enriched throughout the core with respect to the oxic metalliferous sediment. Mo/Mn ratios are elevated in the upper core (MIS 1-5) reflecting more oxic conditions prevalent since MIS 6. Progressively larger Mo/Mn peaks coincide with the onset of MIS 11, 9, 7 and 5 suggesting that onset of more oxic conditions occurred during the late Pleistocene interglacial periods. U/Fe and Mo/Mn records are decoupled during suboxic diagenesis. Non steady state paleo-redox fronts are identified by the cross over of Mo and U/Fe and are associated with the glacial – interglacial transitions. Significant U/Fe peaks generally coincide with glacial periods indicting more reducing conditions. Sequential leach data show that the majority of the U is partitioned to the easily reducible ferrihydrite phase. However, at the horizons where the most extreme U enrichment is observed, there is also an increased degree of partitioning of U to a residual, non-reducible phase.

There is a significant change in the redox state of the sediments at most Pleistocene glacial-interglacial transitions. This could be driven by a pulse of carbon delivery to the seafloor or depletion of bottom water oxygen followed by a return to steady state

conditions. The redox sensitive oxyanions used in combination are potentially powerful paleoproxies in settings where suboxic diagenesis has compromised other proxy records.

There is negative correlation between V/Fe and P/Fe, which is consistent with there being competition occurring between P and V in the scavenging of these elements by particulate Fe in hydrothermal precipitates. While variation in P/Fe and V/Fe can be partially explained by variation in the deep water phosphate (again linking to changing circulation) affecting this scavenging, the more important process appears to be the diagenetic transformation of hydrothermally formed ferrihydrite to the more stable goethite in the sediment. Loss of P occurs during oxic transformations, while V/Fe is preferentially taken up into the goethite and non reducible phases. The degree of alteration of ferrihydrite shows a distinct behavioural change between glacial and interglacial sediments. There is little transformation during the glacial periods, resulting in high P/Fe ratios in the easily reducible Fe oxide fraction (ferrihydrite). During the interglacial periods, the sediments undergo a rate of phase transition similar to the sediments at 17^{o}S and the P/Fe ratio of the ferrihydrite fraction is lower implying oxic conditions and loss of P from this phase.

The redox status of the sediment could be controlled by changes in the overlying productivity, changes in the degree of sediment focussing, changes in bottom water oxygen concentration or variability in the preservation of the deep sea carbonate component of the sediment. Variability in the preservation of carbonate is unlikely to be of any significance, as there is no evidence for dissolution of carbonate in these sediments. Changes in focussing are also unlikely to be the sole cause of the variability seen in the oxyanion data, as while there is evidence for a significant degree of focussing occurring at 14^{o}S, the focussing factor does not appear to be variable on a glacial-interglacial timescale.

Decoupling the effects of changing productivity and changing bottom water [O_2] is more difficult as these properties are inter-related. It is likely that the changes in the redox status are the result of a combination of the two. Changes in the strength of circulation could explain some variability. The bulk V/Fe and P/Fe behave as would be expected in they were in competition during scavenging reactions by the particulate Fe.

V/Fe correlates inversely to the amount of dissolved phosphate in the bottom water. This is at least partially a function of the ocean ventilation, in a similar way to bottom water oxygen concentration. The 14°S site is currently situated beneath an area of steep [O_2] and dissolved [P] gradients, therefore the changes in circulation required to have a noticeable effect on sedimentation need not be that large. However variability in dissolved P cannot explain all the fractionation seen in the P and V sequential extractions, which require significant amount of diagenesis.

Increased productivity over the sediments would increase the delivery of organic C to the sediments, resulting in more reducing conditions. There is no evidence for this now, as C_{org} is negligible. Previous proxy studies of the LGM have posited much higher sedimentation rates, which was inferred to be the result of an increased calcite flux, but there is dispute about the contribution of focussing to these accumulation rates. As mentioned above, certainly in these sediments focussing is an issue, but it does not appear to vary on a glacial-interglacial timescales and the exact controls are not completely understood.

When used in conjunction, the oxyanions in these sediments can be used to reconstruct changes in redox status of the sediments on a glacial interglacial timescale and the degree of suboxic diagenesis that is occurring. These redox changes are a function of the ocean conditions beneath which the sediments are forming. While on their own the oxyanion distributions cannot be used to extrapolate past ocean conditions, in conjunction with other variables they form a useful tool to help explain the mechanisms operating in the past environment.

Chapter 6: Summary

The south east and equatorial Pacific play an important role in the global carbon cycle. The EEP is the location of the largest flux of carbon dioxide from the modern oceans where the equatorial undercurrent upwells. Productivity varies through the equatorial and sub tropical region, decreasing with distance from the equator. The major topographic high in the region is the East Pacific Rise (EPR).

Between 13°-19°S the EPR is the location intense hydrothermal activity (Feely et al., 1996). This venting has implications for sedimentation in the region. The main sources and gross composition of sediments are reasonably well constrained, and within 100km of the ridge axis are dominated by hydrothermal plume fall out. The south east Pacific contains the largest areal distribution of recent metalliferous sediments in the oceans. The distribution is controlled by westward flow at ~2500m depth (Reid, 1982) which transports the hydrothermal plume over significant distances (Dymond, 1981).

The ridge crest 13-19°S is beneath an area of low productivity. At the depth of the ridge crest, the water mass has circulated south to this area from the north Pacific (NPDW). In the present day Pacific, there is an oxygen minimum and nutrient maximum associated with NADW at ~2000m. It has been suggested that during the LGM this was ~500-1000m deeper (Matsumoto et al., 2002). If this is the case, then the EPR ridge crest could be exposed to a water mass with a higher nutrient and lower oxygen concentration during the last glacial period without the need for a significant change in the direction of the mid depth (~3000m) water flow (Matsumoto et al., 2002)

The GS7202 core site is located at 14°47' S, 82km west of the EPR ridge crest at a water depth of 3044m. The sediment in this core can be represented by a simple two component model of biogenic carbonate diluted with a large metalliferous hydrothermal input. The lithogenic input is negligible (<1.5% of the bulk). The water column at site GS 7202-35 is saturated at depth with respect to calcite ($\Omega_{CALCITE}$ = 1.03) and the bulk of the sediment is calcium carbonate (58-72%). More intensive hydrothermal input, occurring while the core location was closer to the ridge axis, is apparent by the increased dilution and thus greater hydrothermal input (up to 40%) in

the deeper parts of the core. The hydrothermal component of the core consists predominantly of x-ray amorphous Fe and Mn (hydr)oxides. There is only a minor clay component (<1%) and no measurable pyrite despite S concentrations that are elevated above background pelagic sedimentation values throughout the core.

80 km west of the ridge crest, the particles forming in the neutrally buoyant hydrothermal plume are predominantly reactive Fe (hydr)oxides, although particles closer to the ridge axis (~25km) are a mixture of Fe oxide and sulphide/sulphur mineral phases (Feely et al, 1996).

In the sediment the reactive Fe (hydr)oxides, delivered as ferrihydrite, are transformed to more crystalline goethite and other non-reducible phases (Poulton & Canfield, 2005). The degree to which this transformation is occurring can be assessed in part by assuming that the reaction obeys a 1st order kinetic model (Poulton & Canfield, 2006) Two distinct behaviours can be observed in this sediment. The ferrihydrite deposited during interglacial periods is slowly transformed to goethite (estimated half life – 1.3Ma). Other Pleistocene sediments at 19^{o}S show similar behaviour (Figure 4.4.4).

There is no first order relationship in the sediments deposited in glacial periods. There appears to be an excess of ferrihydrite present relative to the amount of more crystalline phases down core. Either ferrihydrite transformations under glacial conditions are somehow impeded (perhaps as the result of a distinct change in sediment redox status under glacial conditions) or the excess is the result of sulphide oxidation. It has been hypothesized that the accumulation of sulphides in sediments is enhanced during glacial periods. Oxidation of this sulphide material would result in the formation of ferrihydrite in early diagenesis independent of the ferrihydrite sourced from the hydrothermal plume.

As they are precipitated from the hydrothermal plume Fe (hydr)oxides can act as scavengers of trace elements dissolved in the ambient seawater, (e.g. U, Mo, P, V, As) (Edmonds and German, 2004; Feely et al., 1996; German et al., 1990; Trocine & Trefry, 1988). Potentially, these elements could therefore be a record of past ocean conditions (Edmonds & German, 2004; Feely et al., 1996). However, they are subject

to chemical alteration during transport and post-deposition in the sediment to varying degrees. (Poulton & Canfield, 2006). These reactions can perturb any sediment record (Schaller et al., 2000). The situation is further complicated in areas of low sediment accumulation, as when this is the case bioturbation and lateral redistribution of sediment can smooth the record.

Both Fe and Mn can be used as tracers of hydrothermal input to the sediment from the overlying plume. These sediments show a significant enrichment of both Fe and Mn. Plume derived Fe and Mn (hydr)oxides are subject to alteration both in the aging neutrally buoyant plume and after sedimentary deposition. Variability in the Fe/Mn ratio is the result of either fractionation during early sedimentary diagenesis or variation at source. The Fe/Mn range in these sediments (2.12-3.7) is consistent with other sediments from the area, but the mean value is low. There appears to be an excess of Mn with respect to Fe compared to oxic metalliferous sediments in the region. Sequential leaches have shown that 70-80% of the Mn is associated with the operationally defined reactive Fe-Oxide fraction, which is inferred to include Mn(II), carbonate and sorbed Mn(II), which can be derived from early diagenesis in the sediment, or reactions of the Mn oxides with sulphides deposited from the plume. (Aller & Rude, 1988; Schippers & Jorgensen, 2001). There must be a significant amount of Mn cycling is occurring. Precipitation of Mn oxide phases requires that the sediment be close to oxic in nature. The active redox zone in these sediments must have remained deep enough below the surface of the sediment to ensure a minimum loss of Mn into the overlying water throughout the sediment record.

Mn cycling in the sediment has a significant effect on its Mo content if the sediment is suboxic. While the molybdenate oxyanion has a strong affinity for manganese oxides, during early diagenesis the Mo is completely lost from the sediment. The Mo/Mn ratio in oxic sediments and ferromanganese deposits is relatively constant (Mo/Mn = 0.002; Shimmield & Price, 1986). The variable Mo/Mn record at the GS 7202 site confirms significant cycling of the Mn in the sediment when core was close to the axis (Figure 3.7.1; Figure 3.7.3b). This is particularly apparent in glacial periods, where there is no Mo remaining in the sediment. In relatively more recent sediment in the upper sections of the core (MIS 1-5), the Mo/Mn ratios are higher. This is consistent with a shift to more oxic conditions. This could be the result of a combination of more oxidised

hydrothermal inputs as the core is further from the ridge crest, an increase in the ventilation of the Pacific and/or less carbon export occurring since the mid-Pleistocene (Venuti et al., 2007).

Fe and Mn (hydr)oxides also scavenge oxyanions of P, V and U. As mentioned previously, the trace element record in the sediment could potentially reflect past ocean chemistry. The P/Fe ratios in the hydrothermal plume have been shown to reflect deep water phosphate concentrations (Feely et al., 1996). However the P/Fe ratios in the sediment at the GS7202 site are less than those observed in particles in the overlying plume (Figure 4.6.2). At 19^{o}S the P/Fe ratio has been shown to decrease as ferrihydrite in the sediment is transformed to goethite in oxic diagenesis (Poulton & Canfield, 2006). However at 14^{o}47'S the amount of P associated with the reactive Fe is highly variable downcore (Figure 4.6.3). The glacial layers of the sediment have high P/Fe ratios. A significant proportion of the P is associated with the highly reactive phase. It has been hypothesised that there is enhanced accumulation of sulphides. Oxidation of Fe-sulphides precipitated into the sediment in glacial periods to ferrihydrite provides a sink for diagenetically mobilised P, the result of which would be increased P/Fe in the glacial periods.

Both plume particle and sediment V/Fe ratios are inversely related to bottom water oxygen concentrations. As such, is has been suggested they are a potential proxy for deepwater phosphate concentrations (Edmonds & German, 2004; Feely et al., 1996). This is a function of ocean ventilation in a similar way to dissolved oxygen. The 14^{o}47'S site is currently situated beneath a water mass with steep oxygen and dissolved phosphate concentration gradients. This means that the changes in circulation required to have a noticeable effect on sedimentation need not be that large.

Variability in the dissolved phosphate concentrations however cannot explain all the fractionation shown in by the sequential leaches of these sediments. The sequential leach data indicate that the majority of the V is bound to a non reducible phase, with only a small (relatively constant) percentage associated with the amorphous ferrihydrite phases (Figure 4.6.5). This suggests there has been a significant degree of Fe cycling, and the majority of the V can be found in the more crystalline Fe phases. The V/Fe in the ferrihydrite and goethite phases is considerably lower than that of the

plume, while the ratio in the non reducible phase is greatly in excess of plume values i.e. V that has been discriminated against in the amorphous phase remains in the sediment column associated with the non reducible phase. This enrichment relative to Fe increases with increasing depth (i.e. increasing sediment age and decreasing distance from the axis at time of deposition).

High P/Fe and low V/Fe coincide with glacial periods and lower P/Fe and higher V/Fe ratios occur during the Holocene and other interglacials. While the significant degree of suboxic cycling of Fe and Mn occurring in these sediments has led to partitioning of trace metals within the sediment, we hypothesize that the primary plume signature is still retained in the sediment recording elevated phosphate during glacial periods.

Peaks in uranium concentration are common in sediments in the EPR region between 10^{o} and 20^{o}S (Schaller et al., 2000; Shimmield & Price, 1988). A number of explanations have been put forth for these enrichments, including scavenging from the hydrothermal plume (Shimmield & Price, 1988) and post-depositional subsurface flow of uranium rich fluids (Rydell et al., 1974; Schaller et al., 2000). The enrichment seen in these sediments is particularly high (~30ppm maximum). Previously published $^{234}U/^{238}U$ data (Rydell et al., 1974) indicate the uranium is of seawater origin.

In oxic and ridge flank hydrothermal sediments the U/Fe ratio is both low and relatively constant (U/Fe = 0.3x10-4, Mills et al., 1994). Core U/Fe ratios suggest relatively oxic conditions were prevalent during MIS 5, 7 and 9 (Figure 3.7.3). In the glacial sections of the 15^{o}S core the U/Fe is significantly greater than this value. The most significant enrichment occurs at ~443ka in MIS 12. This coincides with a significant minimum in the reconstructed ventilation of the Pacific at ~450ka (Venuti et al., 2007).

The majority of the U is associated with the amorphous ferrihydrite phase (Figure 4.6.6). There is still a significant fraction in the goethite and non reducible phases in the top 5 m of the core, but below this horizon, where there is the greatest U enrichment, the fraction of U into phases other than ferrihydrite reduces to practically 0. However, at horizons where extreme U enrichment is observed there is increased partitioning of the U to the residual non reducible phase.

Accumulation of a significant quantity of authigenic U only occurs in sediments where the redox interface is within cm of the surface (Morford et al., 2005). In order to retain the Mn(II) in this core the thickness of the oxic layer at the sediment would have to be greater than this. A more likely explanation of the U enrichment observed is input of seawater U associated with plume sulphide particles (German et al., 2002). Oxidation of the sulphides during and post burial in the sediment would produce U(VI) and Mn(II), which would then be retained by the secondary phases formed. The U/Th disequilibrium observed by Rydell (Rydell et al., 1974) is inferred to arise because U is mobilised during sulphide oxidation and reincorporated into ferrihydrite phases. The subsurface U peaks therefore record periods of low bottom water O content and high U input associated with plume sulphides.

In summary, as the site at 14^{o}47'S has moved increasing distances from the ridge axis over the last 740ka, it has seen variable and decreasing delivery of sulphide material from the hydrothermal plume. The general trend of decreasing supply of sulphide with time is modulated by decreased oxygen levels during glacial periods. During the periods of lower oxygen concentrations, the oxidation of sulphide material at the seafloor is slower. Suboxic cycling of Mn and Fe are also enhanced and there is increased preservation of U in the sediment. A further result of this change in the ventilation of the ocean is higher glacial bottom water phosphate levels. This can be seen in the combined P/Fe and V/Fe records.

The main aim of this work was to understand the mechanisms controlling the distribution of these trace elements and oxyanions in southeast Pacific sediments and to use oxyanion distributions and Fe speciation to establish variability in the redox status of the sediment through time. The mechanisms controlling the redox conditions were identified and the redox relationships of the oxyanions investigated to see if this quantity could be used as proxy for past ocean conditions.

This was accomplished by establishing a complete picture of the sedimentary relationships in the core. Bulk sediment composition and accumulation were investigated in the context of the regional setting, and an age model generated for sediment accumulation. A series of sequential extractions allowed investigation of the

speciation of Fe and Mn and the fractionation of the trace elements of interest between different phases in the core and to evaluate the current and previous redox status throughout the core.

It was found that when used in conjunction, the trace element record in ridge crest metalliferous sediments can be used to reconstruct past bottom water oxygen on a glacial-interglacial timescale, in a region where paleoceanographic records are limited.

Future work

Further work is required on the kinetic model used to investigate the rate of ferrihydrite alteration .The sequential extractions in this work were only carried out on a small subset of samples so data resolution could be greatly increased. There were some ambiguities in the carbonate sequential leach data. Further extractions including a preliminary leach of the carbonate phase prior to the leach of the reactive Fe phase and more detailed crystallographic analysis are required to explain the ambiguities seen

A number of published sedimentary records from the southern EPR exist which exhibit subsurface uranium peaks that are largely undated. This work suggests the possibility these peaks are relicts of a lower oxygen glacial ocean. Detailed further work is required to test this hypothesis. The sediment accumulation at each site needs to be assessed and the age of the uranium enriched horizons established. Detailed analysis of the phase association of Fe and P has been carried out at DSDP site 92-158 at 19^{o}S (Poulton & Canfield, 2006) but there is to date no uranium data for this site.

.

Appendix 1: Geochemical data

Table A1.1: Major and minor elements as measured by XRF. Major elements were measured from XRF Beads. Minor elements were measured from XRF pellets. Age is derived from the $d^{18}O$ age model.

Sample ID	Age	Depth	Major elements								Minor elements								
			SiO2	Fe2O3	MnO	MgO	CaO	K2O	Na2O	P2O5	Cr	V	Ni	Cu	Zn	As	Ba	U	Mo
	(ka)	cm	(%)	(%)	(%)	(%)	(%)	(%)	(%)	(%)	(ppm)	(ppm)	(ppm)	(ppm)	(ppm)	(ppm)	(ppm)	(ppm)	(ppm)
SLTTC1	4.5	5.3	3.0	9.0	2.2	0.58	41.6	0.19	2.7	0.69	17.2	247	129	309	122	286	1290	5.0	8.6
SLTTC3	13.3	15.5	2.6	7.3	1.9	0.50	43.5	0.20	2.5	0.62	12.1	200	108	210	95	232	1100	7.1	7.0
SLTTC4	18.3	20.5	3.2	9.1	2.3	0.59	40.0	0.23	2.8	0.77	16.7	236	131	297	119	302	1220	6.7	8.5
SLTTC5	22.8	25.5	2.3	6.9	2.3	0.52	43.1	0.20	2.8	0.53	6.0	192	129	198	90	207	1260	4.8	10.5
SLTTC6	27.3	30.5	2.9	8.6	2.8	0.51	41.9	0.21	2.3	0.71	6.8	255	155	261	111	277	1360	5.0	15.0
SLTTC7	31.8	35.5	3.3	9.5	3.1	0.53	40.0	0.26	2.2	0.92	6.3	286	177	306	125	339	1320	8.2	19.2
SLTTC8	36.3	40.5	2.7	7.9	2.6	0.56	41.5	0.28	3.0	0.80	7.9	230	145	246	105	279	1210	8.5	15.8
SLTTC9	40.8	45.5	2.5	7.2	2.3	0.50	42.2	0.22	2.5	0.63	3.6	212	109	210	94	227	1190	8.2	10.8
SLTTC10	45.3	50.5	2.5	6.9	2.2	0.42	41.9	0.20	2.0	0.62	6.2	208	115	216	95	231	1150	8.3	11.7
SLTTC11	49.8	55.5	2.6	7.5	2.4	0.42	43.2	0.20	1.8	0.66	7.8	220	116	221	97	234	1280	8.1	11.2
SLTTC12	54.4	60.5	2.7	8.3	2.5	0.48	41.6	0.24	2.1	0.79	26.4	253	141	251	107	273	1290	8.3	14.2
SLTTC13	58.9	65.5	3.0	9.2	2.9	0.52	40.4	0.29	2.4	0.96	8.5	264	167	299	123	332	1290	8.2	19.2
SLTTC14	63.4	70.5	3.0	9.1	3.0	0.49	41.1	0.25	2.1	0.87	7.7	278	180	297	125	296	1400	7.4	21.7
SLTTC15	67.9	75.5	2.8	8.8	2.9	0.48	41.9	0.21	1.9	0.76	7.7	268	178	296	124	279	1480	7.3	21.7
SLTTC16	72.4	80.5	2.7	8.7	2.7	0.48	41.5	0.19	2.0	0.66	9.2	269	164	281	115	256	1500	4.7	19.7
SLTTC17	76.9	85.5	2.7	8.8	2.7	0.50	40.7	0.19	2.1	0.62	3.0	285	169	296	119	252	1630	4.9	22.8
SLTTC18	81.4	90.5	2.7	9.1	2.9	0.48	43.3	0.15	1.9	0.57	4.5	284	166	317	122	250	1700	3.7	24.1
SLTTC19	85.9	95.5	2.8	9.3	3.1	0.54	40.4	0.18	2.3	0.60	4.8	313	190	361	136	266	1760	5.7	29.7
SLTTC20	90.4	100.5	2.7	8.8	3.0	0.49	40.7	0.17	2.0	0.58	7.1	275	182	340	131	251	1510	5	30.8
SLTTC23	103.9	115.5	2.7	9.1	2.9	0.51	41.9	0.18	2.1	0.62	5.3	273	163	334	128	256	1460	5.2	28.1
SLTTC24	108.4	120.5	3.0	10.2	3.4	0.57	39.7	0.19	2.2	0.65	5.0	333	204	415	149	285	1840	5.4	39.0
SLTTC25	113.0	125.5	2.8	9.2	3.1	0.55	40.9	0.17	2.2	0.57	4.4	300	193	375	137	258	1810	4.1	40.5
SLTTC27	121.9	135.5	2.9	8.7	2.7	0.54	41.6	0.16	2.2	0.51	3.0	282	198	334	125	236	1670	3.6	33.9
SLTTC28	126.0	140.5	3.3	10.8	3.2	0.68	52.2	0.18	2.7	0.63	0.8	260	165	312	122	235	1440	4.0	23.7
SLTTC29	130.0	145.5	2.8	9.2	2.6	0.52	41.6	0.16	2.0	0.57	8.0	282	156	305	124	528	1400	3.5	17.4
SLTTC31	138.2	155.5	2.6	8.2	2.5	0.48	42.4	0.21	2.1	0.72	2.4	240	138	241	107	259	1110	8.3	7.1
SLTPC5	140.2	158	2.4	7.4	2.3	0.46	40.6	0.20	2.5	0.69	5.0	263	155	258	113	338	1280	11.3	18.5
SLTPC7	148.3	168	2.8	8.9	2.7	0.49	38.6	0.32	2.8	1.16	8.1	263	165	284	121	378	1230	12.6	7.9

Table A1.1: Continued: Major and minor elements as measured by XRF. Major elements were measured from XRF Beads. Minor elements were measured from XRF pellets. Age is derived from the $d^{18}O$ age model.

			Major elements								Minor elements								
Sample ID	Age	Depth	SiO2	Fe2O3	MnO	MgO	CaO	K2O	Na2O	P2O5	Cr	V	Ni	Cu	Zn	As	Ba	U	Mo
	(ka)	cm	(%)	(%)	(%)	(%)	(%)	(%)	(%)	(%)	(ppm)	(ppm)	(ppm)	(ppm)	(ppm)	(ppm)	(ppm)	(ppm)	(ppm)
SLTPC9	156.5	178	2.4	7.4	2.5	0.42	34.7	0.26	2.4	0.92	6.2	265	162	264	117	341	1270	11.9	5.7
SLTPC11	164.6	188	2.3	7.0	2.5	0.43	40.9	0.19	2.4	0.62	4.7	225	147	215	102	229	1330	8.2	4.6
SLTPC14	176.8	203	2.3	6.8	2.6	0.42	41.6	0.14	2.2	0.49	8.7	217	152	227	102	197	1360	5.7	3.6
SLTPC16	184.9	213	2.3	7.1	2.6	0.43	40.8	0.17	2.3	0.59	2.5	232	148	244	102	225	1400	4.8	2.7
SLTPC20	197.1	233	2.8	8.5	3.1	0.50	40.6	0.17	2.3	0.59	1.4	298	196	386	125	256	1770	4.3	5.1
SLTPC22	203.3	243	2.5	7.9	3.0	0.48	39.1	0.16	2.5	0.57	2.1	271	180	386	126	255	1370	4.5	5.4
SLTPC24	209.4	253	2.6	7.8	2.9	0.51	40.0	0.17	2.6	0.56	2.0	263	169	372	124	237	1290	3.6	4.5
SLTPC26	215.5	263	2.5	7.5	2.9	0.50	40.0	0.17	2.6	0.57	5.5	257	172	355	122	239	1430	4.3	4.5
SLTPC28	221.6	273	2.4	7.8	3.1	0.52	38.2	0.22	2.8	0.77	2.1	264	195	335	120	283	1340	6.3	7.2
SLTPC30	227.7	283	2.3	7.6	3.2	0.47	42.2	0.16	2.1	0.53	1.9	271	202	314	112	227	1370	3.5	7.4
SLTPC32	233.8	293	2.5	8.7	2.9	0.47	38.5	0.17	2.5	0.62	2.5	321	183	420	138	304	1330	3.5	5.3
SLTPC34	239.9	303	3.5	9.8	3.0	0.49	37.8	0.20	2.6	0.77	4.8	368	203	493	165	361	1320	8.0	4.9
SLTPC36	246.0	313	2.7	8.8	2.6	0.55	55.0	0.18	2.9	0.65	6.7	195	136	229	88	202	1110	11.3	0.5
SLTPC40	258.2	333	2.4	6.1	2.1	0.40	43.9	0.20	2.1	0.63	9.9	179	109	183	86	201	1120	9.9	0.4
SLTPC52	294.8	393	2.5	8.1	3.3	0.43	40.1	0.18	2.4	0.65	0.2	287	221	357	127	260	1380	7.6	3.5
SLTPC54	300.9	403	2.5	7.8	2.9	0.42	40.1	0.18	2.3	0.63	4.6	271	165	296	119	246	1350	6.6	1.5
SLTPC58	313.1	423	2.7	8.8	3.0	0.46	38.8	0.22	2.6	0.80	5.1	329	184	393	133	305	1380	8.6	2.4
SLTPC60	319.2	433	2.5	8.0	2.7	0.42	41.9	0.16	2.0	0.53	2.1	250	183	324	115	223	1200	4.0	2.5
SLTPC62	325.3	443	2.4	7.9	2.9	0.42	39.9	0.17	2.4	0.59	6.5	268	180	354	123	250	1160	5.8	4.9
SLTPC64	331.4	453	3.1	10.8	3.0	0.48	35.9	0.26	2.7	1.02	11.0	384	175	424	152	384	1120	7.0	0.5
SLTPC66	337.5	463	1.5	4.5	1.4	0.22	26.8	0.11	1.5	0.41	8.9	287	146	275	118	250	916	3.8	0.8
SLTPC68	343.6	473	2.2	7.1	2.5	0.39	41.4	0.19	2.4	0.71	5.1	246	166	262	103	245	1000	6.6	1.6
SLTPC70	349.7	483	2.6	7.9	2.9	0.47	40.7	0.26	2.5	0.89	7.5	250	166	251	110	294	998	10.4	0.0
SLTPC73	358.9	498	2.6	7.4	2.5	0.40	40.4	0.24	2.3	0.87	3.5	222	168	281	103	280	989	12.9	0.9
SLTPC75	365.1	508	3.1	9.6	3.3	0.45	39.1	0.27	2.3	1.08	5.6	279	226	379	132	356	1250	14.7	1.7

Table A1.1: Continued: Major and minor elements as measured by XRF. Major elements were measured from XRF Beads. Minor elements were measured from XRF pellets. Age is derived from the $d^{18}O$ age model

			Major elements								Minor elements								
Sample ID	Age	Depth	SiO2	Fe2O3	MnO	MgO	CaO	K2O	Na2O	P2O5	Cr	V	Ni	Cu	Zn	As	Ba	U	Mo
	(ka)	cm	(%)	(%)	(%)	(%)	(%)	(%)	(%)	(%)	(ppm)	(ppm)	(ppm)	(ppm)	(ppm)	(ppm)	(ppm)	(ppm)	(ppm)
SLTPC77	371.2	518	3.0	9.4	3.8	0.49	37.4	0.25	2.6	0.92	9.0	306	254	362	145	336	1400	10.7	2.3
SLTPC80	380.4	533	3.0	9.2	3.4	0.45	37.7	0.19	2.4	0.70	8.6	310	204	374	148	292	1450	7.9	1.6
SLTPC83	389.6	548	3.9	12.7	5.1	0.56	32.0	0.18	2.7	0.70	10.4	454	294	626	261	406	1820	7.6	4.4
SLTPC85	395.7	558	3.5	11.4	4.7	0.54	33.3	0.18	2.7	0.67	7.6	406	249	537	212	358	1620	8.5	3.0
SLTPC94	423.8	603	2.5	7.6	2.6	0.41	40.4	0.25	2.4	0.94	5.9	250	156	243	111	322	1010	13.3	0.8
SLTPC98	436.5	623	2.7	8.1	2.9	0.43	41.2	0.24	2.2	0.88	6.2	264	164	267	119	302	1020	16.8	0.6
SLTPC99	439.6	628	3.0	8.9	3.3	0.49	39.6	0.34	2.5	1.21	9.5	287	183	298	130	393	1120	27.9	0.8
SLTPC101	445.9	638	2.7	7.7	2.8	0.44	39.0	0.29	2.6	1.04	4.9	249	162	262	115	338	990	26.2	0.1
SLTPC105	458.6	658	2.6	7.7	2.9	0.43	41.1	0.24	2.2	0.83	4.4	244	159	265	112	277	1070	12.5	1.1
SLTPC107	464.9	668	2.9	9.1	3.6	0.45	37.3	0.23	2.5	0.86	3.0	317	280	430	152	359	1230	14.0	1.8
SLTPC114	493.0	703	3.6	12.2	4.3	0.54	33.6	0.21	2.7	0.90	12.3	440	236	543	199	438	1310	14.7	2.7
SLTPC120	524.7	733	3.3	10.9	3.8	0.51	34.9	0.25	2.7	1.03	8.2	391	205	447	173	437	1170	16.1	1.5
SLTPC125	551.0	758	2.8	9.2	3.5	0.47	37.7	0.23	2.6	0.95	8.7	323	188	342	139	359	1220	13.6	0.2
SLTPC129	571.7	778	3.3	11.4	4.7	0.52	34.4	0.21	2.5	0.87	8.3	425	283	524	191	433	1520	14.0	3.8
SLTPC130	575.6	783	3.4	11.4	4.8	0.55	37.8	0.19	2.3	0.78	15.0	386	230	487	184	379	1520	11.9	3.6
SLTPC135	595.0	808	3.0	9.6	4.0	0.51	36.6	0.23	2.7	0.86	11.5	332	216	395	152	376	1330	15.5	4.1

Table A1.2 Major elements as measured by ICP-AES. Age is derived from the $d^{18}O$ age model

Sample ID	Depth (cm)	Age (ka)	Ti	Al	Mg	K	P	Fe	Mn	Ca
			wt %	wt %	wt %	wt %	wt %	wt %	wt %	wt %
SLTTC2	9.8	8.9	0.006	0.07	0.36	0.16	0.28	5.35	1.69	29.9
SLTTC3	15.5	13.3	0.005	0.06	0.33	0.14	0.27	5.04	1.41	29.5
SLTTC5	25.5	22.8	0.006	0.07	0.34	0.14	0.25	5.02	1.72	30.2
SLTTC7	35.5	31.8	0.006	0.07	0.42	0.24	0.40	6.43	2.18	27.5
SLTTC11	55.5	49.8	0.006	0.07	0.32	0.17	0.30	5.39	1.76	30.3
SLTTC15	75.5	67.9	0.007	0.07	0.34	0.18	0.34	6.13	2.13	29.3
SLTTC18	90.5	81.4	0.007	0.08	0.34	0.13	0.25	6.19	2.09	29.4
SLTPC4	153	133.1	0.008	0.09	0.39	0.19	0.37	6.95	2.11	27.7
SLTPC14	203	176.8	0.007	0.07	0.31	0.13	0.22	5.13	2.01	30.1
SLTPC24	253	209.4	0.009	0.11	0.37	0.15	0.26	5.74	2.27	28.5
SLTPC34	303	239.9	0.006	0.06	0.39	0.19	0.39	7.92	2.67	25.9
SLTPC54	403	300.9	0.006	0.07	0.32	0.16	0.29	5.85	2.31	29.1
SLTPC64	453	331.4	0.005	0.05	0.37	0.23	0.49	8.15	2.43	26.4
SLTPC74	503	362.0	0.006	0.08	0.31	0.23	0.47	6.09	2.07	28.9
SLTPC88	573	404.9	0.006	0.06	0.33	0.12	0.24	5.87	2.32	29.3
SLTPC95	608	427.0	0.006	0.06	0.31	0.20	0.42	5.30	1.92	30.5
SLTPC98	623	436.5	0.006	0.06	0.32	0.20	0.41	5.80	2.20	29.1
SLTPC103	648	452.3	0.006	0.06	0.33	0.21	0.42	5.94	2.22	29.7
SLTPC106	663	461.7	0.006	0.07	0.31	0.21	0.44	5.97	2.27	28.5
SLTPC108	673	468.1	0.009	0.09	0.39	0.20	0.40	8.18	3.81	25.1
SLTPC115	708	498.3	0.008	0.07	0.37	0.16	0.36	8.32	3.26	26.3
SLTPC124	753	545.8	0.008	0.07	0.36	0.22	0.49	7.34	2.92	26.8
SLTPC134	803	591.1	0.008	0.08	0.38	0.20	0.44	7.42	3.14	28.1
SLTPC144	853	630.0	0.007	0.07	0.34	0.21	0.48	6.88	2.47	28.0

Table A1.3: Minor elements as measured by ICP-AES. Age is derived from the $d^{18}O$ age model

Sample ID	Depth (cm)	Age (ka)	Cr	V	Ni	Cu	Zn	As	Ba	Sr
			ppm	ppm	ppm	ppm	ppm	ppm	ppm	ppm
SLTTC2	9.75	8.9	8.1	153	101	190	93.6	84.1	870	1220
SLTTC3	15.5	13.3	8.9	141	79	179	89.4	77.5	769	1180
SLTTC5	25.5	22.8	7.1	148	104	177	88.1	78.9	873	1220
SLTTC7	35.5	31.8	7.8	199	121	242	110.4	116.1	891	1230
SLTTC11	55.5	49.8	5.5	163	87	195	93.8	93.0	844	1270
SLTTC15	75.5	67.9	4.8	189	127	236	108.7	85.6	957	1260
SLTTC18	90.5	81.4	4.4	199	118	256	109.7	90.3	1060	1240
SLTPC4	153	133.1	5.4	212	123	256	118.9	118.1	846	1210
SLTPC14	203	176.8	4.0	162	115	195	96.8	69.6	899	1320
SLTPC24	253	209.4	5.0	189	105	266	109.9	86.4	863	1260
SLTPC34	303	239.9	7.5	268	119	348	140.4	122.6	863	1210
SLTPC54	403	300.9	5.5	192	125	249	108.9	90.6	865	1370
SLTPC64	453	331.4	8.7	266	123	340	136.0	134.6	724	1280
SLTPC74	503	362.0	7.8	187	120	228	132.6	115.9	768	1410
SLTPC88	573	404.9	6.5	197	134	249	115.7	85.1	792	1350
SLTPC95	608	427.0	7.1	165	105	188	93.8	91.0	644	1420
SLTPC98	623	436.5	6.8	183	117	215	104.9	100.9	668	1420
SLTPC103	648	452.3	5.8	188	134	232	110.4	106.9	704	1440
SLTPC106	663	461.7	6.3	190	119	236	106.9	115.2	724	1410
SLTPC108	673	468.1	5.9	285	215	360	153.2	124.7	1020	1450
SLTPC115	708	498.3	5.9	306	147	364	154.1	129.3	802	1350
SLTPC124	753	545.8	7.0	258	144	294	130.1	138.3	821	1350
SLTPC134	803	591.1	7.0	259	165	316	133.2	133.3	926	1410
SLTPC144	853	630.0	6.2	231	96	221	119.2	139.4	704	1340

Table A1.4: % Inorganic Carbon (IC) measured by coulometry % $CaCO_3$ is calculated from %IC assuming all IC is derived from $CaCO_3$. Age is derived from the $d^{18}O$ age model

Sample ID	Depth (cm)	Age (ka)	%IC	%CaCO3
SLTTC 2	9.8	8.6	8.6	71.4
SLTTC 2	9.8	8.6	8.5	71.1
SLTTC 4	20.5	18.3	8.7	72.5
SLTTC 6	30.5	27.3	8.1	67.5
SLTTC 6	30.5	27.3	8.0	66.3
SLTTC 8	40.5	36.3	8.7	72.7
SLTTC 8	40.5	36.3	8.7	72.5
SLTTC 10	50.5	45.3	9.1	75.9
SLTTC 11	55.5	49.8	9.1	76.1
SLTTC 12	60.5	54.4	8.9	74.2
SLTTC 14	70.5	63.4	8.7	72.5
SLTTC 14	70.5	63.4	8.6	72.1
SLTTC 16	80.5	72.4	8.7	72.5
SLTTC 17	85.5	76.9	8.7	72.7
SLTTC 18	90.5	81.4	8.8	73.1
SLTTC 18	90.5	81.4	8.8	73.6
SLTTC 21	105.5	94.9	8.4	70.4
SLTTC 22	110.5	99.4	8.6	71.8
SLTTC 22	110.5	99.4	8.5	70.5
SLTTC 23	115.5	103.9	8.5	71.1
SLTTC 25	125.5	113.0	8.6	71.9
SLTPC 1	138.0	123.9	8.7	72.5
SLTPC 1	138.0	123.9	8.7	72.2
SLTTC 28	140.5	126.0	8.7	72.8
SLTPC 2	143.0	128.0	8.6	71.9

Sample ID	Depth (cm)	Age (ka)	%IC	%CaCO3
SLTPC 3	148	132.1	8.3	69.3
SLTPC 3	148	132.1	8.3	69.5
SLTPC 5	158	140.2	8.8	73.3
SLTPC 7	168	148.3	8.2	68.3
SLTPC 9	178	156.5	8.4	70.2
SLTPC 9	178	156.5	8.4	70.2
SLTPC 10	183	160.5	8.5	70.6
SLTPC 12	193	168.7	9.2	76.5
SLTPC 14	203	176.8	9.0	75.1
SLTPC 15	208	180.9	8.5	71.1
SLTPC 16	213	184.9	8.9	73.9
SLTPC 17	218	188.0	8.8	73.4
SLTPC 18	223	191.0	8.7	72.2
SLTPC 19	228	194.1	8.7	72.6
SLTPC 20	233	197.1	8.5	70.7
SLTPC 21	238	200.2	8.3	69.2
SLTPC 21	238	203.3	8.3	68.9
SLTPC 22	243	203.3	8.5	70.7
SLTPC 23	248	206.3	8.1	67.4
SLTPC 25	258	212.4	8.5	70.5
SLTPC 25	258	212.4	8.7	72.8
SLTPC 27	268	218.5	8.5	70.8
SLTPC 28	273	221.6	8.7	72.4
SLTPC 30	283	227.7	7.8	65.3
SLTPC 31	288	230.7	8.5	70.5

Sample ID	Depth (cm)	Age (ka)	%IC	%CaCO3
SLTPC 32	293	233.8	8.5	71.1
SLTPC 33	298	236.8	7.9	65.9
SLTPC 34	303	239.9	8.2	68.4
SLTPC 35	308	242.9	8.7	72.4
SLTPC 37	318	249.0	9.2	76.7
SLTPC 38	323	252.1	9.1	76.0
SLTPC 39	328	255.1	9.3	77.5
SLTPC 40	333	258.2	9.2	76.4
SLTPC 42	343	264.3	9.0	75.0
SLTPC 43	348	267.3	8.2	68.3
SLTPC 43	348	267.3	8.1	67.8
SLTPC 45	358	273.4	8.2	68.0
SLTPC 45	358	273.4	8.1	67.8
SLTPC 45	358	273.4	8.1	67.9
SLTPC 46	363	276.5	7.8	65.1
SLTPC 49	378	285.6	8.2	68.5
SLTPC 51	388	291.7	8.4	70.0
SLTPC 52	393	294.8	8.2	68.5
SLTPC 53	398	297.8	8.1	67.5
SLTPC 54	403	300.9	8.8	73.0
SLTPC 57	418	310.0	8.4	70.0
SLTPC 58	423	313.1	8.6	72.0
SLTPC 58	423	313.1	8.4	70.3
SLTPC 60	433	319.2	8.7	72.5
SLTPC 60	433	319.2	8.7	72.3

Table A1.4 Continued

Sample ID	Depth (cm)	Age (ka)	%IC	%CaCO3
SLTPC 61	438	322.2	8.9	73.9
SLTPC 62	443	325.3	8.7	72.8
SLTPC 63	448	328.3	8.1	67.8
SLTPC 63	448	328.3	8.0	66.7
SLTPC 65	458	334.4	8.4	69.8
SLTPC 65	458	334.4	8.4	69.7
SLTPC 66	463	337.5	8.8	73.3
SLTPC 67	468	340.5	8.7	72.3
SLTPC 69	478	346.7	9.0	74.9
SLTPC 70	483	349.7	8.7	72.6
SLTPC 73	498	358.9	8.5	71.0
SLTPC 75	508	365.1	8.2	68.4
SLTPC 76	513	368.1	7.7	64.3
SLTPC 79	528	377.3	8.4	70.4
SLTPC 80	533	380.4	7.9	65.8
SLTPC 80	533	380.4	8.0	66.7
SLTPC 82	543	386.5	8.0	66.9
SLTPC 83	548	389.6	7.0	58.2
SLTPC 84	553	392.7	7.1	59.3
SLTPC 85	558	395.7	7.0	58.3
SLTPC 87	568	401.9	9.0	75.2
SLTPC 89	578	408.0	8.4	70.0
SLTPC 90	583	411.2	8.2	68.6
SLTPC 91	588	414.3	8.2	68.3
SLTPC 92	593	417.5	8.5	70.8
SLTPC 93	438	420.6	8.6	71.6

Sample ID	Depth (cm)	Age (ka)	%IC	%CaCO3
SLTPC 94	603	423.8	8.5	70.8
SLTPC 95	608	427.0	8.8	73.1
SLTPC 96	613	430.1	9.3	77.2
SLTPC 97	618	433.3	9.1	75.9
SLTPC 98	623	436.5	8.6	71.8
SLTPC 99	628	439.6	8.0	66.8
SLTPC 100	633	442.8	8.9	73.8
SLTPC 101	638	445.9	8.4	70.1
SLTPC 101	638	445.9	8.4	70.4
SLTPC 103	648	452.3	8.7	72.5
SLTPC 104	653	455.4	8.1	67.9
SLTPC 105	658	458.6	8.7	72.5
SLTPC 106	663	461.7	8.7	72.4
SLTPC 107	668	464.9	8.1	67.2
SLTPC 110	683	474.4	7.3	60.5
SLTPC 111	688	477.6	7.8	64.9
SLTPC 113	698	487.7	7.6	63.6
SLTPC 115	708	498.3	7.9	65.6
SLTPC 120	733	524.7	7.6	63.6
SLTPC 125	758	551.0	6.6	54.7
SLTPC 125	758	551.0	8.0	66.5
SLTPC 130	783	575.6	7.7	64.3
SLTPC 135	808	595.0	7.8	65.0
SLTPC 140	833	614.4	7.1	58.8
SLTPC 145	858	634.2	8.0	66.9
SLTPC 150	603	655.5	7.4	61.5

Table A1.5: % Organic Carbon (%OC) as calculated from % Total Carbon (%TC) and % Inorganic carbon (%IC) measured by coulometry

Sample	Age (ka)	Depth (cm)	%TC	%IC	%OC
SLTTC2	8.6	9.75	9.2	8.6	0.6
SLTTC10	45.3	50.5	9.5	9.1	0.4
SLTPC1	123.9	138	9.4	8.7	0.7
SLTPC3	132.1	148	8.7	8.3	0.4
SLTPC10	160.5	183	9.5	8.5	1.0
SLTPC20	197.1	233	8.5	8.5	0.1
SLTPC33	236.8	298	8.1	7.9	0.2
SLTPC38	252.1	323	9.2	9.1	0.1
SLTPC60	319.2	433	9.6	8.7	0.9
SLTPC70	349.7	483	9.1	8.7	0.4
SLTPC80	380.4	533	8.3	7.9	0.5
SLTPC89	408	578	9.2	8.4	0.8
SLTPC99	439.6	628	8.7	8.0	0.7
SLTPC110	474.4	683	8.1	7.3	0.8

Table A1.6: Bulk uranium and molybdenum concentrations measured by ICP-MS

Sample ID	Age (ka)	Depth (cm)	Mo (ppm)	%SD	U (ppm)	%SD
SLTTC2/1	8.6	9.8	8.9	2.4	4.5	0.9
SLTTC2/2	8.6	9.8	9.2	1.3	4.6	1.8
SLTTC3	13.3	15.5	6.7	2.8	5.5	1.4
SLTTC5	22.8	25.5	9.6	2.2	3.7	1.0
SLTTC7	31.8	35.5	10.1	2.3	5.8	2.1
SLTTC11	49.8	55.5	17.5	1.6	5.7	1.5
SLTTC15	67.9	75.5	19.5	2.4	2.7	1.7
SLTTC18	81.4	90.5	11.0	1.8	6.2	1.3
SLTPC4	133.1	153	5.2	1.7	2.9	1.0
SLTPC14	176.8	203	1.7	2.4	2.4	1.2
SLTPC24	209.4	253	4.7	1.5	2.6	0.4
SLTPC34	239.9	303	4.6	2.6	4.7	1.8
SLTPC54	300.9	403	3.8	2.1	4.2	1.3
SLTPC64	331.4	453	3.3	2.1	5.3	1.2
SLTPC74	362.0	503	2.6	2.1	12.1	2.0
SLTPC88	404.9	573	3.1	1.8	4.4	1.2
SLTPC95/1	427.0	608	2.3	1.6	15.7	2.2
SLTPC95/2	427.0	608	2.3	2.3	14.8	2.5
SLTPC98	436.5	623	2.6	4.1	15.7	2.0
SLTPC103	452.3	648	2.8	2.6	15.1	2.0
SLTPC106	461.7	663	2.5	4.4	13.0	2.0
SLTPC108	468.1	673	5.6	2.7	14.2	2.3
SLTPC115	498.3	708	3.4	2.1	11.4	1.5
SLTPC124	545.8	753	3.0	1.5	12.4	1.3
SLTPC134	591.1	803	4.8	1.8	11.9	1.4
SLTPC144	630.0	853	2.9	3.1	8.4	1.5

Table A1.7 $\delta^{18}O$ record as measured by stable isotope mass spectroscopy

Trigger Core		
	Combined Depth (cm)	d18O
SLTTC1	5.25	-0.970
SLTTC2	9.75	-0.745
SLTTC3	15.0	-0.323
SLTTC4	20.5	-0.206
SLTTC5	25.5	-0.102
SLTTC6	30.5	-0.224
SLTTC7	35.5	-0.550
SLTTC8	40.5	-0.324
SLTTC9	45.5	-0.434
SLTTC10	50.5	-0.408
SLTTC11	55.5	-0.339
SLTTC12	60.5	-0.344
SLTTC13	65.5	-0.281
SLTTC14	70.5	-0.369
SLTTC15	75.5	-0.371
SLTTC16	80.5	-0.306
SLTTC17	85.5	-0.382
SLTTC18	90.5	-0.510
SLTTC19	95.5	-0.659
SLTTC20	100.5	-0.778
SLTTC21	105.5	-0.897
SLTTC22	110.5	-1.042
SLTTC23	115.5	-0.869
SLTTC24	120.5	-1.044
SLTTC25	125.5	-1.047
SLTTC26	130.5	-1.091
SLTTC27	135.5	-1.209
SLTTC28	140.5	-1.035
SLTTC29	145.5	-0.930

Piston Core		
	Combined Depth (cm)	d18O
SLTTC30	150.5	-0.479
SLTTC31	155.5	-0.407
SLTTC32	160.5	-0.162
SLTTC33	165.5	-0.268
SLTPC1	138	-0.859
SLTPC2	143	-0.919
SLTPC3	148	-0.718
SLTPC4	153	-0.342
SLTPC5	158	-0.122
SLTPC6	163	-0.140
SLTPC7	168	-0.196
SLTPC8	173	-0.138
SLTPC9	178	-0.045
SLTPC10	183	0.053
SLTPC11	188	-0.257
SLTPC12	193	-0.020
SLTPC13	198	-0.327
SLTPC14	203	-0.464
SLTPC15	208	-0.400
SLTPC16	213	-0.141
SLTPC17	218	-0.497
SLTPC18	223	-0.457
SLTPC19	228	-0.706
SLTPC20	233	-0.888
SLTPC21	238	-0.993
SLTPC22	243	-1.035
SLTPC23	248	-0.903
SLTPC24	253	-0.839
SLTPC25	258	-0.763

Piston Core		
	Combined Depth (cm)	d18O
SLTPC26	263	-0.738
SLTPC27	268	-0.671
SLTPC28	273	-0.507
SLTPC29	278	-0.552
SLTPC30	283	-0.623
SLTPC31	288	-0.507
SLTPC32	293	-0.536
SLTPC33	298	-0.312
SLTPC34	303	-0.574
SLTPC35	308	-0.475
SLTPC36	313	-0.155
SLTPC37	318	-0.158
SLTPC38	323	-0.210
SLTPC39	328	-0.126
SLTPC40	333	-0.165
SLTPC41	338	-0.189
SLTPC42	343	-0.233
SLTPC43	348	-0.152
SLTPC44	353	-0.079
SLTPC45	358	-0.060
SLTPC46	363	-0.107
SLTPC47	368	-0.334
SLTPC48	373	-0.384
SLTPC49	378	-0.277
SLTPC50	383	-0.405
SLTPC51	388	-0.155
SLTPC52	393	-0.413
SLTPC53	398	-0.295
SLTPC54	403	-0.197

Piston Core		
	Combined Depth (cm)	d18O
SLTPC55	408	-0.237
SLTPC56	413	-0.173
SLTPC57	418	-0.480
SLTPC58	423	-0.355
SLTPC59	428	-0.371
SLTPC60	433	-0.451
SLTPC61	438	-0.486
SLTPC62	443	-0.443
SLTPC63	448	-0.435
SLTPC64	453	-0.383
SLTPC65	458	-0.369
SLTPC66	463	0.019
SLTPC67	468	0.093
SLTPC68	473	0.265
SLTPC69	478	0.192
SLTPC70	483	0.188
SLTPC71	488	0.187
SLTPC72	493	0.209
SLTPC73	498	0.329
SLTPC74	503	0.318
SLTPC75	508	0.247
SLTPC76	513	0.263
SLTPC77	518	0.050
SLTPC78	523	0.018
SLTPC79	528	0.017
SLTPC80	533	-0.122
SLTPC81	538	-0.283
SLTPC82	543	-0.311
SLTPC83	548	-0.691
SLTPC84	553	-0.597

Table A1.7 Continued: $\delta^{18}O$ record as measured by stable isotope mass spectroscopy

Piston Core	Adjusted depth	d18O
SLTPC85	558	-0.556
SLTPC86	563	-0.655
SLTPC87	568	-0.584
SLTPC88	573	-0.424
SLTPC89	578	-0.246
SLTPC90	583	-0.049
SLTPC91	588	0.167
SLTPC92	593	0.317
SLTPC93	598	0.554
SLTPC94	603	0.794
SLTPC95	608	0.805
SLTPC96	613	0.762
SLTPC97	618	0.665
SLTPC98	623	0.472
SLTPC99	628	0.395
SLTPC100	633	0.325
SLTPC101	638	0.367
SLTPC102	643	0.359
SLTPC103	648	0.266
SLTPC104	653	0.395
SLTPC105	658	0.417
SLTPC106	663	0.374
SLTPC107	668	0.274
SLTPC108	673	0.234
SLTPC109	678	-0.080
SLTPC110	683	-0.256
SLTPC111	688	-0.562

Piston Core	Adjusted depth	d18O
SLTPC112	693	-0.556
SLTPC113	698	-0.432
SLTPC114	703	-0.454
SLTPC115	708	-0.451
SLTPC116	713	-0.262
SLTPC117	718	-0.318
SLTPC118	723	-0.426
SLTPC119	728	-0.393
SLTPC120	733	-0.462
SLTPC121	738	-0.389
SLTPC122	743	-0.261
SLTPC123	748	-0.179
SLTPC124	753	-0.098
SLTPC125	758	-0.281
SLTPC126	763	-0.198
SLTPC127	768	-0.313
SLTPC128	773	-0.485
SLTPC129	778	-0.422
SLTPC130	783	-0.482
SLTPC131	788	-0.353
SLTPC132	793	-0.234
SLTPC133	798	-0.220
SLTPC134	803	-0.104
SLTPC135	808	-0.250
SLTPC136	813	-0.348
SLTPC137	818	-0.436
SLTPC138	823	-0.479

Piston Core	Adjusted depth	d18O
SLTPC139	828	-0.562
SLTPC140	833	-0.641
SLTPC141	838	-0.298
SLTPC142	843	-0.269
SLTPC143	848	-0.020
SLTPC144	853	0.368
SLTPC145	858	0.228
SLTPC146	863	0.286
SLTPC147	868	0.255
SLTPC148	873	0.203
SLTPC149	878	0.172
SLTPC150	883	0.186
SLTPC151	888	0.144
SLTPC152	893	0.074
SLTPC153	898	0.189
SLTPC154	903	0.004
SLTPC155	908	-0.188
SLTPC156	913	-0.324
SLTPC157	918	-0.337
SLTPC158	923	-0.415
SLTPC159	928	-0.378
SLTPC160	933	-0.392
SLTPC161	938	-0.212
SLTPC162	943	-0.134
SLTPC163	948	-0.075
SLTPC164	953	-0.096
SLTPC165	958	0.038

Appendix 2: Comparison of ICP-AES and XRF analyses and ICP-AES corrected dataset

The bulk geochemistry of the core was measured by both XRF and ICP-AES (Raw data contained in Appendix 1). There is a degree of conflict with the concentrations measured by these two different techniques (Figure A2.1). They generally fall on a linear array, but there is a systematic offset between the two sets of data.

A2.1 ICP-AES

The accuracy of ICP-AES was assessed by analysis of USGS certified reference standard MAG-1. Agreement between Data and certified values of elements of interest is generally good.

Table A2.1: Accuracy of ICP-AES Measurements

Element	Certified Value			Measured 1	Measured 2	Average	Accuracy (%)
Al (wt%)	8.68	±	0.16	8.27	8.11	8.19	0.94
Fe (wt%)	4.76	±	0.42	5.13	5.09	5.11	1.07
K (wt%)	2.95	±	0.14	2.89	2.84	2.86	0.97
Mg (wt%)	1.81	±	0.06	1.78	1.75	1.76	0.97
Ca (wt%)	0.98	±	0.07	0.96	0.95	0.96	0.98
Ti (wt%)	0.45	±	0.04	0.44	0.43	0.44	0.97
Mn (wt%)	0.076	±	0.01	0.08	0.08	0.08	1.09
P (wt%)	0.07	±	0.01	0.07	0.07	0.07	0.97
Ba (µg/g)	480	±	41	479	475	477	0.99
Sr (µg/g)	150	±	15	143	141	142	0.95
V (µg/g)	140	±	6	138	136	137	0.98
Zn (µg/g)	130	±	6	137	135	136	1.05
Cu (µg/g)	30	±	3	27	26	27	0.88
As (µg/g)	9.2	±	NM	11.8	5.7	8.8	0.95

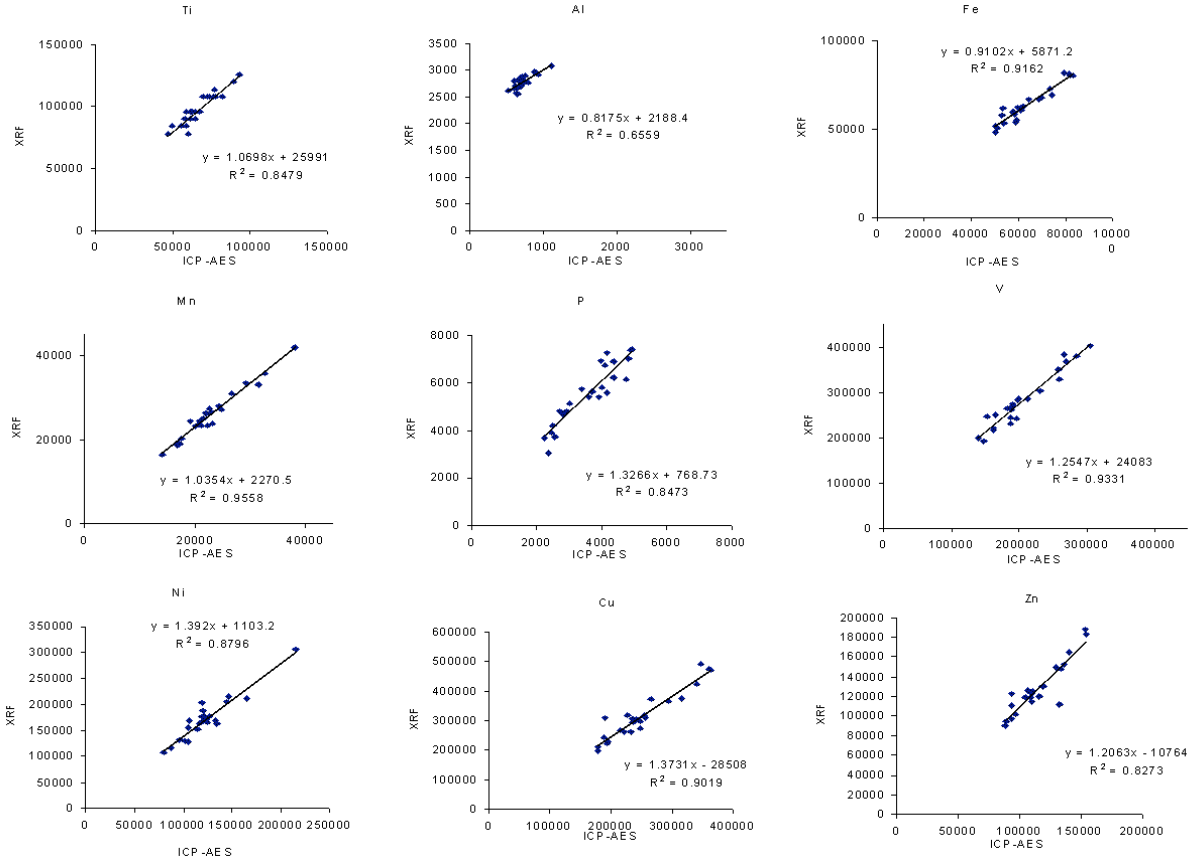

Figure A2.1 Comparison of XRF and ICP-AES data

A2.2: XRF

Accuracy of the XRF measurements is assessed by comparison between measurements made by the Phillips PW1400 fully automatic wavelength dispersive XRF and Pananlytical Epsilon Polarised XRF, which had precision of better than 3% RSD.

Table A2.2: Precision and Accuracy of Pananlytical Epsilon Polarised XRF

Sample Identification	Fe2O3 Conc. (%)	MnO Conc. (%)	Cu Conc. (ppm)	Zn Conc. (ppm)	As Conc. (ppm)
Expected	**6.8**	**0.098**	**30**	**130**	**9.2**
MAG-1	7.12	0.11	26.06	140.06	7.77
MAG-1	7.06	0.11	25.69	141.09	7.62
MAG-1	7.13	0.11	27.21	141.50	7.96
MAG-1	7.09	0.11	27.20	139.49	7.55
MAG-1	7.07	0.11	25.69	140.14	7.76
Average	7.09	0.11	26.37	140.46	7.73
Standard Deviation	0.03	0.00	0.78	0.82	0.16
RSD %	0.4326	0.0000	2.9454	0.5811	2.0508

Figure A2.2 shows a comparison of the XRF data between the two XRF instruments. Agreement is reasonable, but the Phillips PW1400 underestimates the Fe_2O_3 and MnO slightly, and greatly overestimates the As (by a factor of over 2). This discrepancy is consistent with that observed between the Phillips PW1400 XRF and the ICP-AES.

These comparisons and the certified reference data from the ICP-AES suggest that this is the more reliable technique for this suite of samples. Correction to the ICP-AES data also brings trace element concentrations more in line with what would be expected in this region. Therefore where used, all XRF data has been corrected to the ICP-AES data. Corrected data is contained in Table A2.3

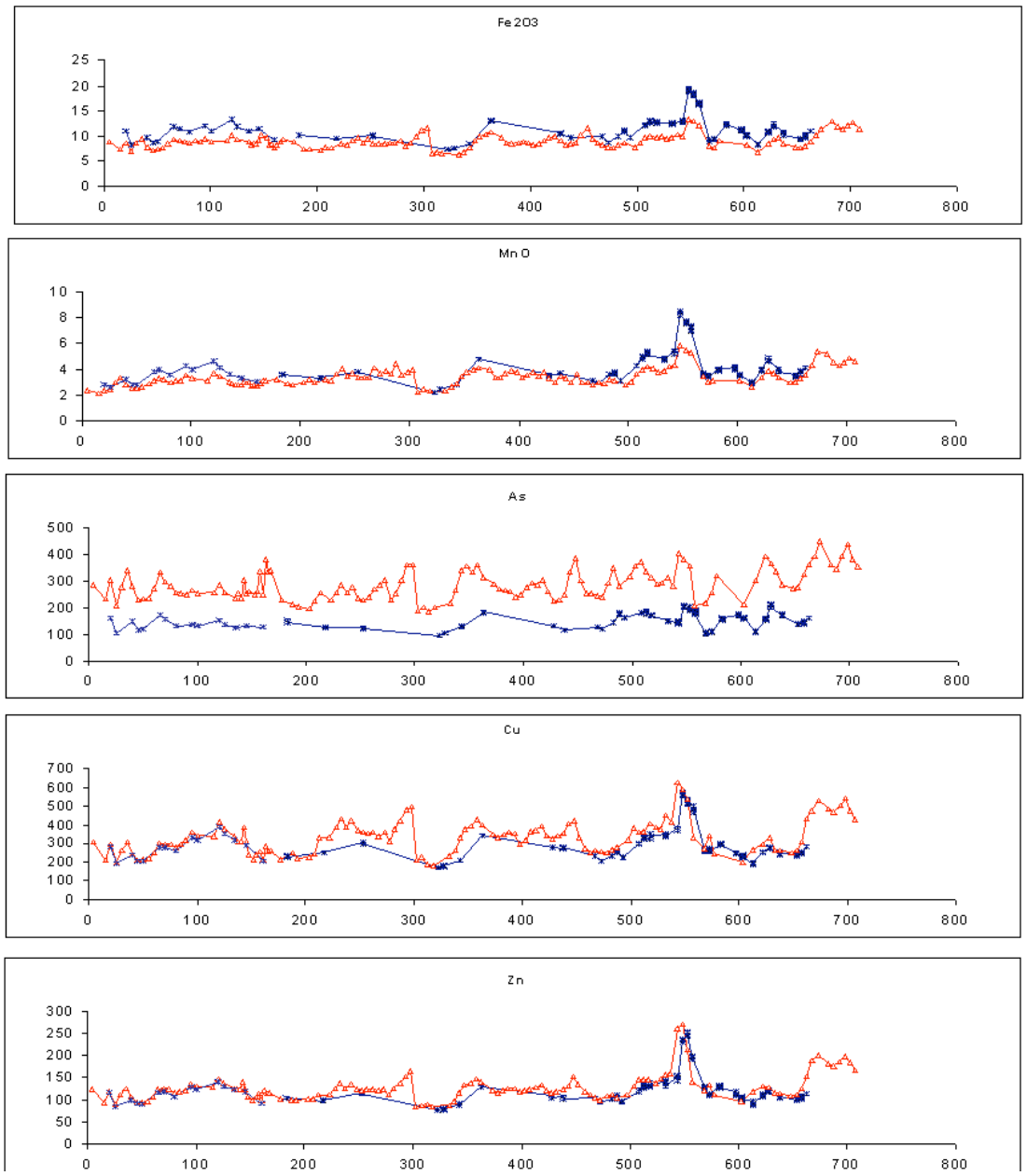

Figure A2.2: Data comparison between 2 XRF instruments. Red line: Phillips PW1000: Blue line: Pananalytical Epsilon 5.

Table A2.3 ICP-AES Corrected XRF data.

Adjusted Depth (cm)	Age (ka)	Fe (wt %)	Mn (wt%)	Ca (%)	P (%)	V (ppm)	Cu (ppm)	Zn (ppm)	As (ppm)	Ni (ppm)
5.25	4.5	6.2	1.6	28.6	0.3	178	245	110	100	92
15.5	13.3	5.0	1.4	30.4	0.3	140	173	87	80	76
20.5	18.3	6.1	1.5	28.2	0.3	169	237	108	106	93
25.5	22.8	4.7	1.6	30.3	0.2	134	165	84	71	92
30.5	27.3	6.0	2.0	28.8	0.3	184	211	101	96	111
35.5	31.8	6.7	2.3	27.7	0.5	209	244	112	119	127
40.5	36.3	5.4	1.9	28.8	0.4	164	200	96	97	103
45.5	40.8	4.9	1.7	30.0	0.3	150	174	87	78	78
50.5	45.3	5.0	1.7	30.6	0.3	146	178	87	79	82
55.5	49.8	5.2	1.7	30.3	0.3	157	182	89	81	83
60.5	54.4	5.9	1.9	28.9	0.4	182	204	97	95	101
65.5	58.9	6.4	2.1	28.1	0.5	191	239	111	117	119
70.5	63.4	6.3	2.3	28.4	0.4	203	237	112	103	129
75.5	67.9	6.2	2.2	28.9	0.4	195	236	112	97	127
80.5	72.4	6.1	2.0	29.1	0.3	195	225	105	89	117
85.5	76.9	6.3	2.1	28.6	0.3	208	237	108	87	121
90.5	81.4	6.3	2.1	29.0	0.3	207	251	110	86	119
95.5	85.9	6.7	2.5	27.7	0.3	230	283	121	92	136
100.5	90.4	6.1	2.3	29.1	0.3	200	269	117	87	130
115.5	103.9	6.3	2.2	28.8	0.3	198	264	115	89	116
120.5	108.4	7.2	2.6	27.3	0.3	246	323	132	99	146
125.5	113.0	6.5	2.4	28.3	0.3	220	294	122	89	138
135.5	121.9	6.1	2.1	28.8	0.2	205	264	113	81	142
138	123.9	5.8	1.9	29.4	0.2	183	252	114	76	135
140.5	126.0	6.0	1.9	29.4	0.2	188	248	110	81	118

Table A2.3 Continued: ICP-AES Corrected XRF data.

Depth (cm)	Age (ka)	Fe (wt %)	Mn (wt%)	Ca (%)	P (%)	V (ppm)	Cu (ppm)	Zn (ppm)	As (ppm)	Ni (ppm)
143	128.0	5.9	1.9	29.5	0.2	184	250	111	79	116
145.5	130.0	6.4	1.9	28.8	0.3	206	243	111	87	111
148	132.1	7.1	2.1	28.4	0.3	218	303	125	107	145
153	136.1	6.8	2.0	27.9	0.4	209	247	116	110	122
155.5	138.2	5.7	1.8	29.5	0.3	172	196	98	90	99
158	140.2	5.8	1.9	30.8	0.3	170	224	99	92	121
160.5	142.2	5.2	1.8	30.1	0.4	150	180	90	85	94
163	144.3	5.8	2.0	28.7	0.4	174	197	99	101	104
165.5	146.3	6.2	2.1	28.1	0.5	190	208	102	119	111
168	148.3	6.6	2.1	27.5	0.6	190	228	109	134	118
178	156.5	6.2	2.2	28.0	0.5	192	213	106	120	116
188	164.6	5.0	1.9	30.0	0.3	161	178	93	79	105
193	168.7	5.1	1.9	31.3	0.2	148	204	90	73	115
198	172.7	4.9	2.0	30.4	0.2	160	183	92	69	107
203	176.8	4.9	2.0	30.4	0.2	154	186	93	67	108
208	180.9	5.3	2.2	30.8	0.3	175	224	93	73	124
213	184.9	5.1	2.0	30.0	0.3	165	199	93	77	105
223	191.0	5.9	2.2	30.0	0.3	187	260	102	89	133
228	194.1	5.6	2.1	30.9	0.2	178	261	101	79	130
233	197.1	6.4	2.5	29.1	0.3	218	302	113	89	140
238	200.2	6.8	2.8	28.4	0.3	236	334	123	99	155
243	203.3	6.1	2.4	30.1	0.2	197	302	114	88	128
248	206.3	6.6	2.6	29.1	0.3	221	326	122	96	136
253	209.4	5.9	2.3	30.2	0.2	191	292	112	82	121
258	212.4	5.8	2.3	30.0	0.2	186	282	110	78	117
263	215.5	5.8	2.3	30.4	0.2	185	280	110	82	123

Table A2.3 Continued: ICP-AES Corrected XRF data

Depth (cm)	Age (ka)	Fe (wt %)	Mn (wt%)	Ca (%)	P (%)	V (ppm)	Cu (ppm)	Zn (ppm)	As (ppm)	Ni (ppm)
268	218.5	6.1	2.9	28.8	0.4	214	282	111	92	161
273	221.6	6.0	2.6	29.6	0.3	191	265	108	99	139
278	224.6	6.4	2.7	29.5	0.3	219	280	112	106	146
283	227.7	5.5	2.5	30.5	0.2	197	249	101	78	144
288	230.7	6.1	3.1	30.1	0.2	214	296	114	87	165
293	233.8	7.1	2.5	29.1	0.3	237	327	123	106	131
298	236.8	7.9	2.6	28.1	0.3	265	370	135	127	137
303	239.9	8.3	2.8	27.5	0.3	274	380	146	127	145
308	242.9	4.4	1.4	33.1	0.2	122	176	79	63	87
313	246.0	4.6	1.7	31.7	0.3	136	187	82	69	97
318	249.0	4.3	1.5	31.4	0.2	134	157	84	62	74
333	258.2	4.2	1.5	31.4	0.3	124	154	80	68	78
338	261.2	4.6	1.7	31.7	0.4	143	189	82	74	99
343	264.3	5.2	1.9	30.6	0.5	162	211	88	92	107
348	267.3	6.4	2.4	28.7	0.6	198	259	106	120	135
353	270.4	7.0	2.6	27.9	0.5	220	295	120	126	158
358	273.4	7.3	2.7	27.9	0.5	237	309	123	117	162
363	276.5	7.7	2.9	27.1	0.5	248	333	131	127	172
373	282.6	6.8	2.8	28.2	0.4	230	309	124	109	150
378	285.6	6.0	2.3	30.3	0.3	184	272	110	101	126
383	288.7	5.9	2.3	30.0	0.4	196	262	105	93	127
388	291.7	6.1	2.5	29.6	0.3	206	275	110	92	161
393	294.8	6.1	2.7	29.3	0.3	210	281	114	90	158
398	297.8	6.0	2.6	29.6	0.3	210	276	112	83	144
403	300.9	5.8	2.3	29.2	0.3	197	237	108	85	118
408	303.9	5.9	2.4	28.6	0.4	201	251	109	95	120

Table A2.3 Continued: ICP-AES Corrected XRF data

Depth (cm)	Age (ka)	Fe (wt %)	Mn (wt%)	Ca (%)	P (%)	V (ppm)	Cu (ppm)	Zn (ppm)	As (ppm)	Ni (ppm)
413	307.0	6.3	2.6	29.2	0.4	221	287	112	102	135
418	310.0	6.8	2.4	28.8	0.4	233	291	115	98	125
423	313.1	7.1	2.6	28.4	0.4	243	307	120	107	132
428	316.1	6.4	2.3	29.8	0.3	217	271	109	90	124
433	319.2	5.7	2.0	30.6	0.2	180	257	105	76	130
438	322.2	5.9	2.4	29.8	0.2	201	268	108	78	147
443	325.3	6.1	2.3	30.4	0.2	195	279	111	86	129
448	328.3	7.2	2.0	29.5	0.3	217	314	117	117	121
453	331.4	8.3	2.5	25.4	0.5	287	329	135	136	125
458	334.4	6.7	2.0	28.0	0.4	225	262	122	105	108
463	337.5	6.0	2.0	28.8	0.3	209	221	107	86	104
468	340.5	5.7	1.9	29.4	0.3	194	203	102	87	100
473	343.6	5.4	2.0	30.6	0.4	177	211	94	85	119
478	346.7	5.3	2.0	30.7	0.4	174	207	91	83	116
483	349.7	5.6	2.2	29.0	0.4	180	203	100	102	118
488	352.8	6.1	2.2	28.1	0.6	189	217	102	123	112
498	358.9	5.4	1.9	31.3	0.4	158	226	95	97	120
503	362.0	6.1	2.0	30.3	0.4	176	253	102	111	135
508	365.1	6.9	2.5	28.9	0.4	203	297	118	126	161
513	368.1	7.1	2.8	26.0	0.5	221	282	129	131	163
518	371.2	6.8	2.9	26.9	0.4	224	284	129	118	181
523	374.3	7.1	2.8	27.9	0.4	231	315	130	110	165
528	377.3	6.7	2.6	28.2	0.4	217	303	124	101	158
533	380.4	6.8	2.7	27.5	0.3	228	293	132	102	146
538	383.5	7.4	2.9	27.6	0.3	248	347	140	109	174
543	386.5	7.0	3.0	27.3	0.2	249	323	141	97	166

Table A2.3 Continued: ICP-AES Corrected XRF data

Depth (cm)	Age (ka)	Fe (wt %)	Mn (wt%)	Ca (%)	P (%)	V (ppm)	Cu (ppm)	Zn (ppm)	As (ppm)	Ni (ppm)
548	389.6	9.7	4.2	22.8	0.3	343	477	226	144	210
553	392.7	9.3	3.8	23.8	0.3	325	447	233	134	203
558	395.7	8.6	3.7	23.6	0.2	304	412	185	126	178
568	401.9	5.6	2.4	30.5	0.2	191	263	125	71	145
573	404.9	5.3	2.1	30.8	0.2	174	220	109	74	116
578	408.0	6.3	2.1	30.5	0.2	197	271	119	89	123
603	423.8	5.7	2.1	28.8	0.5	180	198	101	113	111
613	430.1	4.6	1.8	30.8	0.3	145	167	89	73	95
623	436.5	5.9	2.3	29.0	0.4	191	215	108	105	117
628	439.6	6.6	2.7	27.5	0.6	210	238	117	139	130
633	442.8	6.8	2.6	28.0	0.6	223	262	116	129	142
638	445.9	5.8	2.3	28.3	0.5	179	211	104	119	116
648	452.3	5.4	2.0	30.0	0.4	166	212	104	98	121
653	455.4	5.3	2.1	30.0	0.4	164	202	99	95	108
658	458.6	5.5	2.2	29.3	0.4	175	214	102	96	113
663	461.7	6.2	2.4	28.0	0.5	199	244	113	114	126
668	464.9	7.2	3.0	26.8	0.4	233	334	135	126	200
673	468.1	8.2	3.8	24.7	0.4	284	367	165	139	219
683	474.4	9.4	3.7	23.6	0.4	327	408	176	159	173
688	477.6	8.5	3.2	25.3	0.3	299	372	159	127	145
693	482.5	8.1	3.0	26.1	0.3	288	359	156	121	140
698	487.7	8.6	3.2	25.1	0.3	302	384	163	138	158
703	493.0	9.2	3.4	24.3	0.4	332	416	174	155	168
708	498.3	8.2	3.2	25.6	0.3	302	364	161	134	153
713	503.6	7.9	2.9	26.2	0.3	287	331	148	124	141
718	508.8	8.2	3.0	25.9	0.3	297	341	152	133	147

Table A2.3 Continued: ICP-AES Corrected XRF data

Depth (cm)	Age (ka)	Fe (wt %)	Mn (wt%)	Ca (%)	P (%)	V (ppm)	Cu (ppm)	Zn (ppm)	As (ppm)	Ni (ppm)
723	514.1	8.8	3.2	25.1	0.4	320	368	161	147	157
728	519.4	9.7	3.6	23.4	0.5	352	420	180	182	176
733	524.7	8.3	3.1	25.4	0.5	293	346	152	155	146
738	529.9	7.2	2.7	26.8	0.5	247	289	133	133	124
743	535.2	6.8	2.6	27.5	0.4	236	266	125	122	122
748	540.5	6.9	2.7	27.3	0.5	230	269	123	125	128
753	545.8	7.4	3.0	26.3	0.5	259	287	133	140	147
758	551.0	6.8	2.8	26.9	0.5	238	270	124	126	134
763	556.3	6.6	2.6	27.6	0.4	230	264	122	115	138
768	561.6	7.1	2.8	26.7	0.4	243	296	128	132	149
773	566.9	8.0	3.3	25.4	0.5	279	348	148	152	159
778	571.7	8.6	3.8	24.7	0.4	319	403	167	154	203
783	575.6	7.9	3.6	25.8	0.3	288	376	162	134	165
793	583.3	7.9	3.6	25.3	0.5	286	370	159	149	173
798	587.2	7.6	3.2	25.7	0.5	267	321	143	153	151
803	591.1	7.0	3.0	27.0	0.4	243	294	131	130	151
808	595.0	7.1	3.1	26.7	0.4	246	308	135	133	154
813	598.9	7.5	3.0	26.3	0.4	259	321	139	131	141
818	602.8	7.8	3.0	26.3	0.3	274	336	145	131	129
823	606.6	8.0	3.1	26.1	0.3	296	355	155	130	124
828	610.5	8.0	3.0	26.1	0.3	285	354	155	129	121
833	614.4	9.9	3.6	23.4	0.4	352	453	189	174	146
838	618.3	11.7	4.3	20.5	0.6	420	538	223	246	174
843	622.2	9.6	5.0	22.3	0.5	360	415	197	200	215
848	626.1	7.4	4.9	25.3	0.4	269	304	147	146	206
853	630.0	6.7	2.4	27.8	0.5	223	210	117	131	93

Table A2.3 Continued: ICP-AES Corrected XRF data

Depth (cm)	Age (ka)	Fe (wt %)	Mn (wt%)	Ca (%)	P (%)	V (ppm)	Cu (ppm)	Zn (ppm)	As (ppm)	Ni (ppm)
858	634.2	6.9	2.5	27.5	0.5	231	220	117	139	105
863	638.5	6.5	2.4	28.0	0.5	214	205	112	124	95
868	642.7	6.8	2.5	27.7	0.5	221	210	117	130	100
873	647.0	8.4	6.9	22.4	0.6	327	363	166	187	295
878	651.2	9.3	3.2	23.8	0.7	313	310	154	204	145
883	655.5	8.5	3.3	24.9	0.6	293	298	148	171	160
888	659.7	7.6	2.8	26.5	0.5	253	269	133	150	143
893	664.0	7.3	2.5	27.1	0.4	245	261	127	130	135
898	668.2	7.7	2.6	26.7	0.4	270	286	130	131	148
903	672.5	10.0	3.5	23.3	0.5	368	408	175	184	195
908	676.7	9.1	3.4	24.5	0.4	344	392	167	149	171
913	681.0	10.0	3.7	23.3	0.3	374	457	191	167	192
918	685.2	11.6	4.2	20.8	0.6	441	548	218	222	203
923	689.5	9.0	3.7	24.4	0.4	341	419	176	150	182
928	693.7	8.9	3.3	24.7	0.4	340	392	173	147	136
933	698.0	8.0	3.1	25.8	0.3	298	351	160	130	135
938	702.2	8.0	3.4	25.6	0.4	285	344	163	140	145
943	706.5	8.2	3.3	24.8	0.6	280	328	161	169	138
948	710.7	7.1	2.8	26.2	0.5	228	270	136	139	120
953	715.0	7.7	3.2	25.2	0.6	263	294	143	161	150
958	719.2	7.5	3.5	25.6	0.5	266	298	137	151	181
963	723.5	8.1	2.8	25.6	0.6	284	263	132	150	124
968	727.7	7.1	2.9	26.7	0.4	255	240	125	113	136
973	732.0	7.0	4.4	26.0	0.4	275	296	141	112	221
978	736.3	8.1	3.6	25.1	0.5	311	301	152	136	163
983	740.5	8.6	4.2	24.0	0.5	341	353	175	155	220

Table A2.4: Concentrations found in the bulk sediment and in the easily reducible (ferrihydrite) fraction. Sequential extraction data are presented as measured by ICP-AES.

Depth (cm)	Age (ka)	Bulk concentration									Concentration in easily reducible oxides (extraction b)								
		Al (%)	P (%)	Fe (%)	Mn (%)	Ca (%)	V (ppm)	Cu (ppm)	Zn (ppm)	As (ppm)	Al (%)	P (%)	Fe (%)	Mn (%)	Ca (%)	V (ppm)	Cu (ppm)	Zn (ppm)	As (ppm)
9.8	8.6	0.07	0.28	5.3	1.7	29.9	153	190	94	84	0.04	0.12	3.6	1.3	23.7	11.4	146	66	59
15.5	13.3	0.06	0.27	5.0	1.4	29.5	141	179	89	78	0.04	0.09	3.4	1.1	24.0	10.6	142	63	42
25.5	22.8	0.07	0.25	5.0	1.7	30.2	148	177	88	79	0.03	0.07	3.0	1.3	23.3	10.2	130	56	31
35.5	31.8	0.07	0.40	6.4	2.2	27.5	199	242	110	116	0.03	0.09	3.9	1.7	21.9	14.1	175	75	31
55.5	49.8	0.07	0.30	5.4	1.8	30.3	163	195	94	93	0.04	0.12	3.4	1.4	24.5	11.8	145	65	45
75.5	67.9	0.07	0.34	6.1	2.1	29.3	189	236	109	86	0.03	0.10	3.4	1.6	22.5	12.5	156	70	37
90.5	81.4	0.08	0.25	6.2	2.1	29.4	199	256	110	90	0.04	0.09	3.4	1.6	22.6	13.4	165	70	27
153	133.1	0.09	0.37	7.0	2.1	27.7	212	256	119	118	0.04	0.20	3.7	1.6	21.4	14.5	155	77	44
203	176.8	0.07	0.22	5.1	2.0	30.1	162	195	97	70	0.03	0.14	3.0	1.6	23.7	11.3	129	61	34
253	209.4	0.11	0.26	5.7	2.3	28.5	189	266	110	86	0.05	0.09	2.9	1.8	22.3	12.7	162	67	19
303	239.9	0.06	0.39	7.9	2.7	25.9	268	348	140	123	0.03	0.22	4.2	2.0	20.6	18.5	209	88	38
403	300.9	0.07	0.29	5.9	2.3	29.1	192	249	109	91	0.04	0.19	3.6	1.8	22.0	13.8	168	74	44
453	331.4	0.05	0.49	8.1	2.4	26.4	266	340	136	135	0.03	0.12	3.8	1.8	20.1	17.0	192	82	24
503	362.0	0.08	0.47	6.1	2.1	28.9	187	228	133	116	0.04	0.25	3.5	1.6	21.9	13.3	156	68	45
573	404.9	0.06	0.24	5.9	2.3	29.3	197	249	116	85	0.03	0.09	2.7	1.6	20.4	12.1	137	65	23
608	427.0	0.06	0.42	5.3	1.9	30.5	165	188	94	91	0.03	0.20	2.9	1.4	23.1	11.1	122	60	40
623	436.5	0.06	0.41	5.8	2.2	29.1	183	215	105	101	0.03	0.29	3.7	1.7	22.6	13.4	154	74	76
648	452.3	0.06	0.42	5.9	2.2	29.7	188	232	110	107	0.03	0.29	3.8	1.7	23.1	13.8	164	78	69
663	461.7	0.07	0.44	6.0	2.3	28.5	190	236	107	115	0.04	0.31	3.8	1.7	23.1	13.6	167	75	75
673	468.1	0.09	0.40	8.2	3.8	25.1	285	360	153	125	0.04	0.06	4.0	2.9	19.6	18.9	223	97	17
708	498.3	0.07	0.36	8.3	3.3	26.3	306	364	154	129	0.04	0.15	4.6	2.6	20.7	21.9	233	107	25
753	545.8	0.07	0.49	7.3	2.9	26.8	258	294	130	138	0.04	0.21	4.2	2.3	21.2	18.4	195	92	44
803	591.1	0.08	0.44	7.4	3.1	28.1	259	316	133	133	0.03	0.06	3.3	2.3	21.6	16.5	184	82	19
853	630.0	0.07	0.48	6.9	2.5	28.0	231	221	119	139	0.03	0.29	4.0	1.9	22.0	16.8	147	80	62

Table A2.4 Continued: Concentrations found in the reducible (goethite) fraction and the residual fraction remaining after sequential leaching Sequential extraction data are presented as measured by ICP-AES

Depth (cm)	Age (ka)	Concentration in reducible oxides (extraction c)									Concentration in non reducible phase (bulk - (ferrihydrite + goethite))								
		Al (%)	P (%)	Fe (%)	Mn (%)	Ca (%)	V (ppm)	Cu (ppm)	Zn (ppm)	As (ppm)	Al (%)	P (%)	Fe (%)	Mn (%)	Ca (%)	V (ppm)	Cu (ppm)	Zn (ppm)	As (ppm)
9.8	8.6	0.006	0.09	0.5	0.001	0.16	0.54	7.8	0.9	15.3	0.027	0.070	1.27	0.37	6.0	141	36	27	10
15.5	13.3	0.007	0.13	0.6	0.001	0.17	0.85	8.9	2.1	19.7	0.019	0.054	1.03	0.26	5.3	129	28	25	16
25.5	22.8	0.007	0.11	0.7	0.002	0.14	0.98	6.6	2.7	22.0	0.029	0.063	1.26	0.40	6.7	137	41	29	26
35.5	31.8	0.009	0.22	1.1	0.003	0.21	1.81	3.7	4.9	17.1	0.029	0.086	1.41	0.44	5.3	184	63	31	68
55.5	49.8	0.007	0.12	0.8	0.001	0.18	0.94	8.9	2.8	15.8	0.025	0.064	1.22	0.36	5.6	150	41	26	33
75.5	67.9	0.009	0.15	1.1	0.002	0.18	1.65	4.1	6.2	21.4	0.027	0.084	1.63	0.53	6.6	174	76	33	27
90.5	81.4	0.010	0.10	1.3	0.003	0.14	1.91	4.7	8.8	14.2	0.030	0.056	1.50	0.49	6.7	183	85	31	49
153	133.1	0.012	0.10	1.6	0.004	0.15	1.98	6.3	11.3	26.9	0.037	0.067	1.65	0.46	6.1	196	95	31	47
203	176.8	0.007	0.03	0.8	0.003	0.14	0.94	9.8	4.8	11.0	0.033	0.050	1.33	0.45	6.2	150	56	31	25
253	209.4	0.014	0.11	1.5	0.008	0.12	1.98	3.8	10.6	22.8	0.051	0.060	1.39	0.48	6.0	174	99	32	44
303	239.9	0.009	0.08	1.7	0.011	0.16	2.12	11.8	12.9	11.9	0.019	0.097	2.01	0.66	5.2	248	128	39	73
403	300.9	0.008	0.03	0.8	0.004	0.20	0.84	12.6	4.2	16.2	0.026	0.071	1.45	0.53	7.0	177	68	31	31
453	331.4	0.010	0.25	2.5	0.030	0.22	3.49	6.2	17.1	55.6	0.017	0.113	1.87	0.56	6.1	245	142	37	55
503	362.0	0.010	0.12	1.2	0.015	0.18	1.24	4.9	7.7	17.0	0.032	0.102	1.46	0.43	6.9	172	67	57	54
573	404.9	0.010	0.08	1.4	0.021	0.13	1.72	5.1	11.4	25.0	0.023	0.062	1.73	0.71	8.8	184	107	39	37
608	427.0	0.007	0.11	1.0	0.016	0.17	1.07	4.4	7.7	40.2	0.030	0.113	1.39	0.45	7.2	152	62	27	11
623	436.5	0.007	0.01	0.5	0.006	0.21	0.40	19.6	0.9	16.1	0.021	0.106	1.52	0.49	6.2	169	41	30	9
648	452.3	0.007	0.03	0.7	0.013	0.17	0.63	15.9	4.1	24.6	0.022	0.095	1.47	0.48	6.5	173	52	28	13
663	461.7	0.007	0.03	0.5	0.003	0.23	0.32	15.9	0.1	7.4	0.024	0.103	1.63	0.55	5.1	176	53	32	32
673	468.1	0.016	0.24	2.2	0.047	0.19	3.12	3.2	15.3	50.5	0.036	0.106	1.96	0.83	5.3	263	133	41	57
708	498.3	0.011	0.14	1.9	0.030	0.15	2.48	7.0	13.0	42.9	0.022	0.079	1.88	0.66	5.4	281	124	34	61
753	545.8	0.009	0.17	1.6	0.025	0.20	2.06	4.6	8.8	57.2	0.029	0.112	1.60	0.57	5.4	237	95	30	38
803	591.1	0.014	0.25	2.1	0.052	0.23	3.14	3.0	14.0	46.4	0.031	0.127	2.00	0.75	6.2	239	129	37	68
853	630.0	0.008	0.09	1.3	0.038	0.17	1.25	7.4	6.3	17.6	0.028	0.106	1.60	0.52	5.8	213	67	33	60

Appendix 3: Detrital correction to data

Previously sediments from 14°S in the SEPR have considered to be best represented by a 3 component compositional model of carbonate material, hydrothermal material, and detrital material. If the detrital input to the core is significant, then the geochemical data requires detrital correction. It is usual for Ti or Al concentrations to calculate the detrital contribution to the sediment, making the assumption that all the Al and Ti are of lithogenic origin. The Ti and Al concentrations in core GS 7202-35 are extremely low and are shown in Table A3.1

Table A3.1 Ti and Al concentrations in core GS 7202-35

Sample ID	Depth Cm	Ti mg/g	Al mg/g
SLTTC2	9.75	0.059	0.717
SLTTC3	15.5	0.050	0.609
SLTTC5	25.5	0.062	0.701
SLTTC7	35.5	0.065	0.707
SLTTC11	55.5	0.062	0.694
SLTTC15	75.5	0.070	0.686
SLTTC18	90.5	0.072	0.760
SLTPC4	153	0.077	0.889
SLTPC14	203	0.068	0.740
SLTPC24	253	0.093	1.116
SLTPC34	303	0.056	0.615
SLTPC54	403	0.061	0.731
SLTPC64	453	0.047	0.530
SLTPC74	503	0.065	0.806
SLTPC88	573	0.060	0.649
SLTPC95	608	0.058	0.650
SLTPC98	623	0.058	0.623
SLTPC103	648	0.060	0.635
SLTPC106	663	0.063	0.687
SLTPC108	673	0.090	0.928
SLTPC115	708	0.078	0.714
SLTPC124	753	0.077	0.747
SLTPC134	803	0.082	0.786
SLTPC144	853	0.07	0.701

These sediments are far removed from any terrigenous inputs, so it assumed that any detrital material is primarily sourced from basaltic debris. Table A3.2 shows the composition of the EXCO basalts (Dunk, 2004)

Table A3.2: Composition of the EXCO basalts (Dunk, 2004). Values are calculated means (n=9). Values in brackets are 1σ.

Ti (wt %)	Ca/Ti (wt/wt)	Fe/Ti (wt/wt)	Mn/Ti (wt/wt)
0.88 (0.30)	10.5 (4.7)	10.5 (3.4)	0.19 (0.08)

Using the basalt ratio, the detrital input for each element (X_{det}) can be calculated using equation A3.1

$$X_{det} = Ti_{bulk} \,.\, (X/Ti)_{basalt}$$

Where Ti_{bulk} is the bulk Ti concentration and $(X/Ti)_{basalt}$ is the basaltic ratio. Table A3.3 shows X_{det} for the tracer elements Fe, Mn and Ca in core GS 7202-35.

Table A3.3 Bulk and detrital concentrations of phase tracers in core GS 7202-35.

Depth	Ti_{bulk}	Fe_{bulk}	Fe_{det}	% Fe detrital	Mn_{bulk}	Mn_{det}	% Mn detrital	Ca	Ca(Det)	% Ca detrital
cm	mg/g	mg/g	mg/g		mg/g	mg/g		mg/g	mg/g	
9.75	0.06	54	0.62	1.2	17	0.01	0.07	299	0.6	0.2
15.5	0.05	50	0.52	1.0	14	0.01	0.01	295	0.5	0.5
25.5	0.06	50	0.65	1.3	17	0.01	0.01	302	0.6	0.6
35.5	0.06	64	0.68	1.1	22	0.01	0.01	275	0.7	0.7
55.5	0.06	54	0.65	1.2	18	0.01	0.01	303	0.7	0.7
75.5	0.07	61	0.73	1.2	21	0.01	0.01	293	0.7	0.7
90.5	0.07	62	0.76	1.2	21	0.01	0.01	294	0.8	0.8
153	0.08	70	0.80	1.2	21	0.01	0.01	277	0.8	0.8
203	0.07	51	0.71	1.4	20	0.01	0.01	301	0.7	0.7
253	0.09	57	0.97	1.7	23	0.02	0.02	285	1.0	1.0
303	0.06	79	0.59	0.7	27	0.01	0.01	259	0.6	0.6
403	0.06	59	0.64	1.1	23	0.01	0.01	291	0.6	0.6
453	0.05	82	0.49	0.6	24	0.01	0.01	264	0.5	0.5
503	0.06	61	0.68	1.1	21	0.01	0.01	289	0.7	0.7
573	0.06	59	0.63	1.1	23	0.01	0.01	293	0.6	0.6
608	0.06	53	0.60	1.1	19	0.01	0.01	305	0.6	0.6
623	0.06	58	0.61	1.1	22	0.01	0.01	291	0.6	0.6
648	0.06	59	0.63	1.1	22	0.01	0.01	297	0.6	0.6
663	0.06	60	0.66	1.1	23	0.01	0.01	285	0.7	0.7
673	0.09	82	0.94	1.1	38	0.02	0.02	251	0.9	0.9
708	0.08	83	0.82	1.0	33	0.01	0.01	263	0.8	0.8
753	0.08	73	0.81	1.1	29	0.01	0.01	268	0.8	0.8
803	0.08	74	0.86	1.2	31	0.02	0.02	281	0.9	0.9
853	0.07	69	0.77	1.1	25	0.01	0.01	280	0.8	0.8

The calculated % of each element attributable to detrital material is <2% in all cases. This is less than the precision and accuracy associated with the ICP-AES measurements. Any detrital correction would therefore be less than the error associated with the analytical measurements, so detrital corrections are not required to these data.

References

Aller R.C., Rude, P.D. (1988) Complete oxidation of solid phase sulfides by manganese and bacteria in anoxic marine sediments *Geochimica et Cosmochimica Acta* **52**, 751-765

Anderson R. F., Fleisher M. Q., and LeHuray A. P. (1989) Concentration, oxidation state, and particulate flux of uranium in the Black Sea *Geochimica et Cosmochimica Acta* **53**(9), 2215-2224.

Antoine, D., André, J.-M., and Morel, A. (1996) Oceanic primary production 2 Estimation at global scale (coastal zone color scanner) chlorophyll *Global Biogeochemical Cycles*, **10,** 57-69.

Archer D., Wingarth A., Lea D., Mahowald N. (2000) What caused the glacial/interglacial atmosphere pCO2 cycles? *Reviews of Geophysics* **38**, 159-189

Archer, D., Maier-Reimer E. (1994) Effect of deep-sea sedimentary calcite preservation on atmospheric CO2 concentration. *Nature* **367**, 260– 263

Baker E. T., German, C. R., Elderfield, H., (1995) Hydrothermal plumes over spreading-center axes: global distributions and geological inferences. In: Humphris, S. E., Zierenberg, A., Mullineaux, L. S., Thomson, R. E. (Eds.), Seafloor hydrothermal systems. *Geophys. Monogr. Am. Geophys. Union.*, **91**, 47-71.

Barnes C. E. and Cochran J. K. (1990) Uranium removal in oceanic sediments and the oceanic U balance. *Earth and Planetary Science Letters* **97**(1-2), 94-101.

Barnes C. and Cochran J. (1988) The geochemistry of uranium in marine sediments. In *Radionuclides: A Tool for Oceanography* (ed. J. Guary, P. Guegueniat, and R. Pentreath), pp. 162-170. Elsevier.

Behrenfeld, M., Falkowski, P., (1997) Photosynthetic rates derived from satellite based chlorophyll concentration. *Limnol. Oceanogr.* **42**, 1 –20

Bender M. L. (1973) Helium-uranium dating of corals. *Geochimica et Cosmochimica Acta* **37**(5), 1229-1247.

Bender M., Broecker W., Gornitz V., Middel U., Kay R., Sun S.-S., and Biscaye P. (1971) Geochemistry of three cores from the East Pacific Rise. *Earth and Planetary Science Letters* **12**(4), 425-433.

Berger, W. H., Adelseck, C. G., Mayer, L. A., (1976) Distribution of carbonate in surface sediments of the Pacific Ocean. *J. Geophys. Res.*, **81**(15), 2617-2627.

Berner R A., Rao J., (1994) Phosphorus in sediments of the Amazon River and estuary: Implications for the global flux of phosphorus to the sea *Geochimica et Cosmochimica Acta,* **58**(10), 2333-2339.

Berner R. A. (1981) A New Geochemical Classification of Sedimentary Environments. *Journal of Sedimentary Petrology* **51**(2), 359-365.

Berner, R.A., (1973). Phosphate removal from sea water by adsorption on volcanogenic ferric oxides. *Earth Planet. Sci. Lett.* **18**, 77–86.

Bertine K.K., (1972) The deposition of Molybdenum in anoxic waters. *Marine Chemistry* **1**, 43-53

Bostrom K., Joensuu O., Kraemer T., Rydell H., Valdes S., Gartner S., and Taylor G. (1974) New finds of exhalative deposits on the East Pacific Rise. *Geologiska Foreningens i Stockholm Forhandlingar* **96**, 53-60.

Bostrum, K., Peterson, M. N. A., Joensuu, O., Fisher, D.E. (1969). Aluminium poor ferromanganoan sediments on active oceanic ridges. *J. Geophys. Res*. **74,** 3262.

Bostrom, K., Peterson, M.N.A., (1966). Precipitates from hydrothermal exhalations of the East Pacific Rise. *Economic Geology* **61**, 1258–1265.

Bourdon B., Turner S., Henderson G., and Lundstrom C. (2003) Uranium-series geochemistry. *Reviews in mineralogy and geochemistry* **52**, 1-656.

Bradtmiller, L. I., Anderson R. F., Fleischer M. Q., and Burkle L. H. (2006), Diatom productivity in the equatorial Pacific Ocean from the last glacial period to the present: A test of the silicic acid leakage hypothesis, *Paleoceanography*, **21**, PA4201, doi:10.1029/2006PA001282.

Calvert S.E., Pedersen T.F. (1993) Geochemistry of recent and anoxic marine sediments: implications for geological records *Marine Geology* **113**, 67-88

Campbell, A. C., (1991). Mineralogy and chemistry of marine particles by synchrotron X-ray spectrometry, Mossbauer spectrometry, and plasma-mass spectrometry. In: Hurd, D.C., Spencer, D.W., (Eds), *Geophys. Monogr., Am. Geophys. Union*., **63**: 375-390.

Canfield, D.E., (1998). A new model for Proterozoic ocean chemistry.*Nature* **396**, 450–453.

Cave, R.R., German, C.R., Thomson, J., Nesbitt, R.W., (2002). Fluxes to sediments underlying the Rainbow hydrothermal plume at 36_140N on the Mid-Atlantic Ridge. *Geochim. Cosmochim. Acta* **66**, 1905–1923.

Chavez, R., Barber, R., (1987) An estimate of new production in the equatorial Pacific. *Deep-Sea Res*. **34**, 1229– 1243.

Chen J. H., Lawrence Edwards R., and Wasserburg G. J. (1986) 238U, 234U and 232Th in seawater. *Earth and Planetary Science Letters* **80**(3-4), 241-251.

Cochran J. K. (1992) The oceanic chemistry of the uranium- and thorium-series nuclides. In *Uranium-Series Disequilibrium: Applications in Earth, Marine,*

and Environmental Sciences, Vol. 1 (ed. M. Ivanovich and R. S. Harmon), pp. 334-391. Oxford University Press.

Cochran J. K., Carey A. E., Sholkovitz E. R., and Surprenant L. D. (1986) The geochemistry of uranium and thorium in coastal marine sediments and sediment pore waters. *Geochimica et Cosmochimica Acta* **50**(5), 663-680.

Colley S., Thomson J., and Toole J. (1989) Uranium relocations and derivation of quasi-isochrons for a turbidite/pelagic sequence in the Northeast Atlantic. *Geochimica et Cosmochimica Acta* **53**, 1223-1234.

Colley S. and Thomson J. (1985) Recurrent uranium relocations in distal turbidites emplaced in pelagic conditions. *Geochimica et Cosmochimica Acta* **49**, 2339-2348.

Colley S., Thomson J., Wilson T., and Higgs N. (1984) Post-depositional migration of elements during diagenesis in brown clay turbidite sequences in North East Atlantic. *Geochimica et Cosmochimica Acta* **48**, 1223-1235.

Cormier, M-H., Scheirer, D. S., MacDonald, K. C., (1996). Evolution of the East Pacific Rise at 16-19S since 5Ma: bisection of overlapping spreading centres by new, rapidly propagating segments. *Mar. Geophys. Res.*, **18,** 53-84.

Cornell, R.M., Schwertmann, U., (1996). The Iron Oxides: Structure, Properties, Reactions, Occurrence and Uses. VCH, Weinheim, Germany.

Cornell, R.M., Giovanoli R., Schneider, W., (1989). Review of the hydrolysis of iron (III) and the crystallisation of amorphous iron(III) hydroxide hydrate. *J. Chem. Tech. Biochtechnol.* **46**, 115-134.

Cronan D. S., Hodkinson, R. A., (1997). Geochemistry of hydrothermal sediments from ODP sites 834 and 835 in the Lau Basin, southwest Pacific. *Mar. Geol.* **141,** 237-268.

DeMets, C., Gordon, R. G., Argus, D. F., Stein, S., (1994). Effect of recent revisions to the Geomagnetic Reversal Time Scale on estimates of current plate motions. *Geophys. Res. Lett.,* **21**: 2191-2194.

Devey, C. W., Bond, Z., Dunk, R. M.,Gharrib, J., Junge, G., Lackschewitz, K., Lear, C., Mottl, M., Pracht, J., Rudnicki, M., Scholz, C., Schramm, B., Severmann, S., Wheat, G., (2000). Cruise report. SO-145/2, Jan-Feb 2000 Talcahuano - Arica, Chile, University of Bremen, Germany.

Duce R. A., Arimoto R., Ray B. J (1986) Atmospheric distribution and sources of trace metals over the Pacific Ocean *Atmospheric environment* **20**(10), 2073-2074

Dunk R.M., Mills R.A., (2006) The impact of oxic alteration on plume-derived transition metals in ridge flank sediments from the East Pacific Rise. Marine Geology 229 (3-4), 133-157Dunk R. M., Mills R. A., and Jenkins W. J. (2002) A reevaluation of the oceanic uranium budget for the Holocene. *Chemical Geology* **190**(1-4), 45-67.

Dunk R. (2004) A Geochemical Study of Ridge Flank Sediments on the East Pacific Rise & The Development of Uranium as a Tracer of Low Temperature Hydrothermal Circulation *PHD Thesis*, University of Southampton.

Dunk, R. M., R. A. Mills, and W. J. Jenkins (2002) A reevaluation of the oceanic uranium budget for the Holocene, *Chemical Geology* **190,** 45– 67.

Dymond, J. E., Collier, R., McManus, J., Honjo, S., Manganini, S. (1997) Can the aluminium and titanium contents of ocean sediments be used to determine the paleoproductivity of the oceans? *Paleoceanography*, **12,** 586-193.

Dymond, J., Roth, S., 1988. Plume dispersed hydrothermal particles: a time-series record of settling flux from the Endeavour Ridge using moored sensors. *Geochimica et Cosmochimica Acta* **52**, 2525–2536.

Dymond J. (1981) Geochemistry of Nazca plate surface sediments: and evaluation of hydrothermal, biogenic, detrital, and hydrogenous sources. *Geological Society of America Memoirs* **Memoir 154**, 133-173.

Edmonds, H.N., German, C.R., (2004). Particle geochemistry in the Rainbow hydrothermal plume, Mid-Atlantic Ridge. *Geochim. Cosmochim. Acta* **68**, 759–772.

Elderfield, H., Schultz, A., (1996). Mid-ocean ridge hydrothermal fluxes and the chemical composition of the ocean. *Annual Review of Earth and Planetary Sciences* **24**, 191–224.

Elderfield, H., Greaves, M. J., Rudnicki, M. D., Hydes, D. J., (1993). Aluminium reactivity in hydrothermal plumes at the Mid Atlantic Ridge. *J. Geophys. Res*., **98**, 9667-9670.

Emerson, S. R., Huested, S. S., (1991) Ocean anoxia and the concentrations of molybdenum and vanadium in seawater. *Mar. Chem*., **34,** 177-196.

Feely, R. A., Sabine, C. L., Lee, K., Millero, F. J., Lamb, M. F., Greeley, D., Bullister, J. L., Key, R. M., Peng, T-H., Kozyr, A., Ono, T., Wong, C. S., (2002). In situ calcium carbonate dissolution in the Pacific Ocean. *Global Biogeochem. Cycle*., **16**(4), 1144, doi:10.1029/2002GB001866.

Feely, R. A., Trefry, J. H., Lebon, G. T., German, C. R., (1998). The relationship between P/Fe and V/Fe in hydrothermal precipitates and dissolved phosphates in seawater. *Geophys. Res. Lett.*, **25**, 2253-2256.

Feely, R. A., Baker, E. T., Marumo, K., Urabe, T., Ihibashi, J., Gendron, J., Lebon, G. T., Okamura, K., (1996). Hydrothermal plume particles and the dissolved phosphate over the superfast-spreading southern East Pacific Rise. *Geochim, Cosomochim. Acta*, **60,** 2297-2323.

Feely, R. A., Massoth, G. J., Trefry, J. H., Baker, E. T., Paulson, A. J., Lebon, G. T., (1994a). Composition and sedimentation of hydrothermal plume particles from North Cleft sediment, Juan de Fuca Ridge. *J. Geophys. Res.*, **99,** 4985-5006.

Feely, R. A., Gendron, J. F., Baker, E. T., Lebon, G. T., (1994b). Hydrothermal plumes along the East Pacific Rise 8°40' to 11°50'N: 3. Particle distribution and composition. *Earth Planet. Sci. Lett.* **128,** 19-36.

Feely R. A., Massoth G.J., Baker E.T. et al. (1992) Tracking the dispersal of hydrothermal plumes from the Juan de Fuca ridge using suspended matter composition *J. Geophys. Res – Solid Earth* **97**, 3457-3468

Feely R. A., Trefry J. H., Massoth G. J., and Metz S. (1991) A comparison of the scavenging of phosphorus and arsenic from seawater by hydrothermal iron oxyhydroxides in the Atlantic and Pacific Oceans. *Deep Sea Research Part A. Oceanographic Research Papers* **38**(6), 617-623.

Feely, R. A., Massoth, G. J., Baker, E. T., Cowen, J. P., Lamb, M. F., Krogslund, K. A., (1990a). The Effect of hydrothermal processes on mid water phosphorous distributions in the North East Pacific. *Earth Planet. Sci. Lett*., **96,** 305-318.

Feely, R. A., Geiselman, T. L., Baker, E. T., Massoth, G. J., Hammond, S. R., (1990b) Distribution and composition of buoyant and non buoyant hydrothemal plume particles from ASHES vent at Axial Volcano, Juan de Fuca Ridge. *J. Geophys. Res.*, **95,** 12855-12874.

Feely, R.A., Lewison, M., Massoth, G.J., Robert-Baldo, G., Lavelle, J.W., Byrne, R.H., Von Damm, K.L., Curl Jr. H.C., (1987). Composition and dissolution of black smoker particulates from active vents on the Juan de Fuca Ridge. *J. Geophys. Res.* **92**, 11347–11363.

Ford, R. G., Kemner, K. M., Bertsch, P. M., (1999). Influence of sorbate-sorbent interactions on the crystallization kinetics of nickel- and lead-ferrihydrite coprecipitates. *Geochim. Cosmochim. Acta,* **63,** 39-48.

Ford, R.G., Bertsch, P.M., Seaman, J.C., (1997). Changes in transition metal and heavy metal partitioning during hydrous iron oxide aging. *Env. Sci. Technol.*, **31**, 2028-2033.

Fouquet, Y., (1997). Where are the large hydrothemal sulphide deposits in the oceans? Trans. R. Soc. Lond., **355**: 427-441.

Francois, R., Frank M., Rutgers van der Loeff M. M., Bacon M. P. (2004), 230Th normalization: An essential tool for interpreting sedimentary fluxes during the late Quaternary *Paleoceanography* **19**, 1018, doi:10.1029/2003PA000939.

Francois R., Altabet M. A., Yu E. F., Sigman D. M., Bacon M. P., Frank M., Bohrmann G., Bareille G., and Labeyrie L. D. (1997) Contribution of Southern Ocean surface-water stratification to low atmospheric CO2 concentrations during the last glacial period. *Nature* **389**(6654), 929-935.

Francois R., Frank M., Rutgers van der Loeff M., Bacon M.P. (1994) 230Th normalization: An essential tool for interpreting sedimentary fluxes during the late Quaternary. *Paleoceanography* **19**, PA1018, doi:10.1029/2003PA000939

Francois R., (1988) A study on the regulation of the concentration of some trace metals (Rb, Sr, Pb, Cu, V, Cr, Ni, Mn, Mo) in Saanach Inlet sediments, British Columbia, Canada *Marine Geology,* **83**, 285-308

Froelich, P.N., Bender, M.L., Luedtke, N.A., Heath, G.R., DeVries, T., (1982). The marine phosphorus cycle. *Am. J. Sci.* **282**, 474–511.

German, CR; Von Damm, KL. (2004). Hydrothermal processes. In: *Treatise on geochemistry*. Ed. by KK Turekian; HD Holland. New York: Elsevier. Pages 181-222.

German C. R., Colley S., Palmer M. R., Khriponoff A., and Klinkhammer G. P. (2002) Hydrothermal plume-particle fluxes 13oN on the East Pacific Rise. *Deep Sea Research Part I: Oceanographic Research Papers* **49**(11), 1921-1940.

German, C. R., Bourles, D. L., Brown, E. T., Hergt, J., Colley, S., Higgs, N. C., Ludford, E. M., Nelson, T. A., Feely, R. A. Raisbeck, G., Yiou, F., (1997). Hydrothermal scavenging on the Juan de Fuca Ridge: $^{230}Th_{xs}$, ^{10}Be and REEs in ridge flank sediments. *Geochim. Cosmochim. Acta*., **61,** 4067-4078.

German C. R., Fleer A. P., Bacon M. P., and Edmond J. M. (1991) Hydrothermal scavenging at the Mid-Atlantic Ridge: radionuclide distributions. *Earth and Planetary Science Letters* **105**(1-3), 170-181.

German C. R., Klinkhammer G. P., Edmond J. M., Mitra A., and Elderfield H. (1990) Hydrothermal Scavenging of Rare-Earth Elements in the Ocean. *Nature* **345**(6275), 516-518.

Gieskes J.M., Sirocky F.X., Lakind, J. (1983) Interstitial water studies, Leg-72. *Initial reports of the Deep Sea Drilling Project* **72**, 391-394

Gieskes J.M., Elderfield H., Nevsky B. (1983) Interstitial water studies, Leg-65. *Initial reports of the Deep Sea Drilling Project* **65**, 441-449

Goldberg E. D., Somayajulu B. L. K., Galloway J., Kaplan I. R., and Faure G. (1969) Differences between barites of marine and continental origins. *Geochimica et Cosmochimica Acta* **33**, 287-289.

Grevemeyer I., Schramm B., Devey C. W., Wilson D. S., Jochum B., Hauschild J., Aric K., Villinger H. W., and Weigel W. (2002) A multibeam-sonar, magnetic and geochemical flowline survey at 14[deg]14'S on the southern East Pacific Rise: insights into the fourth dimension of ridge crest segmentation. *Earth and Planetary Science Letters* **199**(3-4), 359-372.

Gurvich E. G., (2006) *Metalliferous Sediments of the World Ocean. Fundamental Theory of Deep-Sea Hydrothermal Sedimentation*, Springer, Berlin 416 pp..

Halbach, P., Scherhag, C., Hebisch, U., Marchig, V., (1981). Geochemical and mineralogical control of different genetic types of deep-sea nodules from the Pacific Ocean. *Mineral Deposita*, **16,** 59-84.

Hansell D.A., Carlson C.A., Bates N.R., Poisson A., (1997) Horizontal and vertical removal of organic carbon in the equatorial Pacific Ocean: A mass balance assessment *Deep Sea Res. Part II* **44** (9-10), 2115-2130

Hauschild, J., Grevemeyer, I., Kaul, N., Villinger, H., (2003) Asymmetric sedimentation on young ocean floor at the East Pacific Rise, 15°S. *Mar. Geol.*, 193, 49-59.

Hegner E., Kroner A., and Hofmann A. W. (1984) Age and isotope geochemistry of the Archaean Pongola and Usushwana suites in Swaziland, southern Africa: a case for crustal contamination of mantle-derived magma. *Earth and Planetary Science Letters* **70**(2), 267-279.

Henderson G. and Anderson R. (2003) The U-series toolbox for paleoceanography. In *Reviews in Mineralogy and Geochemistry*, Vol. 52 (ed. B. Bourdon, S. Turner, G. Henderson, and C. Lundstrom), pp. 1-656.

Huang, B., and Z. Liu., (1999) Pacific subtropical-tropical thermocline water exchange in the National Centers for Environmental Prediction ocean model, *J. Geophys. Res.*, 104(C5), 11,065 – 11,076

Imbrie J., Hays J.D, Martinson D.G., McIntyre A., Mix A.C., Morley J.J., Pisias N.G. Prell., W.L., Shackleton N.J., (1984) The Orbital Forcing Theory of Pleistocene Clmate: Support for a revised chronolgy of the marine d^{18}O isotope record In *Milankovitch and Climate Part 1* (ed. A. Berger, J. Imbrie, J. Hays, G Kukla, B., Saltzman) pp. 269-305.D Reidel Publishing Company

Kadko, D., Feely, R., Massoth, G., (1994) Scavenging of ^{234}Th and phosphorous removal from the hydrothermal effluent plume over the North Cleft segment of the Juan de Fuca Ridge. *J. Geophys. Res.,* **99,** 5017-5024

Karl D M., Tien G. Dore +J., Winn C D., (1993) Total dissolved nitrogen and phosphorus concentrations at US-JGOFS Station ALOHA : Redfield reconciliation, *Marine Chemistry* **41,** 203-208

Kennedy, C.B., Scott, S.D., Ferris, F.G., (2004) Hydrothermal phase stabilization of 2-line ferrihydrite by bacteria. *Chem. Geol.* **212**, 269–277.

Kienast S. S., Kienast M., Mix, A. C., et al. (2007) Thorium-230 normalized particle flux and sediment focusing in the Panama Basin region during the last 30,000 years *Paleoceanography* **22**(2), 2213

Klinkhammer P. and Palmer M. R. (1991) Uranium in the oceans: Where it goes and why. *Geochimica et Cosmochimica Acta* **55**(7), 1799-1806.

Klinkhammer, G., Hudson, A., (1986). Dispersal patterns for hydrothermal plumes in the South-Pacific using manganese as a tracer. *Earth Planet. Sci. Lett*. **79**, 241–249.

Kniewald G. and Branica M. (1988) Role of uranium(V) in marine sedimentary environments: A geochemical possibility. *Marine Chemistry* **24**, 1-12.

Kolodny Y. and Kaplan I. (1973) Deposition of uranium in the sediment and interstitial water of an anoxic fjord. *Proceedings of Symposium on Hydrogeochemistry and Biogeochemistry*.

Ku T.-L., Ivanovich M., and Luo S. (1990) U-series dating of last interglacial high sea stands: Barbados revisited. *Quaternary Research* **33**, 129-147.

Ku T. L. (1966) Uranium series disequilibrium in deep sea sediments, Columbia University.

Kumar N., Anderson R. F., Mortlock R. A., Froelich P. N., Kubik P., Dittrichhannen B., and Suter M. (1995) Increased Biological Productivity and Export Production in the Glacial Southern-Ocean. *Nature,* **378**(6558), 675-680.

Lewis, E., Wallace D. W. R. (1998) Program Developed for CO2 System Calculations. ORNL/CDIAC-105.Carbon Dioxide Information Analysis Center, Oak Ridge National Laboratory, U.S. Department of Energy, Oak Ridge, Tennessee

Loubere, P., and M. Richaud (2007), Some reconciliation of glacial-interglacial calcite flux reconstructions for the eastern equatorial Pacific, *Geochem. Geophys. Geosyst.*, 8, Q03008, doi:10.1029/2006GC001367.

Loubere P. (2003) Remote vs. local control of changes in eastern equatorial Pacific bioproductivity from the Last Glacial Maximum to the Present. *Global and Planetary Change* **35**(1-2), 113-126.

Loubere, P., Fariduddin M., Murray R.W. (2003) Patterns of export production in the eastern equatorial Pacific over the past 130,000 years *Paleoceanography* **18**(2), 1028, doi:10.1029/2001PA000658

Loubere, P. (2000), Marine control of biological production in the eastern equatorial Pacific, *Nature,* **406**, 497–500.

Loubere, P. (1999), A multiproxy reconstruction of biological productivity and oceanography in the eastern equatorial Pacific for the past 30,000 years, *Mar. Micropaleontol*., **37**, 173– 198.

Lupton J.E., Pyle D.G., Jenkins W.J., Green R., Evans L. (2004) Evidence for an extensive hydrothermal plume in the Tonga-Fiji region of the South Pacific, *Geochem Geophys Geosyst* **5**(1), 1-18Lyle, M., D. Murray, B. Finney, J. Dymond,

Lupton, J. E., (1995). Hydrothermal plumes: Near and far field. Special publication-seafloor hydrothermal systems: physical, chemical, biological and geological interactions. *Geophys. Monogr., Am. Geophys. Union.*, **91,** 317-343.

Lupton, J.E., Craig, H., (1981) A major helium-3 source at 15_S on the East Pacific Rise. *Science* **214**, 13–18.

Lyle, M., N. Mitchell, N. Pisias, A. Mix, J. I. Martinez, and A. Paytan (2005), Do geochemical estimates of sediment focusing pass the sediment test in the equatorial Pacific?, Paleoceanography, **20**, PA1005,

Lyle, M., Mix A., Pisias N. (2002) Patterns of CaCO3 deposition in the eastern tropical Pacific Ocean for the last 150 ka: Evidence for a southeast Pacific depositional spike during marine isotope stage (MIS) 2 *Paleoceanography* **17**(2), 1013,

Lyle, M. (1992), Composition maps of surface sediments of the eastern tropical Pacific ocean, *Proc. Ocean Drill. Program Initial Rep*. **138,** 101– 115.

Lyle, M., Murray D.W., Finney B.P., Dymond J., Robbins J.M., Brooksforce K. (1988) The record of late Pleistocene biogenic sedimentation in the eastern tropical Pacific Ocean. *Paleoceanography* **3**, 39–59

Marchig, V., Erzinger J., Heinze, P. M., (1986). Sediments in the black smoker area of the East Pacific Rise (18.5º S). *Earth Planet. Sci. Lett*., **79**, 93-106.

Marsh, R., Josey, S. A., Nurser, A. J. G., de Cuevas, B. A., and Coward, A. C., 2005, Water Mass Transformation in the North Atlantic over 1985-2002 simulated in an eddy permitting model. *Ocean Science*, **2**, 1-18.

Martinez, C. E., McBride, M. B., (1998) Coprecipitates of Cd, Cu, Pb and Zn in iron oxides: Solid phase transformation and metal solubility after aging and thermal treatment. *Clays Clay Miner*., **46**: 537-545.

Matsumoto K., Oba T., Lynch-Stielglitz J., Yamamoto H., (2002) Interior hydrography and circulation of the glacial Pacific Ocean. *Quaternary Science Reviews* **21**, 1693-1704

McManus J., Berelson W.M., Klinkhammer G. P., Hammond D. E., Holm C. (2005) Authigenic uranium: relationship to oxygen penetration depth and organic carbon rain rate *Geohimica et Cosmochimica Acta* **69**, 95-108

Metz, S., Trefry, J.H., (1993). Field and laboratory studies of metal uptake and release by hydrothermal precipitates. *J. Geophys. Res*. **98**, 9661–9666.

Metz S., Trefry H., Nelson T., (1988) History and geochemistry of metalliferous sediment core from the Mid Atlantic Ridge. *Geochim. Cosmochim. Acta* **52**(10), 2369-2378

Milliman, J. D., Triy, P. J., Balch, W. M., Adams, A. K., Li, Y-H., Mackenzie, F. T., (1999) Biologically mediated dissolution of calcium carbonate above the chemical lysocline. *Deep Sea Res*., **46**, 1653-1669.

Mills, R. A. and H. Elderfield (1995) Rare earth element geochemistry of hydrothermal deposits from the active TAG Mound, 26 degrees-N Mid-Atlantic Ridge. *Geochim. Cosmochim. Acta* **59**, 3511-3524..

Mills R. A., Thomson J., Elderfield H., Hinton R. W., and Hislop E. (1994) Uranium enrichment in metalliferous sediments from the Mid-Atlantic Ridge. *Earth and Planetary Science Letters* **124**, 35-47.

Mills R., Elderfield H., and Thomson J. (1993) A Dual Origin for the Hydrothermal Component in a Metalliferous Sediment Core from the Mid-Atlantic Ridge. *Journal of Geophysical Research* **98**(b6), 9671-9681.

Mix A.C., (1989) Influence of productivity variations on long-term atmospheric CO2 *Nature* 337, 541-544

Morford J. L. and Emerson S. (1999) The geochemistry of redox sensitive trace metals in sediments. *Geochimica et Cosmochimica Acta* **63**(11-12), 1735-1750.

Murray J.W., Leborgne R., Dandonneau Y., JGOFS studies in the equatorial Pacific (1997) *Deep Sea Research Part II – Topical Studies in Oceanography* **44**(9-10), 1759-1763

Murray, R. W., Leinen, M., (1996). Scavenged excess aluminium and its relationship to bulk titanium in biogenic sediment from the central equatorial Pacific Ocean. Geochim. Cosmochim. Acta 60: 3869-3878.

Murray R. W., Leinen M., and Isern A. (1993) Biogenic flux of Alto sediment in the central equatorial Pacific Ocean: Evidence for increased productivity during glacial periods. *Paleoceanography* **6**, 651-669.

Olivarez, A.M., Owen, R.M., 1989. REE/Fe variations in hydrothermal sediments: Implications for the REE content of seawater. *Geochim. Cosmochim. Acta* **53**, 757–762.

Oschlies A., Koeve W., Garçon V (2000) An eddy-permitting coupled physical-biological model of the North Atlantic: 2.Ecosystem dynamics and comparison with satellite and JGOFS local station data, *Global Biogeochem. Cycles,* **14**, 499-523

Oxburgh R., (1998) Variations in the osmium isotope composition of sea water over the past 200,000 years, *Earth and Planetary Science Letters* **159**, 183–191

Paillard D., Labeyrie L., and Yiou P. (1996) Macintosh Program Performs Time-Series Analysis . *Eos, Transactions, American Geophysical Union* **77**, 379Pierrot, D. E. Lewis,and D. W. R. Wallace. 2006. MS Excel Program Developed for CO2 System Calculations. ORNL/CDIAC-105.Carbon Dioxide Information Analysis Center, Oak Ridge National Laboratory, U.S. Department of Energy, Oak Ridge, Tennessee.

Pailler D., Bard E., Rostek., Zheng Y., Mortlock R., Van Geen A. (2002) Burial of redox-sensitive metals and organic matter in the equatorial Indian Ocean linked to precession. Geochim. Cosmochim Acta **66**(5), 849–865

Paytan, A., M. Kastner, and F. P. Chavez (1996), Glacial to interglacial fluctuations in productivity in the equatorial Pacific as indicated by marine barite *Science* **274**, 1355–1357

Pedersen, T., B. Nielsen, and M. Pickering (1991), Timing of Late Quaternary productivity pulses in the Panama Basin and implications for atmospheric CO2, *Paleoceanography* **6** 657–678

Pedersen, T. F., M. Pickering, J. S. Vogel, J. N., Southon, and D. E. Nelson (1988), The response of benthic foraminifera to productivity cycles in the eastern equatorial pacific: Faunaland geochemical constraints on glacial bottom water oxygen levels, *Paleoceanography* **3,** 157–168

Pedersen, T. (1983), Increased productivity in the eastern equatorial Pacific during the last glacial maximum (19000 to 14000 Y. B. P.), *Geology*, **11**, 16– 19.

Popova E.E., Coward A.C., Nurser G.A., de Cuevas, B., Fasham., Fasham M. J. R., Anderson T.R. (2006) Mechanisms controlling primary and new production in a global ecosystem model Part 1: Validation of the biological simulation *Ocean Science* **2**(2), 249-266

Poulton SW, Canfield DE (2006) Co-diagenesis of iron and phosphorus in hydrothermal sediments from the southern East Pacific Rise: Implications for the evaluation of paleoseawater phosphate concentrations. *Geochimica et Cosmochimica Acta* **70**: 5883-5898.

Poulton, S.W., Canfield, D.E., (2005). Development of a sequential extraction procedure for iron: implications for iron partitioning in continentally derived particulates. *Chem. Geol*. **214**, 209–221.

Poulton, S.W., Raiswell, R., (2002). The low-temperature geochemical cycle of iron: from continental fluxes to marine sediment deposition. *Am. J. Sci*. **302**, 774–805.

Ravizza G., McMurtry G.M., (1993) Osmium isotopic variations in metalliferous sediments from the East Pacific Rise and the Bauer Basin. *Geochim. Cosmochim. Acta* **57**, 4301-4310

Raymo, M.E., Oppo, D.W., Curry, W., 1997. The mid-Pleistocene climate transition: a deep sea carbon isotope perspective. *Paleoceanography* **12**, 546–559.

Reid J.L. (1982) Evidence of an effect of heat flux from the East Pacific Rise upon the characteristics of the mid depth waters. *Geophys. Res. Lett.* **9**, 381-384

Reid J. L. (1981) On the mid-depth circulation of the world ocean. In *Evolution of Physical Oceanography* (ed. B. A. Warren and C. Wunsch), pp. 70-111. MIT Press

Rudnicki, M.D., Elderfield, H., (1993) A chemical model of the buoyant and neutrally buoyant plume above the TAG vent field, 26 degrees N, Mid-Atlantic Ridge. *Geochim. Cosmochim. Acta* **57**, 2939–2957.

Ruhlin, D. E., Owen, R. M., (1986) The rare earth element geochemistry of hydrothermal sediments from the East Pacific Rise: Examination of a seawater scavenging mechanism. *Geochim. Cosmochim. Acta*, **50,** 393-400.

Ruttenberg K C., Berner, R A., (1993) Authigenic apatite formation and burial in sediments from non-upwelling, continental margin environments *Geochimica et Cosmochimica Acta* **57**(5), 991-1007

Rydell H., Kraemer T., Boström K., and Joensuu O. (1974) Postdepositional injections of uranium-rich solutions into East Pacific Rise sediments. *Marine Geology* **17**(3), 151-164.

Sanyal, A., N. G. Hemming, W. S. Broecker, and G. N. Hanson (1997), Changes in pH in the eastern equatorial Pacific across stage 5–6 boundary based on boron isotopes in foraminifera, *Global Biogeochem. Cycles*, **11**, 125–133

Sarnthein, M., K. Winn, J. C. Duplessy, and M. R. Fontugne (1988), Global variations of surface ocean productivity in low and mid latitudes: Influence on CO2 reservoirs of the deep ocean and atmosphere during the last 21,000 years, *Paleoceanography*, **3**, 361–399.

Savenko, A. V., (2001) Coprecipitation of manganese, copper, zinc, lead and cadmium with iron hydroxide in hydrothermal plumes (by the data of laboratory modeling). *Oceanology,* **41**, 502-507.

Schaller T., Morford J., Emerson S. R., and Feely R. A. (2000) Oxyanions in metalliferous sediments: tracers for paleoseawater metal concentrations? *Geochimica et Cosmochimica Acta* **64**(13), 2243-2254.

Schippers A., Jorgensen B. B. (2001) Oxidation of pyrite and iron sulfide by manganese dioxide in marine sediments. *Geochimica et Cosmochimica Acta* **65**, 915-922

Schrader, H., and R. Sorknes (1990), Spatial and temporal variation of Peruvian coastal upwelling during the latest Quaternary, *Proc. Ocean Drill. Program Sci. Results*, **112**, 391– 406.

Shackleton, N.J., Berger, A., Peltier W.R., 1990. An alternative astronomical calibration of the lower Pleistocene timescale based on ODP Site 677. *Trans. R. Soc. Edinburgh, Earth Sci.,* **81**: 251-261.

Shackleton, N.J., Pisias, N.G., (1985). Atmospheric carbon dioxide, orbital forcing, and climate. In: Sundquist, E.T., Broecker, W.S. (Eds.), The Carbon cycle and

atmospheric CO_2: natural variations Archean to present. Geophys. Monogr., *Am. Geophys. Union.*, **32,** 412-417

Shackleton, N.J., Opdyke, N.D., (1973). Oxygen isotope and palaeomagnetic stratigraphy of Equatorial Pacific core V29-238: Oxygen isotope temperatures and ice volumes on a 10^5 year and 10^6 year scale. *Quat. Res*., **3,** 39-55.

Shimmield G. B. and Price N. B. (1988) The scavenging of U,230Th and 231Pa during pulsed hydrothermal activity at 20°S, East Pacific Rise. *Geochimica et Cosmochimica Acta* **52**(3), 669-677.

Shimmield G. B. and Price N. B. (1986) The Behavior of Molybdenum and Manganese During Early Sediment Diagenesis - Offshore Baja-California, Mexico. *Marine Chemistry* **19**(3), 261-280.

Schwertmann U., Taylor, R.M., (1989) Iron Oxides. *In: Minerals in Soil Environments*. Weed, S.B., Dixon, J.B. (Eds), Chap 8, pp. 379-438. Soil Science Society of America.

Sinha, B., Yool, A., (2006), Extension of the OCCAM 1 ocean general circulation model to include the biogeochemical cycles of carbon and oxygen PART I: Technical Description, *National Oceanography Centre Southampton Research and Consultancy Report* No. 6, 81pp.

Talley, L.D., (2007). Hydrographic Atlas of the World Ocean Circulation Experiment (WOCE). Volume 2: Pacific Ocean (eds. M. Sparrow, P. Chapman and J. Gould), International WOCE Project Office, Southampton, U.K., ISBN 0-904175-54-5.

Tans, P., Fung, I., Takahashi, T., (1990) Observational constraints on the global atmospheric CO2 budget. *Science* **247**, 1431–1438.

Thomson J., Brown L., Nixon S., Cook G. T., and MacKenzie A. B. (2000) Bioturbation and Holocene sediment accumulation fluxes in the north-east Atlantic Ocean (Benthic Boundary Layer Experiment sites). *Marine Geology* **169**, 21-39.

Thomson J., Higgs N. C., and Colley S. (1996) Diagenetic redistributions of redox-sensitive elements in northeast Atlantic glacial/interglacial transition sediments. *Earth and Planetary Science Letters* **139**(3-4), 365-377.

Thomson J., Higgs N. C., Croudace I. W., Colley S., and Hydes D. J. (1993) Redox zonation of elements at an oxic/post-oxic boundary in deep-sea sediments (abstract). *Geochimica et Cosmochimica Acta* **57**(3), 579-595.

Thomson J., Wallace H. E., Colley S., and Toole J. (1990) Authigenic uranium in Atlamtic sediments of teh last glacial stage - a diagenetic phenomenon. *Earth and Planetary Science Letters* **98**, 222-232.

Thomson J., Higgs N.C., Jarvis I., Hydes D. J., Colley S., Wilson T. R. S., (1986) The behaviour of manganese in Atlantic carbonate sediments *Geochimica et Cosmochimica Acta* **50**, 1807-1818

Thierstein, H.R., Geitzenauer, K.R., Molfino, B., Shackleton, N.J., (1977) Global synchroneity of late Quaternary coccolith datum levels: Validation by oxygen isotopes. *Geology*, **5**: 400-404.

Toggweiler J. R., Dixon K., and Broecker W. S. (1991) The Peru upwelling and the ventilation of the South Pacific thermocline. *Journal of Geophysical Research* **96**(C11), 20467-20497.

Toole J., Baxter M. S., and Thomson J. (1988) Some aspects of the marine geochemistry of uranium. In *Radionuclides: a tool for oceanography* (ed. J. C. Guary, P. Guegneniat, and R. J. Pentreath), pp. 183-194. Elsevier Applied Science.

Trefry, J.H., Metz, S., 1989. Role of hydrothermal precipitates in the geochemical cycling of vanadium. *Nature* **342**, 531–533.

Trocine, R.P., Trefry, J.H., 1988. Distribution and chemistry of suspended particles from an active hydrothermal vent site on the Mid-Atlantic Ridge at 261N. *Earth and Planetary Science Letters* **88**, 1–15.

Tsuchiya M., Lukas R., Fine R.A., Firing E., Lindstrom E., (1989) Source waters of the Pacific Equatorial Undercurrent *Progress in Oceanography* **23** (2), 101-147

Venuti A., Florindo F., Michel E., Hall I. R. (2007) Magnetic proxy for the deep (Pacific) western boundary current variability across the mid-Pleistocene climate transition, *Earth and Planetary Science Letters* **259**, 107-118

Wheat, C.G., Feely, R.A., Mottl, M.J., 1996. Phosphate removal by oceanic hydrothermal processes: an update of the phosphorus budget in the oceans. *Geochim. Cosmochim. Acta* **60**, 3593–3608.

Yang Y. L., Elderfield H., Pedersen T. F., Ivanovich M. (1995) Geochemical record of the Panama Basin during the Last Glacial Maximum carbon event shows that the glacial ocean was not suboxic *Geology* **23**, 1115-1118

Zhao, J., Huggins, F.E., Feng, Z., Huffman, G.P., (1994). Ferrihydrite: surface structure and its effects on phase transformation. *Clays Clay Miner*. **42**, 737–746.